

Temperature Decline Thermography for Flow and Heat Transfer Visualization in Aerodynamics

Stefan von Hößlin

Vollständiger Abdruck der von der Fakultät für Luft– und Raumfahrttechnik der Universität der Bundeswehr München zur Erlangung des akademischen Grades eines

Doctors rerum naturalium (Dr. rer. nat.)

genehmigten Dissertation.

Gutachter / Gutachterin:

1. Univ.-Prof. Dr. rer. nat. habil. Christian J. Kähler
2. Ao.Univ.-Prof. Dipl.-Ing. Dr.techn. Jakob Woisetschläger

Die Dissertation wurde am 04.11.2020 bei der Universität der Bundeswehr München eingereicht und durch die Fakultät für Luft– und Raumfahrttechnik am 11.11.2020 angenommen. Die mündliche Prüfung fand am 20.04.2021 statt.

Kurzfassung

Die Visualisierung von Strömungsphänomenen und Wärmeübergängen ist von zentraler Bedeutung für das physikalische Verständnis und die Weiterentwicklung aerodynamischer Systeme. Sie kann jedoch insbesondere bei bewegten Oberflächen und in instationären Strömungen eine große Herausforderung darstellen. Optische Methoden bieten einen vielversprechenden Ansatz, da sie eine hohe räumliche Auflösung mit schneller Datenerfassung kombinieren und die Grenzschichtströmung potenziell nicht stören.

In dieser Arbeit wird die Temperature Decline Thermography (TDT) genutzt, mit dem Ziel quantitative Wärmeübertragungsverteilungen an aerodynamischen Komponenten zu messen und Grenzschichtzustände in laminarer, turbulenter, transitioneller und abgelöster Strömung zu charakterisieren und zu visualisieren. Basierend auf einer Kurzzeitmessung von transienten Oberflächentemperaturen nach einem Wärmeimpuls, ermöglicht die Methode die berührungslose Analyse von kurzzeitigen Strömungseffekten und Grenzschichtzuständen in stationären sowie in schnell rotierenden Systemen. Diese Arbeit liefert eine detaillierte numerische und analytische Beschreibung des TDT-Messansatzes und eine umfassende Charakterisierung der Messkomponenten. Der Einsatz von TDT wird in verschiedenen Anwendungen demonstriert, die von einfachen ebenen Platten und Tragflügelprofilen bis hin zu experimentell anspruchsvollen Leit- und Laufschaufeln eines rotierenden Turbinenrigs reichen. Es wird gezeigt, dass neben qualitativen Strömungsvisualisierungen an stationären Komponenten auch quantitative Wärmeübergangsverteilungen nach einer Kalibrierung gemessen werden können. Die Detektion des laminar-turbulenten Übergangs mit TDT wird mit Oberflächen-Heißfilmen an einem NACA 0018 Profil mit verschiedenen Anstellwinkeln und bei Reynolds-Zahlen bis zu $Re = 2.3 \times 10^5$ validiert. Basierend auf der kurzen Dauer einer TDT-Messung wird abgeschätzt, ob und mit welcher Auflösung instationäre Übergänge gemessen werden können. Zusätzlich zu statischen Systemen wird die Anwendung von TDT in schnell rotierenden Systemen an einer rotierenden Turbinenschaufel bei $Re = 7.6 \times 10^5$ demonstriert. Trotz des eingeschränkten optischen Zugangs und geringer Lichtverhältnisse werden die wandnahen Spuren eines laminar-turbulenten Übergangs und Wirbelsysteme erstmals unter realistischen Rig-Bedingungen visualisiert.

Die Anwendung von TDT in komplexen Strömungssituationen ermöglicht ein umfassenderes Verständnis von Reibungsverlusten und Wärmeübertragungsverteilungen an aerodynamischen Komponenten. Sie ermöglicht die Unterstützung und Validierung von numerischen Modellen für die Weiterentwicklung hocheffizienter aerodynamischer Systeme.

Abstract

The visualization of boundary layer flow and heat transfer phenomena in aerodynamics is an essential approach for the physical understanding and further development of aerodynamic systems. However, it can be extremely challenging particularly for moving surfaces and in unsteady flows. Optical methods provide a promising approach as they combine a high spatial resolution with fast data acquisition and potentially do not disturb the boundary layer flow.

In this thesis, Temperature Decline Thermography (TDT) is applied to measure quantitative heat transfer distributions and visualize boundary layer states such as laminar, turbulent, transitional, and separated flow on aerodynamic components. Based on a short-time measurement of transient surface temperatures after an energy pulse, the method enables the contactless analysis of short-duration flow effects and boundary layer conditions in stationary, as well as fast-rotating systems. This work provides a detailed numerical and analytical description of the TDT measurement approach and a comprehensive characterization of the measurement components. The use of TDT is demonstrated in several applications ranging from simple flat-plates and airfoils, to experimentally challenging vanes and blades of a rotating turbine rig. It is shown that in addition to qualitative flow visualizations on stationary components, quantitative heat transfer distributions can be measured after a calibration. Laminar-turbulent transition detection with TDT is validated with surface hot films on a NACA 0018 airfoil with different angles of attack and at Reynolds numbers up to $Re = 2.3 \times 10^5$. Based on the short duration of a TDT measurement, an estimation for unsteady transition detection is given. In addition to stationary systems, the application of TDT in fast-rotating systems is demonstrated on a rotating turbine blade at $Re = 7.6 \times 10^5$. Despite the limited optical access and low light conditions, the near-wall traces of a laminar-turbulent transition and vortex systems are visualized under realistic rig conditions for the first time ever.

The application of TDT in complex flow situations provides deeper understanding of friction losses and heat transfer distributions on aerodynamic components. It enables the support and validation of numerical models for the further development of highly efficient aerodynamic systems.

Nomenclature

Symbol	Description	Dimension
α	heat transfer coefficient	$\text{Wm}^{-2}\text{K}^{-1}$
α_{lam}	heat transfer coefficient in laminar flow	$\text{Wm}^{-2}\text{K}^{-1}$
α_{tur}	heat transfer coefficient in turbulent flow	$\text{Wm}^{-2}\text{K}^{-1}$
α_{nat}	heat transfer coefficient of natural convection	$\text{Wm}^{-2}\text{K}^{-1}$
α'	heat transfer coefficient of natural convection containing material parameter	$\text{Wm}^{-2}\text{K}^{-1}$
β	angle of attack of a NACA-profile	$^{\circ}$
γ	attenuation coefficient	m^{-1}
Δx	difference of a quantity x_1 and x_2	dimension of x
δ	boundary layer thickness	m
ε	emissivity	—
Λ	temperature decline rate	s^{-1}
Λ_{ref}	temperature decline rate of a reference measurement without convective flow	s^{-1}
λ	wavelength of electromagnetic radiation	m
λ	thermal conductivity	$\text{Wm}^{-1}\text{K}^{-1}$
μ	dynamic viscosity	$\text{kgm}^{-1}\text{s}^{-1}$
ν	frequency of electromagnetic radiation	Hz
ν	kinematic viscosity	m^2s^{-1}
ξ	starting point of the heating area	m
ρ	density	kgm^{-3}
σ	Stefan–Boltzmann constant	$\text{Wm}^{-2}\text{K}^{-4}$
σ_{Λ}	standard deviation of the temporal Λ variations in a TDT measurement	s^{-1}
$\sigma_{\Lambda,\text{rel}}$	relative standard deviation of the temporal Λ variations in a TDT measurement	s^{-1}
σ_I	standard deviation of the temporal intensity variations	—
$\sigma_{I,\text{rel}}$	relative standard deviation of the temporal intensity variations	—
τ, τ_w	wall shear stress	$\text{kgm}^{-1}\text{s}^{-2}$

$\tau_{w,n}$	wall shear stress of a single measurement	$\text{kgm}^{-1}\text{s}^{-2}$
Φ	radiant flux	W
Φ_0	incident radiant flux	W
Φ_a	absorbed fraction of incident radiant flux	W
Φ_r	reflected fraction of incident radiant flux	W
Φ_t	transmitted fraction of incident radiant flux	W
A	area	m^2
A_D	detector area	m^2
Bi	Biot number	—
a	absorptance	—
c	speed of light	ms^{-1}
C	constant containing the volumetric heat capacity and the thickness of the coating	$\text{Jm}^{-2}\text{K}^{-1}$
C'	constant containing the volumetric heat capacity and the thickness of the coating and conduction coefficients	$\text{Jm}^{-2}\text{K}^{-1}$
c_1	constant containing the Planck constant, speed of light and the Boltzmann constant	J^2mK^{-1}
C_f	friction coefficient	—
c_p	specific heat capacity at constant pressure	$\text{JK}^{-1}\text{kg}^{-1}$
d	distance in a medium	m
d	thickness of a thermal slab	m
D_λ^*	specific spectral detectivity	$\text{Hz}^{-1/2}\text{W}^{-1}\text{m}$
E	energy	J
f	α dependent function	$\text{Wm}^{-2}\text{K}^{-1}$
f	image acquisition frequency of IR-camera	Hz
Fo	Fourier number	—
$f\#$	f-number of a camera lens	—
g	correction factor for an unheated starting length	—
h	Planck constant	Js
I	intensity values of a thermogram	—
I_0	intensity values of an offset thermogram	—
I_n	intensity values of the n^{th} thermogram	—
I_n^m	intensity values of the n^{th} thermogram and the m^{th} measurement	—

i	iterative index	—
K	length of the analysis interval on a temperature decline curve	—
k	Boltzmann constant	JK^{-1}
k	number of temperature step changes within heating area	—
k	iterative index	—
k_s	surface roughness coefficient	m
L_c	characteristic length of a geometry	m
M	excitance	Wm^{-2}
M	number of TDT-measurements	—
$M_{\lambda,BB}$	spectral excitance of a black body emitter	Wm^{-3}
M_{BB}	excitance of a black body emitter	Wm^{-2}
N	number of surface hot-film measurements / thermograms	—
N_0	number of offset thermograms	—
N_T	number of thermograms after the energy pulse	—
n	iterative index	—
NEP_λ	noise equivalent power	W
$NETD$	noise equivalent temperature difference	K
Nu	Nusselt number	—
Nu_x	local Nusselt number	—
$Nu_{x,\text{lam}}$	local Nusselt number of laminar flow	—
$Nu_{x,\text{tur}}$	local Nusselt number of turbulent flow	—
$Nu_{x,0}$	local Nusselt number with heating starting at $x = 0$	—
$Nu_{x,\xi}$	local Nusselt number with heating starting at $x = \xi$	—
p	pressure	$\text{kgm}^{-1}\text{s}^{-2}$
Pr	Prandtl number	—
Q	heat energy	J
Q_{conv}	convective heat energy	J
Q_{cond}	conductive heat energy	J
Q_{in}	heat energy entering a control volume	J
Q_{out}	heat energy leaving a control volume	J
Q_{rad}	radiative energy	J
Q_{st}	heat energy stored within a control volume	J
q	energy per unit area	Jm^{-2}

q_{pulse}	energy per unit area within an energy pulse	Jm^{-2}
r	reflectance	—
Re	Reynolds number	—
Re_{ks}	surface roughness Reynolds number	—
Re_x	local Reynolds number	—
$Re_{x,t}$	critical Reynolds number	—
RMS	root mean squared of a wall shear stress distribution in a surface hot film measurement	$\text{kgm}^{-1}\text{s}^{-2}$
s	volumetric heat capacity	$\text{Jm}^{-3}\text{K}^{-1}$
$SKEW$	skewness of a wall shear stress distribution in a surface hot film measurement	—
St	Stanton number	—
T	temperature	K
T_0	initial temperature	K
T_∞	free-stream temperature	K
T_{BB}	temperature of a black body emitter	K
T_{aw}	adiabatic wall temperature	K
T_{ref}	reference temperature	K
T_w	wall temperature	K
Tu	turbulence intensity	—
t	transmittance	—
t	time	s
t_{int}	integration time of a camera sensor	s
t_{lens}	transmittance of a camera lens	—
t_{opt}	optimal length of the analysis time interval on the temperature decline to reduce noise	s
u	streamwise velocity	ms^{-1}
u_∞	free-stream velocity	ms^{-1}
V	volume	m^3
V	voltage of a surface hot film	V
V_0	voltage of a surface hot film in a reference measurement	V
v	flow velocity in spanwise direction	ms^{-1}
x	spatial coordinate	m
y	spatial coordinate	m
z	spatial coordinate	m

z_γ	γ –quantile of the normal distribution	–
\dot{x}	time derivative with respect to a quantity x	dimension of $x \text{ s}^{-1}$
x^*	dimensionless form of a quantity x	–
\bar{x}	mean of a quantity x	dimension of x
$\partial/\partial x$	partial derivative with respect to a quantity x	dimension of x^{-1}
$\partial^2/\partial x^2$	second partial derivative with respect to a quantity x	dimension of x^{-2}

Content

1	Introduction.....	1
2	Theoretical Background.....	4
2.1	Heat transfer processes	4
2.1.1	Radiative heat transfer	4
2.1.2	Convective heat transfer.....	8
2.1.3	Conductive heat transfer	10
2.2	Boundary layer similarity	12
2.2.1	Boundary layer analogies.....	13
2.2.2	Nusselt correlations.....	14
2.2.3	Non-uniform heating correction.....	14
2.3	Heat transfer and aerodynamics in turbomachinery	16
2.3.1	Laminar-turbulent transition.....	17
2.3.2	Interaction of secondary vortex flow with the blade boundary layer.....	19
2.3.3	Validity of the Reynolds analogy on turbine blades	20
2.4	IR detectors and imaging systems.....	21
2.4.1	Absorption and detection of radiation in IR sensors	21
2.4.2	Properties of IR imaging systems	22
3	Temperature Decline Thermography	26
3.1	Methods for transition detection and flow visualization.....	26
3.1.1	Mechanical approaches	26
3.1.2	Electrical approaches	27
3.1.3	Optical approaches.....	28
3.2	Simulation of thermodynamic processes in TDT measurements.....	29
3.3	Theoretical derivation of the temperature decline rate	32
3.4	Experimental procedure and data analysis.....	34
3.4.1	Measurement setup	34
3.4.2	Temperature decline measurement with flow.....	35
3.4.3	Reference measurement without flow.....	36

3.4.4	Position reference acquisition	37
3.4.5	Image post-processing.....	38
3.4.6	Measurement error sources and data quality enhancement.....	42
3.5	Description and test of the measurement components.....	47
3.5.1	Radiative heating	47
3.5.2	Coating system.....	50
3.5.3	Infrared image acquisition	54
3.5.4	Trigger control	57
4	Quantitative heat transfer measurements	60
4.1	Aim of the measurement.....	60
4.2	Measurement setup	61
4.2.1	Setup for heat transfer calibration.....	61
4.2.2	Setup for non-uniform temperature correction.....	61
4.3	Heat transfer calibration.....	63
4.3.1	Calibration in a laminar flow	63
4.3.2	Application of the calibration relation on turbulent flow conditions	64
4.4	Uncertainty estimation.....	66
4.5	Non-uniform temperature correction.....	67
4.6	Conclusion on quantitative heat transfer measurements with TDT	71
5	Laminar-turbulent transition detection and validation.....	73
5.1	Aim of the measurement.....	73
5.2	Measurement setup	74
5.3	Transition detection on a NACA 0018 airfoil.....	75
5.4	Uncertainty estimation.....	79
5.5	Estimation for unsteady transition detection.....	79
5.6	Conclusion on transition detection with TDT.....	81
6	Flow visualization in a turbine rig.....	83
6.1	Aim of the measurement.....	83
6.2	Measurement setup	84
6.3	Flow visualization on stationary vanes	85

6.3.1	Vane measurement with a backward facing step	85
6.3.2	Influence of surface roughness on transition	87
6.4	Flow visualization on rotating blades	88
6.5	Uncertainty estimation.....	91
6.6	Conclusion on the application of TDT in turbine environments.....	92
7	Conclusion and outlook.....	93
	References.....	95
	List of publications by the author	105

Chapter 1

Introduction

The technological utilization of aerodynamics is one of the greatest engineering achievements of the last centuries. Understanding and mastering aerodynamic phenomena led to groundbreaking successes in aviation and spaceflight, enables global transportation and is fundamental for today's power generation. However, the enormous potential created by the understanding of aerodynamics requires a responsible approach. The rapidly growing global demand for transportation and electricity is leading to an extensive consumption of non-renewable resources and the emission of greenhouse gases. For example, the sector of global civil aviation caused 506 Mt of CO₂ in 2015 which constituted about 13 % of the total transportation-related and 2 % of the global CO₂ emissions [1]. If no significant reductions are achieved, emissions of the expanding aviation sector are expected to rise by more than a factor of 4 until 2050 [2], [A1]. Technological improvements play a major role in mitigating these scenarios for the transportation sector as well as for power generation [1].

Nowadays, numerical models are used to simulate flows around aerodynamic components to optimize their aerodynamic design and reduce friction losses. Particularly in industrial turbines and aircraft engines flow conditions are complex. Here, numerical models must still be supported and validated by experiments under realistic conditions. Moreover, used aerodynamic components like wind and gas turbine blades, or aircraft wings typically show impurities or surface damage at random positions, which impede a precise simulation of the flow conditions. Hence, experimental visualization of flow and heat transfer phenomena, and the detection of laminar-turbulent transition on rotating aerodynamic components are crucial.

Around the beginning of the last century, many experimenters like Osborne Reynolds, Ludwig Prandtl and Hugh L. Dryden created the experimental basis for today's boundary layer theory by visualizing boundary layer flows in tubes and around aerodynamic objects [3, 4, 5]. Nowadays, high-performance optical sensors and laser systems enable methods such as Particle Image Velocimetry (PIV), Laser-Doppler Anemometry (LDA) and Infrared Thermography (IT), which provide an accurate experimental foundation for model validation [6, 7]. However, for flow visualization in high-speed applications like in gas turbines, conventional measurement methods are limited by the heavy casings, limited space, and fast rotating parts. Furthermore, many methods are susceptible to interfering

reflections of surrounding components or give unreliable results as the boundary conditions are often not known with the required precision. Especially on moving turbine blades, this could cause erroneous transition detection and flow visualization [A1].

To overcome these challenges, a novel measurement approach was recently proposed in a patent document by Stadlbauer et al. [8]. They predicted a high potential of this approach to measure transition positions and wall shear stress distributions on stationary and fast-rotating parts, but never demonstrated its application. In this thesis the approach, referred from now on to as Temperature Decline Thermography (TDT), is further developed and its application is demonstrated on stationary as well as fast-rotating aerodynamic components.

As Fig. 1 illustrates, TDT requires only minimal instrumentation consisting of a radiative energy source, a high-speed infrared camera and a thermal coating system on the aerodynamic component. The coating system is illuminated by the radiative energy pulse and the subsequent temperature decline is recorded by the camera. By calculating the temperature decline rates for each pixel, heat transfer coefficients are visualized as a two-dimensional map. Since heat transfer coefficients differ strongly between laminar and turbulent flow states, boundary layer transition and other near-wall flow effects such as laminar separation bubbles and turbulent flow separations can be analyzed with high spatial resolution. The evaluation of relative temperature changes and the subtraction of a reference measurement without flow strongly reduce interfering effects such as inhomogeneous surface heating and reflections from surrounding components.

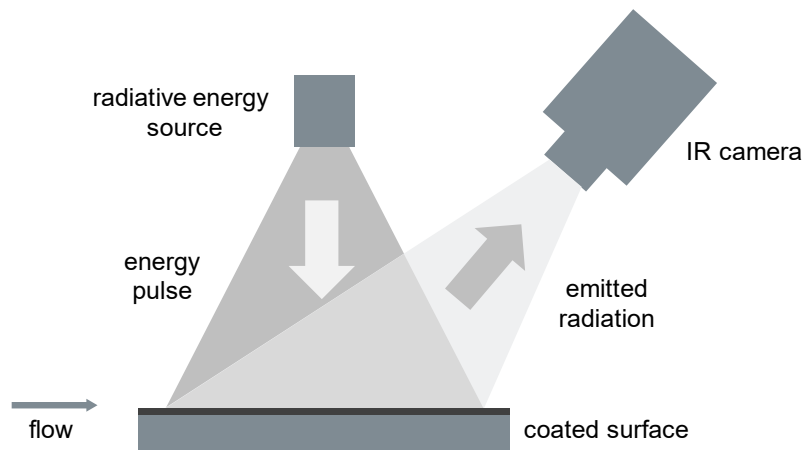


Figure 1 Schematic of the general measurement approach

The aim of this thesis is to demonstrate the use of the TDT method for boundary layer transition detection and heat transfer visualization on stationary and fast-rotating aerodynamic components. Therefore, the heat transfer processes during a TDT measurement are analyzed analytically and numerically in detail. At first, basic tests are conducted to characterize the measurement instruments and to validate the measurement principle and post-processing methods. Then, heat transfer visualizations are performed on different applications ranging from simple flat plates and airfoils to experimentally challenging turbine vanes and rotating blades. These experiments provide a demonstration for qualitative and quantitative determination of heat transfer distributions, a validation of the detection of boundary layer transition with TDT, and, for the first time ever, the visualization of a boundary layer transition on a rotating turbine blade under realistic conditions.

Chapter 2

Theoretical Background

2.1 Heat transfer processes

In this thesis, flow visualization and heat transfer measurements are conducted by infrared thermography. These measurements are based on three mechanisms of thermal heat transport: radiative, convective, and conductive heat transfer. Radiative heat transfer enables the contactless heating and temperature measurement of an aerodynamic component and strongly influences the quality of a TDT measurement. Convective heat transfer provides information about the flow conditions around the component and represents the relevant measurement quantity for TDT. Conductive heat transfer describes the propagation of thermal energy within the component and must be controlled to reduce heat loss during the measurement. In the following, the heat transfer mechanisms are described in the context of TDT.

2.1.1 Radiative heat transfer

Radiative heat transfer is based on the transport of thermal energy by electromagnetic (EM) radiation. EM waves or their quantized form, photons, carry an amount of energy that is characterized by their wavelength λ or frequency ν

$$(1) \quad E = h\nu = \frac{hc}{\lambda},$$

where h is the Planck constant and c the speed of light in vacuum. By the interaction with matter, this amount of energy can be absorbed and converted into heat which increases the temperature T of the matter. Since all bodies with $T > 0\text{ K}$ emit EM radiation, the stored heat is partially converted back into photons and radiated by the body. This process of heat transport is not only essential for life on earth but can be controlled and used for various technical tasks.

In TDT measurements, radiative heat transfer is used in several ways as shown in Fig. 2. In the heating step, electrical energy is converted into EM radiation by a radiative energy source. The radiation propagates through the atmosphere, is altered by optical elements, and partially absorbed by a solid body.

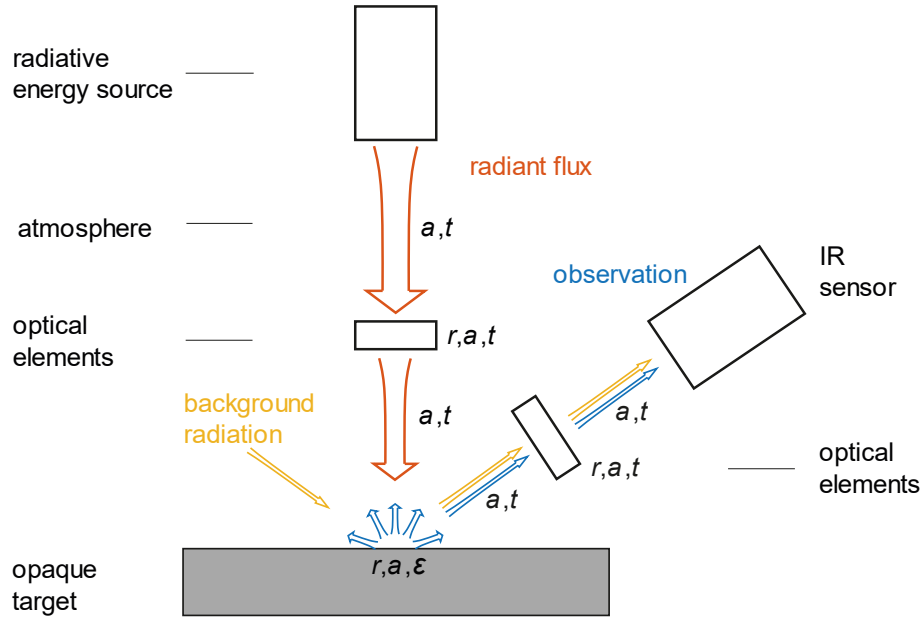


Figure 2 Principle of a TDT measurement. Arrows display the radiant flux. The letters r , a , t and ε stand for reflection, absorption, transmission, and emission processes which are present in the individual sections of the optical path, respectively.

The absorbed energy increases the body temperature T and is partially radiated into the hemisphere which defines the start of the observation step. Compared to the incident radiation, the emitted radiation contains a different spectrum of wavelengths: depending on the body temperature, wavelengths in the infrared (IR, $700\text{ nm} < \lambda < 100\text{ }\mu\text{m}$), visible (VIS, $400\text{ nm} < \lambda < 700\text{ nm}$) and, for high temperatures, ultraviolet range (UV, $10\text{ nm} < \lambda < 400\text{ nm}$) are observed [9].

For the temperature measurement with an IR sensor, only part of the wavelength spectrum and part of the hemispherical emitted radiation is collected and converted into a voltage signal for further analysis.

2.1.1.1 Absorption, reflection, and transmission of EM radiation in matter

The energy source emits a certain amount of energy per unit time which is called the radiant flux Φ . Since all EM waves are influenced by the interaction with matter, the radiation leaving the energy source is scattered, absorbed, and transmitted by the medium in which it propagates. This results in an attenuation of the radiant flux which correlates with the distance d traveled in the medium and is described by the Bouguer–Lambert–Beer law [10]

$$(2) \quad \Phi_t(\lambda, d) = \Phi(\lambda, 0)e^{-\gamma(\lambda)d}.$$

Here, γ is the attenuation coefficient which includes the sum of absorption and scattering processes. When passing through matter, the incident radiant flux is therefore divided into a transmitted and an absorbed/scattered part. At the interface of two media, reflection occurs. The transmittance t ,

absorptance a and reflectance r are defined as their fraction of radiant flux compared to the incident radiant flux $\Phi_0(\lambda)$

$$(3) \quad t(\lambda) = \frac{\Phi_t(\lambda)}{\Phi_0(\lambda)}, \quad a(\lambda) = \frac{\Phi_a(\lambda)}{\Phi_0(\lambda)}, \quad r(\lambda) = \frac{\Phi_r(\lambda)}{\Phi_0(\lambda)}.$$

According to the conservation of energy, $\Phi_0 = \Phi_t + \Phi_a + \Phi_r$. Therefore,

$$(4) \quad 1 = t + a + r.$$

On the radiative path to the target (see Fig. 2), a and r must be reduced to enhance the heating efficiency. For most transparent mediums like air and special glasses used for optical elements, a is negligible. To reduce r , the surface of the optics is often enhanced with anti-reflective coatings.

When the transmitted radiant flux hits the surface of the opaque target, t is zero and the whole incident flux is absorbed or reflected. The absorbed part is converted into heat energy. The reflected part can no longer be used for the measurement. Thus, to enhance heating efficiencies and reduce the effect of background reflections, r of the target must be reduced or, in other terms, a must be enhanced.

2.1.1.2 Emissivity

When an object absorbs a fraction of the incident radiation, its absorptance is $0 < a < 1$. If the object is further in a state of thermal equilibrium, the amount of radiation absorbed by the object equals the amount of radiation which is emitted by the object. According to Kirchhoff's law and Eq. (4), the emissivity ε is therefore [10]

$$(5) \quad \varepsilon = a = 1 - r.$$

A high emissivity therefore reduces the reflectance and enhances the absorptance of the target. For a definition of ε , the excittance M is used which relates the hemispherical emitted radiant flux and the emitting surface element dA

$$(6) \quad M = \frac{d\Phi}{dA}.$$

ε is then defined as the ratio of the excittance compared to the excittance of an ideal blackbody emitter $M_{BB}(T)$

$$(7) \quad \varepsilon = \frac{M(T)}{M_{BB}(T)}.$$

An ideal blackbody emitter is hereby an idealized object which absorbs all incident radiation and emits the maximum radiant flux for a given temperature and wavelength. The radiation is emitted uniformly in all directions into the hemisphere.

Realistic objects have emissivities lower than 1. Furthermore, the emissivity of a realistic object may depend on wavelength, angle of observation and temperature. For IR measurements in this work, high-emissivity coatings are used where ε can be assumed to be independent of wavelength and direction [11]. Furthermore, as will be seen in Sec. 3.4.5, the dependency on wavelength, direction and temperature are of minor importance for TDT measurements since only relative temperature differences are measured. For the sake of simplicity, the definition of a grey body with a hemispherical emissivity $\varepsilon < 1$ independent of wavelength, viewing angle and temperature, is used for further theoretical considerations as found in Eq. (7).

An additional factor that influences the emissivity is the roughness of the surface. Vollmer and Möllmann [10] showed that roughening flat metal surfaces increases ε . The same trend is also observed for irregularly distributed roughness elements [12]. This phenomenon is explained by a radiance enhancement by reflections of emitted radiation on neighboring roughness elements. Increasing the roughness of a surface therefore increases its emissivity. However, an increased surface roughness has further implications on a TDT measurement regarding boundary layer flows. This will be further discussed in Sec. 2.3.1 and 6.3.2.

2.1.1.3 Spectrum of blackbody emitters

IR thermography is based on the measurement of the temperature dependent spectrum emitted by an object with $T > 0\text{K}$. It is assumed that the spectral excittance of a blackbody emitter in a wavelength interval $[\lambda, \lambda + d\lambda]$ is only dependent on the temperature which is described by Planck's law

$$(8) \quad M_{\lambda, \text{BB}}(T) d\lambda = \frac{2\pi hc^2}{\lambda^5} \frac{1}{e^{\left(\frac{hc}{\lambda kT}\right)} - 1} d\lambda,$$

where k is the Boltzmann constant. By integrating over the whole spectral range, the Stefan–Boltzmann law is found which describes a T^4 dependence of the total excittance of a blackbody emitter

$$(9) \quad M_{\text{BB}}(T) = \int_0^\infty M_{\lambda, \text{BB}}(T) d\lambda = \sigma T^4,$$

where σ is the Stefan–Boltzmann constant. For infrared thermography, this observation is of great importance as the emitted radiation spectrum of an object is correlated to its absolute temperature. However, IR sensors can only detect radiation in a specific wavelength range which changes the described T^4 dependency for the measured sensor signal. Furthermore, radiation within a limited solid angle is collected by the sensor. From a blackbody emitter, only a fraction of $M_{\text{BB}}(T)$ is therefore detected which is further reduced for more realistic objects with $\varepsilon < 1$ (see Eq. (7)). In TDT measurements only small temperature changes are analyzed and absolute temperatures are not relevant. A linear relationship between the sensor signal and the object temperature can be assumed in good approximation.

2.1.2 Convective heat transfer

Convective heat transfer describes the transport of thermal energy in fluids by the motion of fluid elements. This can either be the random motion of individual elements (diffusion) or the bulk motion of macroscopic particle collectives (advection). For the application of TDT on aerodynamic components exposed to an air flow, the heat transfer at the surface of these components is considered. Based on the convection conditions at the surface, valuable information of the interaction between the flow and the surface geometry can be derived.

2.1.2.1 Velocity and thermal boundary layer

At the surface of the component exposed to flow, a boundary layer develops in which the flow velocity is reduced compared to its free-stream velocity u_∞ . The velocity takes values between zero at the surface and u_∞ in the undisturbed flow. The retardation of the fluid elements is caused by friction at the wall, which affects adjoining fluid layers with decreasing intensity until free-stream conditions are reached, and the retardation is negligible. The resulting thickness δ of the boundary layer is defined by the distance from the wall at which the fluid velocity is $u = 0.99u_\infty$. Figure 3 shows the typical boundary layer behavior for a stationary flow along a smooth flat plate. At the leading edge $x = 0$, the boundary layer thickness is zero. With increasing x , the retardation of the fluid elements propagates further into the free-stream and the thickness increases. The velocity profile $u(y)$ and the friction denoted as the wall shear stress τ at a certain position x are dependent on the dynamic viscosity μ of the fluid. The wall shear stress is determined by evaluating the gradient of the velocity profile at the wall

$$(10) \quad \tau = \mu \left. \frac{\partial u}{\partial y} \right|_{y=0}.$$

If a temperature difference is present between flow and surface, a thermal boundary layer develops in addition to the velocity boundary layer as illustrated in Fig. 3. Like the velocity, the temperature $T(y)$ varies between the wall temperature T_w and the outer flow T_∞ . At the wall, a heat flux occurs which is proportional to the temperature difference of the wall temperature and a reference temperature T_{aw} . The amount of heat energy Q that is transferred per unit time and area A is given by Newton's law of cooling

$$(11) \quad \dot{q} = \frac{\dot{Q}}{A} = \alpha(T_w - T_{aw}).$$

Here, α represents the heat transfer coefficient. It is mainly dependent on fluid properties and flow conditions within the boundary layer which alter the temperature profile of the thermal boundary layer. T_{aw} is the adiabatic wall temperature which is observed at thermal equilibrium without heat flux on the wall. For subsonic flows, it can be approximated by T_∞ [13, 14, 15].

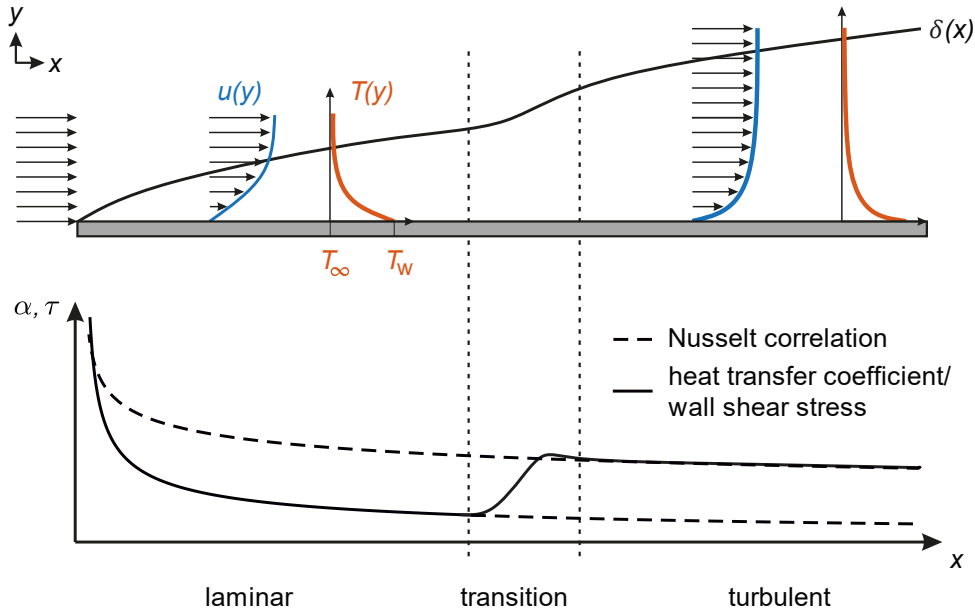


Figure 3 Top Development of velocity and thermal boundary layer on a flat plate exposed to convective flow with velocity u_∞ and temperature T_∞ . T_w is the surface temperature and δ denotes the boundary layer thickness. **Bottom** Heat transfer coefficient α and wall shear stress τ along the flat plate (solid line). The lower and upper dashed line represents the Nusselt correlation for fully laminar and fully turbulent flow, respectively. Regions of laminar, transitional, and turbulent flat plate boundary layer are labeled.

2.1.2.2 Laminar, transitional, and turbulent boundary layer

As illustrated in Fig. 3, the flow along a flat plate is characterized by laminar and turbulent flow. Immediately after the leading edge of the flat plate, a laminar boundary layer develops. Here, the flow follows ordered stream paths with a uniform velocity and there is only molecular mixing between the forming flow layers. However, small disturbances are already present in the laminar boundary layer which originate from surface roughnesses and non-uniformities in the outer flow for instance. The transition from the laminar to the turbulent flow state can be characterized by three stages. First, small disturbances are amplified with increasing distance from the leading edge forming two-dimensional Tollmien–Schlichting waves. In the second stage, these instabilities are further amplified resulting in three-dimensional hairpin-like vortices from which turbulent spots emerge. Finally, the turbulent spots grow and lead to a fully developed turbulent flow [16, 17]. The state of the boundary layer is usually quantified by the intermittency. It is defined as the fraction of time in which the flow is turbulent at a certain position in the boundary layer. The intermittency is 0 for the fully laminar, 1 for the fully turbulent boundary layer state and in between these values for the transitional state.

The onset of transition on a flat plate depends on the density ρ , the dynamic viscosity of the fluid, the free-stream velocity, and the distance from the leading edge. These parameters are summarized in the dimensionless Reynolds number which represents the ratio of inertia and viscous forces

$$(12) \quad Re_x = \frac{\rho u_\infty x}{\mu}.$$

There are additional parameters which influence the location of transition such as the free-stream turbulence intensity, the surface roughness, pressure gradients and acoustic disturbances. If these parameters have a negligible effect, the transition position can be estimated to a critical Reynolds number of about $Re_{x,t} = 3.5 \cdot 10^5$ to 10^6 [18].

Because of the resulting movement of larger fluid patches and the mixing of near-wall flow with layers of the outer flow during transition, the boundary layer thickness as well as wall shear stress and heat transfer coefficients strongly increase as illustrated in the bottom plot of Fig. 3. The development of heat transfer coefficient and wall shear stress along a component and therefore the detection of laminar-turbulent transition will be presented in this thesis for various geometries. The described transitional behavior is called natural transition. As will be described in the context of flows in turbomachinery, further modes of transition exist which depend on multiple parameters.

2.1.3 Conductive heat transfer

Conductive heat transfer is the third mechanism of heat transport relevant for TDT. Thermal conduction is the energy transport enabled by the diffusion of fluid elements in gases and liquids without any bulk motion. In solids, vibrations in the atomic lattice transport heat through the material and in conducting solids like metals, additionally free electrons transport heat energy via diffusion. This leads to a faster distribution of heat compared to non-conductive materials [19]. In a TDT measurement, conduction processes occur after the pulsed heating within the aerodynamic component and influence the transient temperature measurement at the surface.

2.1.3.1 Fourier's law and heat equation

For one-dimensional conduction processes in an isotropic medium, the heat flux is described by Fourier's law

$$(13) \quad \dot{q} = \frac{\dot{Q}}{A} = -\lambda \frac{\partial T}{\partial x},$$

where λ is the thermal conductivity and $\partial T / \partial x$ the spatial temperature gradient within the material. From Fourier's law, the heat equation is derived by considering the conservation of energy flux through a small volume $dV = A dx$ of the medium

$$(14) \quad \dot{Q}_{\text{in}} - \dot{Q}_{\text{out}} = \dot{Q}_{\text{st}}.$$

The change of stored energy within this volume is $\dot{Q}_{st} = s\dot{T}dV$ and $\dot{Q}_{in} - \dot{Q}_{out} = -\partial\dot{Q}/\partial x dx$. Hence, the one-dimensional heat equation is given as

$$(15) \quad \frac{\partial^2 T}{\partial x^2} = \frac{s}{\lambda} \frac{\partial T}{\partial t}.$$

Here, s is the volumetric heat capacity which is defined as the specific heat capacity at constant pressure multiplied by the density of the isotropic material $s = c_p \rho$ [13]. The heat equation gives the temporal and spatial distribution of the temperature in the medium and is used in Sec. 3.2 for simulations to better understand heat conduction processes and conduction losses during a TDT measurement.

2.1.3.2 Simplified model for transient conduction

The heat equation can only be solved analytically for a few specific problems of heat conduction. An estimation of the transient temperature decline after an energy pulse in a TDT measurement can be analytically described by a simple model. Here, a thermally thin slab on the component is exposed to a convective flow. Thermally thin means, that a spatially uniform temperature can be assumed within the slab during the transient process. At the back surface, the slab is ideally insulated against the component. As shown in Fig. 4, the slab is externally heated at $t = 0$ which increases the temperature compared to the flow temperature, $T_w > T_\infty$. Shortly after the heating, a convective heat flux occurs at the surface reducing the heat stored within the slab. When radiative heat transfer is neglected, the conservation of heat flux is given by

$$(16) \quad \dot{Q}_{conv} = -\dot{Q}_{st}.$$

Using Newton's law of cooling and the change of stored energy within the slab, the expression can be rewritten as

$$(17) \quad \alpha \Delta T = -sd \Delta \dot{T},$$

with the temperature difference $\Delta T = T_w - T_{aw}$ and the thickness of the slab $d = V/A$ in y direction. The analytical solution of this differential equation is found by integration

$$(18) \quad \Delta T(t) = \Delta T_0 e^{-\frac{\alpha}{sd}t},$$

where ΔT_0 is the temperature difference directly after the heating. In the TDT method, the exponent of this transient temperature behavior is analyzed. It is called the temperature decline rate $\Lambda = \alpha/(sd)$ and is proportional to the heat transfer coefficient.

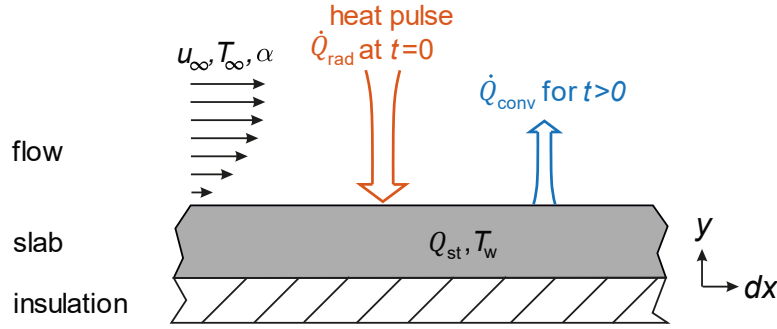


Figure 4 Radiative and convective heat fluxes \dot{Q}_{rad} and \dot{Q}_{conv} on a thermally thin slab which is externally heated at time $t = 0$ and exposed to a convective flow. Q_{st} is the stored energy within the slab which lower surface is ideally insulated.

This simple solution of the transient temperature is, however, limited by the assumption of isothermal conditions within the slab and the ideal insulation at its back surface. The validity of these assumptions is dependent on different material parameter, the convection condition at the surface and the elapsed time after the external heating. The parameters are summarized in the dimensionless Biot and Fourier number

$$(19) \quad Bi = \frac{\alpha L_c}{\lambda}, \quad Fo = \frac{\lambda t}{s L_c^2},$$

where L_c is a characteristic length of the geometry, in this case $L_c = d$. According to Astarita and Carlomagno [15], the isothermal model can be applied for $Bi < 0.05$ and $Fo > 0.5$, if external heating is considered. Incropera and DeWitt [13] follow a less conservative approach by stating the validity of the model for $Bi < 0.1$. This means that the thermal conductivity of the slab should be large, whereas a small thickness and low heat transfer coefficients are preferable. Moreover, to increase Fo , the measurement should be started after a certain amount of time after the energy pulse.

In a TDT measurement the assumption of an ideal insulation is not generally fulfilled. An extension of the simplified model will therefore be derived in Sec. 3.3.

2.2 Boundary layer similarity

For the comparison with numerical models and other measurement methods, the physical interpretation of TDT data is of central importance. As indicated in Fig. 3, the heat transfer coefficient, and therefore the measured temperature decline rate, is proportional to wall shear stress under certain conditions. This constitutes an important extension of the interpretability of TDT data. In this section, the governing differential equations for velocity and thermal boundary layers are used to describe the relation between the heat transfer and the wall shear stress. This is subject to certain assumptions which will be discussed in the following.

2.2.1 Boundary layer analogies

In boundary layer theory, several assumptions are made to simplify the governing differential equations of velocity and thermal boundary layers. Generally, the fluid is regarded as a continuum, where the mean free path of the molecules is small compared to a characteristic length of the flow field. Further, it is assumed that the fluid in the boundary layer is incompressible ($\rho = \text{const.}$), has a negligible free-stream turbulence and generates no additional energy. Body forces such as gravitational or centrifugal ones are negligible, and the boundary layer thickness is very small. For subsonic, forced convection flows over a smooth surface the velocity and thermal boundary layers are then described by three coupled, non-linear differential equations, the continuity, momentum, and energy equation. They take the dimensionless form in u -direction [13]

$$(20) \quad \frac{\partial u^*}{\partial x^*} + \frac{\partial v^*}{\partial y^*} = 0,$$

$$(21) \quad u^* \frac{\partial u^*}{\partial x^*} + v^* \frac{\partial u^*}{\partial y^*} = -\frac{\partial p^*}{\partial x^*} + \frac{1}{Re} \frac{\partial^2 u^*}{\partial y^{*2}},$$

$$(22) \quad u^* \frac{\partial T^*}{\partial x^*} + v^* \frac{\partial T^*}{\partial y^*} = \frac{1}{RePr} \frac{\partial^2 T^*}{\partial y^{*2}},$$

where $*$ denotes the dimensionless form of the respective variable, v is the velocity in y direction and $Pr = c_p \mu / \lambda$ is the Prandtl number. It is found, that for a negligible pressure gradient $\partial p^* / \partial x^* \approx 0$ and $Pr \approx 1$, Eq. (21) and Eq. (22) take the same form. With similar boundary conditions, the solution of these equations is equivalent. Hence, heat transfer and wall friction can be related by the Reynolds analogy [20]

$$(23) \quad \frac{2St}{C_f} \approx 1,$$

where $C_f = 2\tau_w / (\rho u_\infty)$ is the friction coefficient and St the dimensionless Stanton number defined as

$$(24) \quad St = \frac{Nu}{Re Pr}.$$

The Nusselt number is thereby given by

$$(25) \quad Nu = \frac{\alpha L_c}{\lambda}.$$

The right side of Eq. (23), is called the Reynolds analogy factor. It is equal to unity and approximately constant for laminar and turbulent flows [21]. The Reynolds analogy is valid for $Pr \approx 1$. For a wider

range of the Prandtl numbers $0.6 < Pr < 60$, the Chilton–Colburn analogy is introduced, in which the Reynolds analogy factor is corrected by the Prandtl number [22, 23]

$$(26) \quad \frac{2St}{C_f} \approx Pr^{-2/3}.$$

This consideration shows, that in addition to the heat transfer coefficient, the TDT signal is proportional to the wall shear stress $\Lambda \propto \alpha \propto \tau_w$ for negligible pressure gradients. In explicit form the relation between heat transfer coefficient and wall shear stress can be calculated from Eq. (26)

$$(27) \quad \tau_w \approx \alpha \frac{u_\infty}{c_p} Pr^{-2/3}.$$

2.2.2 Nusselt correlations

To validate the proportional relation of Λ and α , experiments on a flat plate are performed in this work. For this, a theoretical description of $\alpha(x)$ along a flat plate in laminar and turbulent flow is used. Following the analytical solution of the boundary layer equations of the previous section for flat plates derived by Blasius [24], and the similarity approach of thermal and velocity boundary layer, Eq. (26), the Nusselt correlation yields $\alpha(x)$ along the flat plate in laminar flow for a uniform temperature distribution [25]

$$(28) \quad \alpha_{\text{lam}}(x) = Nu_{x,\text{lam}} \frac{\lambda}{x} = 0.332 Re_x^{1/2} Pr^{1/3} \frac{\lambda}{x}.$$

For turbulent flow another dependency is derived empirically [13, 14]

$$(29) \quad \alpha_{\text{tur}}(x) = Nu_{x,\text{tur}} \frac{\lambda}{x} = 0.0296 Re_x^{4/5} Pr^{1/3} \frac{\lambda}{x}.$$

The dependencies of $\alpha_{\text{lam}}(x) \propto x^{-1/2}$ for laminar and $\alpha_{\text{tur}}(x) \propto x^{-1/5}$ for turbulent flow are shown in the bottom plot of Fig. 3 as dashed lines.

2.2.3 Non-uniform heating correction

In the previous sections it was shown that velocity and thermal boundary layer development are similar and can be used to interpret the TDT data as heat transfer coefficients and wall shear stresses under certain circumstances. Now, it is investigated how a non-uniform heating of the aerodynamic component affects the similarity of both boundary layers and therefore the interpretability of TDT data. The following summary is based on the work previously published in [A2].

Non-uniform heating in TDT occurs either due to spatial inhomogeneities in the radiant flux of the radiative source or due to limitations in the optical accessibility in a specific geometry. This can result

in step changes in the spatial wall temperature distribution after an unheated starting length and/or arbitrary temperature distributions. Their effect on the thermal boundary layer development has been intensively studied in the literature: for turbulent boundary layers without pressure gradient, Reynolds et al. [26] developed an integral boundary layer analysis for computing heat transfer from abrupt changes in wall temperature. Tribus and Klein and others [27, 28, 29] used the linearity of the energy equation of a steady flow to derive a superposition solution by regarding arbitrary temperature variations as infinitesimal step changes. Kays and Crawford [30] summarized these techniques for different flow applications in their textbook and built a numerical simulation tool for more complex flows. Hacker and Eaton [31] further developed the superposition technique using an experimentally determined Green's function to predict the effect of non-uniform temperature boundary conditions in flows with arbitrary pressure gradients.

For the interpretation of TDT data, a similarity between aerodynamic and thermal boundary layer is necessary. Due to non-uniform heating, the development of the thermal boundary layer during the measurement is delayed or distorted compared to the velocity boundary layer as illustrated in Fig. 5. Consequently, heat transfer (and similarly wall shear stress) distributions are measured inconsistently and must be corrected in the post-processing. For steady flows with zero pressure gradient, this correction can be computed using an integral boundary layer solution of the linear energy equation [30].

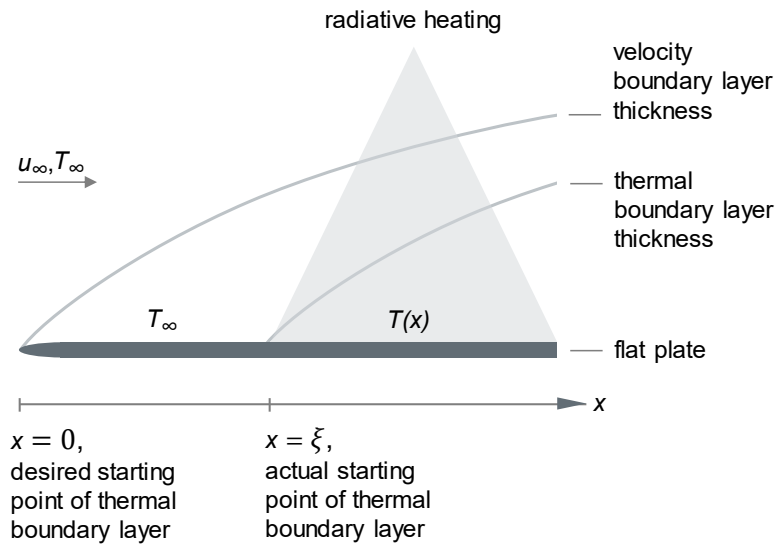


Figure 5 Schematic of the boundary layer development on a non-uniform heated flat plate with an unheated starting length. The image was modified from [A2].

To show this, it is assumed that local heat transfer coefficients are measured on a flat plate with coordinate x in flow direction and with a desired thermal boundary layer starting at $x = 0$. It is further assumed that due to certain circumstances (e.g. restricted optical accessibility or spatial stitching of multiple temperature decline measurements), laser heating can only start at $x = \xi$, with $\xi > 0$. Since the starting points of the desired and actual thermal boundary layer are shifted by ξ , stronger temperature gradients lead to higher heat transfer coefficients at $x \geq \xi$. To correct the offset between both boundary layers and compute the local Nusselt numbers $Nu_{x,0}$ with the heating area starting at $x = 0$, the measured $Nu_{x,\xi}$ can be corrected by the following equation for laminar flow:

$$(30) \quad g(\xi, x) \equiv \frac{Nu_{x,\xi}}{Nu_{x,0}} = \left(1 - \left(\frac{\xi}{x}\right)^{3/4}\right)^{-1/3}.$$

This correction is only valid if the temperature distribution follows a step function with the step being located at $x = \xi$. However, the edge of the heating area is a smooth temperature function rather than a sharp step and even within the heating area, the temperature distribution can be inhomogeneous. Kays and Crawford [30] describe a general theory for calculating heat transfer on a flat plate with arbitrary wall-temperature variations. Assuming a constant-property, constant free-stream velocity flow, infinitesimal changes in wall-temperature can be seen as step functions for which a solution $g(\xi, x)$ already exists (Eq. (30)). By superposing the solutions of these small changes, a general solution can be expressed as a Riemann integral and a summation over possible discontinuities in the temperature distribution:

$$(31) \quad \frac{Nu_{x,\xi}}{Nu_{x,0}} = \frac{1}{\Delta T} \int_0^x g(\xi, x) \frac{\partial T}{\partial \xi} d\xi + \sum_{i=1}^k g(\xi_i, x) \Delta T_i.$$

This relation enables the analytical correction of TDT data measured with a non-uniform heating area for aerodynamic components with negligible pressure gradient. The application and the results of this solution are shown in an experiment in Sec. 4.5.

2.3 Heat transfer and aerodynamics in turbomachinery

TDT is developed for stationary and high-speed applications. Due to the use of radiative heating and IR thermography, it enables fast, contactless measurements and can be integrated into complex geometries. This is particularly advantageous for flow visualizations on rotating components in turbomachines where conventional measurement techniques require high instrumentation effort or cannot be applied.

In Fig. 6, exemplarily a turbine blade is illustrated, which is exposed to an air flow. The surface consists of a suction side and a pressure side on which boundary layers develop.

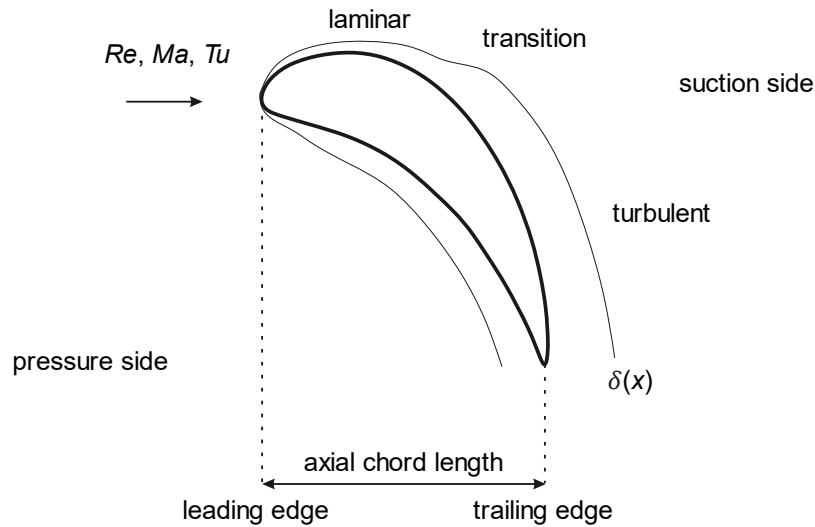


Figure 6 Illustration of a turbine blade exposed to a convective flow with a given Reynolds and Mach number and turbulence intensity. The boundary layer development is shown for suction and pressure side.

The aim in blade design is often to maintain the laminar boundary layer for as long as possible, since the heat and friction losses are lower than in a turbulent boundary layer. Under typical engine conditions, however, a transition to a turbulent boundary layer on the suction side of the blade cannot be avoided. In order to understand the dynamics, the transitional behavior has been intensively studied in the literature [17, 32, 33]. The development of the boundary layers is dependent on several parameters. Due to their large number and nonlinear interaction, a theoretical description of boundary layer development and particularly transition remains a complex task.

The aim of the following sections is to give an overview of the different modes of transition, which can occur in turbine flows and other convective phenomena, which influence the heat transfer distributions on turbine blades. Furthermore, the Reynolds analogy, introduced for flat-plate boundary layers, is revisited for turbine flow applications.

2.3.1 Laminar–turbulent transition

Mode and position of a boundary layer transition in turbine flows are influenced by several parameters. In addition to the Reynolds number, as described for flat-plate boundary layers, parameters like pressure gradient, free-stream turbulence and surface roughness are of particular importance.

For example, an adverse pressure gradient favors the development and amplification of free-stream perturbations in the laminar flow and results in earlier transition to turbulence. In contrast, a reduced pressure in an accelerated flow stabilizes the laminar boundary layer and the transition occurs further downstream [34, 35, 36]. A high free-stream turbulence leads to large disturbances in the laminar boundary layer which favors an early transition [37]. Also, different forms of surface roughnesses can lead to an earlier transition. In literature a distinction is drawn between single roughness elements and

distributed surface roughness. The surface roughness, characterized by the parameter k_s , is particularly important for TDT since high emissivity coatings often have an increased k_s compared to the base material of the aerodynamic component. Experiments in literature showed, that the transition position is significantly altered for a critical roughness Reynolds number above [18, 38, 39]

$$(32) \quad Re_{ks} \equiv \frac{u_\infty k_s}{\nu} > 120.$$

For values below this threshold, the effect of surface roughness is negligible, and the surface is assumed to be hydraulically smooth. In addition to these parameters, turbomachinery flows show periodic oscillations in the free-stream turbulence originating from wakes of upstream vane and blade rows. Also, three-dimensional vortex flows interact with the two-dimensional boundary layer and affect mode and location of the transitional behavior.

The mode of natural transition was already described for the flat-plate boundary layer in Sec. 2.1.2. It was assumed, that the turbulence intensity is small and has negligible effect on transition. In a turbine environment, turbulence intensities are typically in the order of 5 to 10 percent [17]. Together with the non-zero pressure gradients, flow acceleration due to the curved blade geometry and unsteady wakes of preceding vane rows, three additional modes of transition can occur in turbomachinery: bypass transition, separation-induced transition and wake-induced transition [33].

- The bypass transition is characterized by Klebanoff distortions, zones of jet-like streaks with spanwise periodicity, which emerge from free-stream disturbances, grow in downstream direction, and finally disintegrate into turbulent spots. Thereby, the mechanism of Tollmien-Schlichting instabilities is bypassed and the flow breakdown into turbulence is faster compared to natural transition. Bypass transition is observed for free-stream turbulence intensities above 0.5 to 1 percent [40, 41, 42].
- The separation-induced transition occurs in decelerated flows with adverse pressure gradients and low turbulence intensities in which the laminar boundary layer separates from the surface. A shear layer forms between laminar flow and separated region and gives rise to Kelvin-Helmholtz instabilities. These spanwise vortices become unstable further downstream and cause breakdown into turbulent flow. During or after transition, the flow may reattach and form a separation bubble. Such separation bubbles can also be found after tripping wires and backward facing steps and significantly reduce the heat transfer [43, 44, 45, 46].
- Wake-induced transition occurs in turbomachinery when a wake of an upstream vane hits the boundary layer of the blade. If the flow is attached to the surface, the transition to turbulence follows similar mechanisms as described for the bypass transition, due to the high turbulence intensity in wakes, typically in the order of 15 to 20 percent [17]. Wake-induced transitions in turbomachinery occur periodically and are generally shifted upstream

compared to the transition without the influence of a wake. Between two wakes, turbulence decays and the transitional state relaxes towards a laminar boundary layer, which shifts the transition further downstream. Hence, an unsteady, spatially oscillating transition is observed. The dynamics of wake–boundary layer interaction for different flow parameters and separated boundary layer are complex. A detailed description as well as experiments with varying turbulence intensities, Reynolds numbers and loading levels of the turbine can be found in [33, 47].

Since all modes of transition alter the heat transfer at the wall, the corresponding transition position can be detected with TDT. Examples of natural, separation–induced and bypass transition are observed in the experiments of this thesis.

2.3.2 Interaction of secondary vortex flow with the blade boundary layer

In turbomachinery, the blades and vanes are attached to an endwall at which a boundary layer develops. As this boundary layer approaches the junction of endwall and blade, the flow is separated from the wall and parts of boundary layer fluid and the main flow roll up into three–dimensional vortex structures, called the secondary flow. In addition to the losses induced by the two–dimensional blade boundary layer, secondary flow losses typically account for 30 – 50 % of the total aerodynamic losses in a blade row and have therefore been subject of extensive research efforts [48, 49, 50].

Due to their interaction with the blade boundary layer, they impose significant changes to the wall heat transfer and can therefore be detected and examined with TDT. Figure 7 illustrates the emergence of endwall vortex structures and their development across the blade passage based on the experiments of Wang et al. [51]. They examined a stationary cascade in which no unsteady wake effects of preceding vane or blade rows were considered. At the junction of endwall and blade, a horseshoe vortex system occurs consisting of a suction side and a pressure side leg. Moreover, smaller corner vortices are induced on either side. Within the passage, the pressure side horseshoe vortex moves towards the suction side and merges with the suction side leg from the adjacent blade. They build a stronger vortex called the passage vortex, which is gradually lifted from the endwall and moves into the channel. High heat and mass transfer is observed where the vortices meet the suction side wall of the blade and disturb the boundary layer [52].

In Fig. 7 only the lower endwall is depicted. Similar vortex generation occurs for an upper endwall. Particularly for unshrouded turbine blades with tip clearance, secondary flow effects result from the gap leakage flows, which additionally alter the wall heat flux on the suction side of the blade [53].

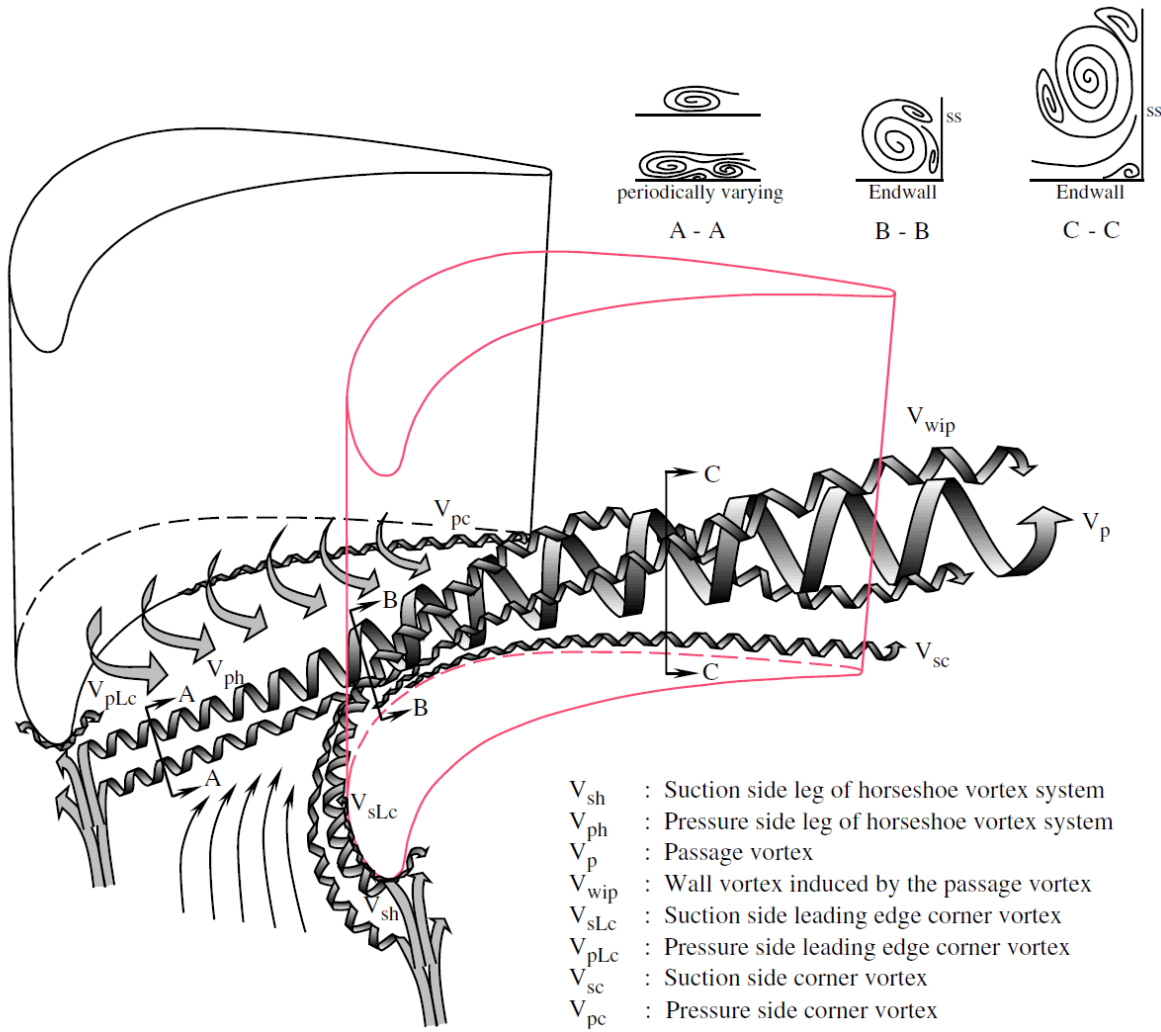


Figure 7 Illustration of vortex flow patterns in a turbine cascades taken from [51]

2.3.3 Validity of the Reynolds analogy on turbine blades

The validity of the Reynolds analogy was already discussed for flat-plate boundary layers. In quantitative TDT measurements, heat transfer coefficients can be converted into wall shear stresses, which helps to understand losses on aerodynamic components. However, for flows around gas turbine blades, some of the assumptions used to derive the Reynolds analogy are not generally valid. These are the pressure gradient and the free-stream turbulence are not negligible, and the surface might not be considered as hydraulically smooth. The validity of the Reynolds analogy in turbine flows is, however, often used in literature [54, 55]. Bons [21] therefore emphasizes the dependency of the Reynolds analogy factor on these parameters and states that when significant pressure gradient and surface roughness are present, their effects on the Reynolds factor add up and can lead to significant changes over a turbine blade. In contrast, when significant free-stream turbulence and surface roughness are present, their effects are opposed and can lead to negligible net changes to the Reynolds factor for small surface

roughnesses. According to Han and Goldstein, a constant analogy factor was found along the suction side of their turbine blade geometry for high turbulence intensities ($Tu = 8.5\%$), while the analogy factor changed for low turbulence values ($Tu = 0.2\%$). Yet, they did not specify the surface roughness of the blade [56].

This shows that a general description of the Reynolds analogy in turbine flows is still subject to further investigations and experiments [57]. For TDT it is concluded that a quantitative conversion of heat transfer coefficients to wall shear stresses in turbine flows must be considered with caution and is specific for every application.

2.4 IR detectors and imaging systems

IR sensors are used in TDT to measure the radiant flux emitted by a surface to non-invasively record the transient temperature after the energy pulse. In the following, relevant properties of IR sensors are described. Special attention is paid to the quantification of sensor noise, which is a limiting factor in some TDT applications. Furthermore, properties to estimate the optimal wavelength range of an IR detector for TDT measurements are described theoretically.

2.4.1 Absorption and detection of radiation in IR sensors

IR sensors are based on the absorption of the incident IR radiation. A photon in solid matter is absorbed when its energy is sufficiently high to excite electronic or vibrational states. The absorption of a photon can be detected by two different sensors, the thermal and photon sensor. If electronic or vibrational states are excited to a non-equilibrium state, their energy will dissipate and increase the temperature of the detector element. This temperature increase is then measured by changes in temperature-dependent physical properties of the detector, for example the changes in electrical resistance. This type of detector is called thermal sensor. Due to the relatively slow thermodynamic processes, these sensors typically have long response times (several milliseconds [10]).

For the measurement of temperature transients, a faster sensor type is required which is called photon detector. It consists of semiconductor materials, where photons can excite free charge carriers by the inner photoelectric effect. The free charge carrier density is increased, and a photocurrent is generated. Hence, the incident radiation is transduced into an electrical signal which is measured by the sensor.

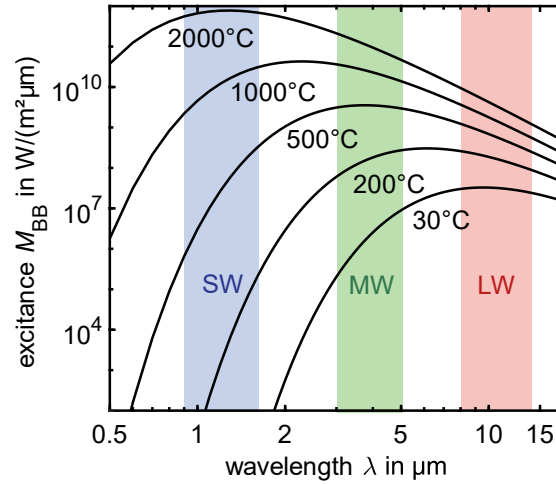


Figure 8 Excittance of a blackbody emitter for different temperatures according to Planck's law in double-logarithmic scale. The typical wavelength ranges are shown for IR sensors for short-wave (SW), mid-wave (MW) and long-wave (LW) IR radiation.

In semiconductors, free charge carriers can only be generated by photons within a limited energy and therefore wavelength range, which depends on the used semiconductor materials. Photon detectors are commonly split into three types of detectors, which are sensitive for short-wave (SW, $0.9\mu\text{m} < \lambda < 1.7\mu\text{m}$), mid-wave (MW, $3\mu\text{m} < \lambda < 5\mu\text{m}$) or long-wave (LW, $8\mu\text{m} < \lambda < 14\mu\text{m}$) IR radiation. Figure 8 shows the simulated temperature dependence of the spectrum emitted by a blackbody according to Planck's law (Eq. (8)). In addition, the wavelength bands of typical IR sensors are illustrated. The maximum frequency of the spectra is proportional to the increasing temperature (Wien's displacement law) which leads to a shift of the spectra to smaller wavelengths. Obviously, SW sensors are only suitable for high temperature measurements, because almost no IR radiation is emitted from objects at room temperature in the SW wavelength range. LW sensors receive most of the radiation at room temperature while for temperatures beyond 350°C , the excittance spectrum is shifted in favor of MW sensors [10].

2.4.2 Properties of IR imaging systems

Until now, the properties of only a single photon detector was analyzed. In IR imaging systems, several photon detectors, commonly known as pixel, are arranged in a focal plane array (FPA) which is often cooled to reduce noise. For modern IR cameras, 1280×1024 pixel with pixel areas of $15 \times 15\mu\text{m}$ is state of the art. An image of the surrounding is projected onto the FPA by a lens system. In the following, properties of IR imaging systems and the performance of the conversion of incident radiation into electrical signals are described.

2.4.2.1 Detectivity

The performance of an imaging sensor can be characterized by several parameters. One of the most relevant parameters is the specific spectral detectivity D_λ^* . It is defined by the reciprocal of the noise equivalent power NEP

$$(33) \quad D_\lambda^* = \frac{\sqrt{A_D \Delta f}}{NEP_\lambda},$$

where a normalization eliminates the dependence of the signal detection bandwidth Δf and detector area A_D . The wavelength dependent NEP_λ is defined as the necessary incident monochromatic radiant flux to produce a voltage, which is equal to the detector noise voltage (signal-to-noise ratio $SNR = 1$). As shown in Fig. 9, D_λ^* is dependent on sensor material and whether a thermal or photon sensor is used. The higher D_λ^* is, the less incident radiation is needed to produce a noise equivalent signal. Photon sensors, as used in this work, have higher detectivities compared to thermal sensors and show a variability of D_λ^* across their wavelength range [10, 58].

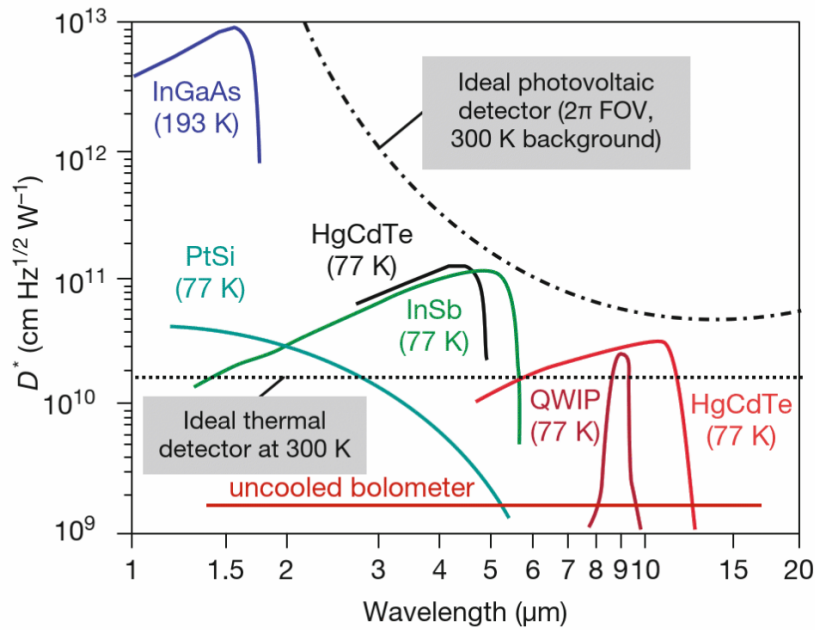


Figure 9 Specific spectral detectivity D_λ^* of several IR detectors. The dashed lines represent the theoretical limits for ideal photon and thermal detectors for hemispherical field of view (FOV) and 300K background temperature. The image is taken from [10].

2.4.2.2 Noise equivalent temperature difference

In IR imaging, several sources of noise are present, which can be classified as statistical and systematic noise sources. Systematic noise in an IR image can occur due to non-uniform properties of individual pixel, which result in the so-called fixed-pattern noise. Statistical shot noise is a consequence of the natural fluctuation of the number of photons received by the sensor. Only a ratio of these photons excites electronic states via the internal photoelectrical effect which again is a statistical process. Some electrons are emitted only by thermal processes without the influence of an external photon. This type of statistical noise is called dark shot noise. The electrons are stored within the pixel and read out after the exposure time. During the read-out process, another statistical noise term is added to the signal, the read-out noise [10, 59]. For the quantification of statistical sensor noise in IR measurements, the noise equivalent temperature difference $NETD$ is used. Like the NEP , it represents the temperature difference where a SNR of unity is achieved

$$(34) \quad NETD = \left(\frac{\partial \Phi}{\partial T} \right)^{-1} NEP.$$

After calculation of the derivative of $\partial \Phi(T)/\partial T$ and by considering the camera aperture $f\#$ and lens transmittance t_{lens} , the $NETD$ for a wavelength band $[\lambda_1, \lambda_2]$ takes the form [60]

$$(35) \quad NETD = \frac{4 (f\#)^2 \sqrt{\Delta f}}{\int_{\lambda_1}^{\lambda_2} t_{\text{lens}} \frac{\partial M_{\lambda, BB}}{\partial T_{BB}} D_{\lambda}^* d\lambda},$$

where the signal detection bandwidth is proportional to the reciprocal of the camera integration time $\Delta f \propto 1/t_{\text{int}}$.

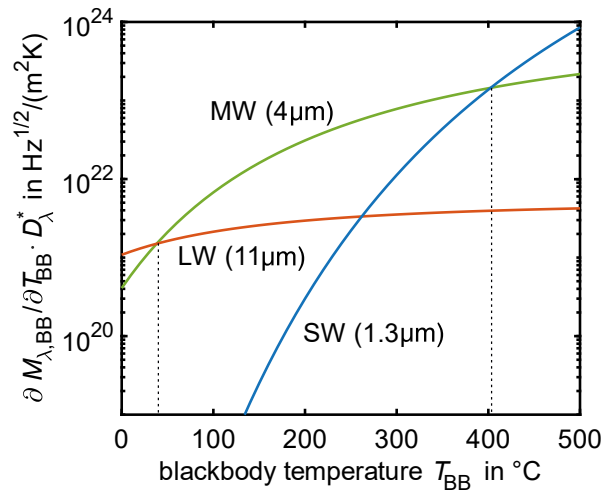


Figure 10 Monotonous increase of $\partial M_{\lambda, BB}/\partial T_{BB}$ multiplied by D_{λ}^* with object temperature. According to Eq. (35), the $NETD$ is reduced with increasing $\partial M_{\lambda, BB}/\partial T_{BB} D_{\lambda}^*$. Thus, the optimal wavelength range is identified for different object temperatures. The wavelength ranges for short-wave (SW), mid-wave (MW) and long-wave (LW) were approximated by their central wavelength.

Figure 10 shows the dependence of the object temperature on $\partial M_{\lambda, BB} / \partial T_{BB}$ multiplied by D_{λ}^* for different wavelengths. D_{λ}^* was derived exemplarily from Fig. 9 for InGaAs (SW), InSb (MW) and HgCdTe (LW) detectors. It is observed, that $\partial M_{\lambda, BB} / \partial T_{BB} D_{\lambda}^*$ monotonously increases with increasing object temperature which in turn reduces the *NETD* according to Eq. (35). Furthermore, it is found that the wavelength range of the sensor determines the maximum possible value of $\partial M_{\lambda, BB} / \partial T_{BB} D_{\lambda}^*$ and thus the minimum possible *NETD*. For example, to reduce the *NETD* it is optimal to use a LW sensor for object temperatures up to around 40°C, MW between 40°C – 400°C, and SW above 400°C. Here, the wavelength bands were approximated by their central wavelength.

2.4.2.3 Temperature contrast

In addition to the *NETD*, the temperature contrast within a wavelength range is a relevant parameter for the determination of the optimal wavelength range of an IR sensor for a specific measurement task. The temperature contrast is quantified by the relative change in excitance $dM_{\lambda, BB} / M_{\lambda, BB}$ which is caused by a relative change in temperature dT / T [61]. Differentiation of Eq. (8) with respect to T and approximation of the result for $c_1 / (\lambda T) \gg 1$ leads to

$$(36) \quad \frac{dM_{\lambda, BB} / dT}{M_{\lambda, BB}} = \frac{c_1}{\lambda T} \frac{e^{c_1 / (\lambda T)}}{e^{c_1 / (\lambda T)} - 1} \approx \frac{c_1}{\lambda T},$$

where $c_1 = hc/k$. It is observed that the temperature contrast increases for decreasing wavelengths and temperatures. Particularly, when comparing MW and LW sensors, an infinitesimal change in object temperature at room temperature results in a 2.69 larger relative change in MW radiation compared to LW radiation as found in [10]. For this approximation, again the central wavelengths of MW and LW range were used. A higher temperature contrast of the incident radiation is therefore achieved for MW and SW sensors.

In conclusion, the choice of an optimal wavelength range of an IR sensor is mainly dependent on the temperature range of the task. For temperatures near room temperature, LW sensors receive highest amounts of radiation, while MW and SW sensors provide higher temperature contrasts. Regarding the temperature noise, MW sensors outperform LW and SW sensors for applications between 40°C – 400°C due to their high specific detectivity and the available radiation.

Chapter 3

Temperature Decline Thermography

The following chapter is partly based on the work previously published in [A1, A2, A3, A4]. The author of this thesis would like to thank the co-authors for their valuable contributions. Especially relevant for this chapter are the contributions of Martin Stadlbauer on the initial idea to perform flow visualization using temperature decline rates; of Juergen Gruendmayer and Martin S. Sommer to develop the trigger control hardware and to support testing; of Andreas Zeisberger to design and build the pulse-stretcher optics; of Christian J. Kähler to provide helpful discussions during the experimental design, the analysis and interpretation of the data; of Jonathan Klimesch to support the implementation of the Matlab tools used for image analysis.

3.1 Methods for transition detection and flow visualization

During the last five decades, many measurement methods have been developed with the purpose of detecting the transitional behavior of boundary layers and visualizing near-wall flow effects. However, until now, it has not been possible to spatially visualize a laminar-turbulent transition on fast rotating gas turbine blades. The following is a brief overview of some of the most successful measurement approaches for transition detection and flow visualization. A distinction is drawn between mechanical, electrical, and optical methods which measure boundary layer phenomena in one or two spatial dimensions.

3.1.1 Mechanical approaches

One of the simplest mechanical approaches for flow visualization is based on thin wool threads which are stucked onto a body exposed to a flow. The threads align to the local flow direction and indicate areas of separated flow, transition to turbulence and the position of a stagnation point [62].

Another approach is the surface oil film technique which is often used for flow visualization [63, 64, 65]. It provides spatial information of near-wall boundary layer conditions from the patterns of

colored oil films deposited on the surface of aerodynamic components. This technique is relatively simple to apply on stationary parts like turbine cascades and vane stages but is limited in use for rotating applications due to the centrifugal forces on the pigments and the poor repeatability.

Both approaches are time consuming and may alter the near-wall flow behavior and hence the natural transition and separation locations. The spatial resolution of the wool threads is limited while the oil film approach leads to contamination in the facility and only provides a temporally integrated impression of the regions of interest.

3.1.2 Electrical approaches

Surface hot film anemometry is a widely used technique to detect laminar–turbulent transition and measure qualitative wall shear stresses on stationary parts along one direction [66, 67]. This method is also used in this work to validate TDT measurements. Surface hot films are thin electronically conductive elements with constant temperature control which measure the heat transfer from the wall surface to the flow and the corresponding wall shear stresses with a temporal resolution in the order of 10^4 Hz. For this, the voltage V required to maintain the constant temperature is recorded and analyzed according to [68]

$$(37) \quad \tau_w \propto \left(\frac{V^2 - V_0^2}{V_0^2} \right)^3,$$

where V_0 is the voltage of the reference measurement without flow. Surface hot film anemometry is well suited for the determination of boundary layer states since statistics of the temporal signal can be used to calculate the average position of a boundary layer transition. For this, second and third moment of the signal distribution, root mean squared (*RMS*) value and skewness (*SKEW*), can be used which are defined as

$$(38) \quad RMS = \sqrt{\frac{1}{N} \sum_{n=1}^N (\tau_{w,n} - \overline{\tau_w})^2},$$

$$(39) \quad SKEW = \frac{1}{RMS^3} \frac{1}{N} \sum_{n=1}^N (\tau_{w,n} - \overline{\tau_w})^3,$$

where $\tau_{w,n}$ is the shear stress measured in a single measurement period and $\overline{\tau_w}$ is the mean shear stress over N measurement periods defined by

$$(40) \quad \overline{\tau_w} = \frac{1}{N} \sum_{n=1}^N \tau_{w,n}.$$

The skewness is a measure of the asymmetry of a distribution and takes positive values for mostly laminar boundary layers with only a few turbulent disturbances and negative values for mostly turbulent boundary layers with remaining laminar parts. Across the transitional region, the skewness therefore

changes from zero in a fully laminar boundary layer to a maximum positive value for an intermittency of 25%, crosses the zero line for an intermittency of 50%, takes a minimum negative value for an intermittency of 75% and converges to zero for a fully turbulent boundary layer [68].

Despite the convenient ability to characterize the transitional region with statistical means, surface hot films have rarely been applied to rotor blades in turbomachinery [69]. This can be accounted to the need of a complex telemetry system for signal and power transmission to and from the rotor blades. Furthermore, the spatial resolution of the technique is limited by the number and spacing of the conductive elements and is therefore not adequate for validating numerical flow simulations.

3.1.3 Optical approaches

The advantages of optical based methods include a reduction of instrumentation effort, the minimized disturbance to the flow, and the high spatial resolution of modern imaging sensors. These sensors enable a highly accurate detection of the laminar–turbulent transition location and flow visualization. Therefore, the application of optical based measurement techniques is promising for turbomachinery applications.

Particle Image Velocimetry (PIV) and Laser–Doppler Velocimetry (LDV), for example, measure the velocity components of the flow based on the scattered light of tracer particles. The methods were successfully applied to complex turbine and compressor flows investigating stator–rotor interaction [7, 70], tip clearance [71] and vane stage flows [72]. For boundary layer analysis on rotor blades, however, the techniques are limited by the thin boundary layer thickness at high Reynolds numbers and the low tracer particle density near the wall. Furthermore, if high resolution data is required, PIV data is only available in a light–sheet plane or tiny 3D volume [6, 73], while LDV data is limited to a grid of individual measurement points.

Infrared Thermography (IT), Temperature Sensitive Paint (TSP) and Thermal Liquid Crystal (TLC) techniques on the other hand, use thermal traces of near–wall flows to measure heat transfer distributions and visualize boundary layer effects like laminar–turbulent transitions and flow separation [74, 75, 76, 77]. Applications of these methods range from the analysis of heat transfer processes on rotors [78] and measurements on rotating wind turbine blades [79] to boundary layer transition detection on the rotors of a hovering helicopter [80] and other rotor blade models [81]. Even unsteady boundary layer transition on pitching airfoils and free standing helicopter rotors was recently measured by Raffel et al. using Differential Infrared Thermography (DIT) [82, 83]. The airfoil is thereby continuously heated and two thermograms are recorded at two different transition positions. The recorded thermograms are subtracted and by a second measurement at a different time, onset and end of the transition positions are extracted from the resulting signals. Unsteady transitions were analyzed with a temporal resolution of up to 14 Hz.

All these studies investigate free standing moving parts with a good optical accessibility. However, in fast rotating turbine rigs the optical access is very limited which impedes heating and observation of the blades. In literature, the investigated surfaces are often actively heated by lamps or electric heating

elements or passively heated by changes in flow temperature [84]. In engine rig applications, these heating methods are associated with high instrumentation effort, have slow heat-up rates, or produce insufficient heating. Furthermore, IT measurements are susceptible to interfering reflections of surrounding components with different temperatures. In turbine rigs, this can cause erroneous transition detection and flow visualization. To bypass these effects, TDT was proposed for flow visualization [8]. It strongly reduces interfering reflections and effects of irregular surfaces and can therefore be used for transition detection and flow visualization even in hard-to-access areas like on rotating blades in turbomachinery where other methods fail.

Another advantage of optical methods like IT is their ability to measure quantitative heat transfer distributions. Generally, this can be done by developing a model of the heat transfer processes in the slab material and calculate heat transfer coefficients based on the measured transient temperatures. This approach is described by analytical and numerical models of Cook and Felderman [85], Kendall and Dixon [86] and Walker and Scott [87] with applications ranging from short-duration facilities [88] to film cooling experiments [89]. Further improvements of these techniques have been achieved by considering a full inverse analysis of the transient temperature behavior using multi-dimensional least-squares minimization [90, 91].

However, determining the specific thermo-physical constants can be prone to errors and sometimes not possible, as they can be temperature dependent. Therefore, another approach is tested in this thesis, which converts TDT data to quantitative heat transfer distributions by means of a calibration measurement. This work shows that TDT can be advantageously used in various applications ranging from the detection of transitions and flow visualization in difficult to access and rotating geometries to quantitative heat transfer measurements on various aerodynamic components.

3.2 Simulation of thermodynamic processes in TDT measurements

In the following sections, numerical simulations are carried out to describe the thermodynamic processes during a TDT measurement. The simplified conduction model which was described in Sec. 2.1.3.2 is extended to include the effect of heat loss due to a realistic, non-ideal insulation on the surface temperature. Furthermore, the measurement quantity of TDT, $\Lambda - \Lambda_{\text{ref}}$, is derived theoretically and correlated to the heat transfer coefficient.

To understand the dynamics of the temperature decline shortly after the energy pulse, an implicit one-dimensional numerical simulation was conducted which is described in Plehwe [92] and von Hoesslin et al. [A3]. It is based on the finite-difference method described by Binder and Schmidt [93] and solves the unsteady heat equation of Eq. (15) in a multi-layer system under a constant convection condition. Transient heat transfer processes could therefore be studied within coating and bulk material.

The simulation method assumes that radiative heat transport and lateral heat conduction is negligible compared to the convective heat flux. Radiative heat transport is negligible since only small temperature

changes near room temperature are considered. This also implies that only small lateral temperature differences are present, and the lateral heat flow is negligible. In the TDT experiments in the present work, both assumptions are therefore valid.

For the discussion of the heat transfer processes in a TDT measurement, a two-layer system consisting of a high-emissivity paint (coating 1) and an insulation layer (coating 2) on an aluminum substrate was simulated. Figure 11 shows a typical transient temperature decline after the energy pulse. On the left-hand side, the temperature distribution within the coating is shown for different times t . The position $y = 0$ mm represents the surface of the aerodynamic component which is exposed to forced convection with a heat transfer coefficient of $\alpha = 500 \text{ W}/(\text{m}^2\text{K})$. Shortly after the energy pulse at $t = 0$ ms, the heat is conducted from the uppermost molecule layers into the coating 1. Due to the high temperature gradients, unsteady conditions are observed. The thermal impulse propagates through the coating and reaches the insulation layer, which attenuates further heat flow into the aluminum substrate. After about 40 ms an almost constant temperature distribution is reached within coating 1 and a quasi-stationary state establishes for a few milliseconds. The heat inside the coating layer now serves as a heat reservoir for the ongoing convection into the flow. As described in Sec. 2.1.3.2, Astarita and Carlomagno [15] estimate the start of isothermal conditions at a Fourier number of $Fo > 0.5$. In the simulated case, this corresponds to an elapsed time of about 11 ms.

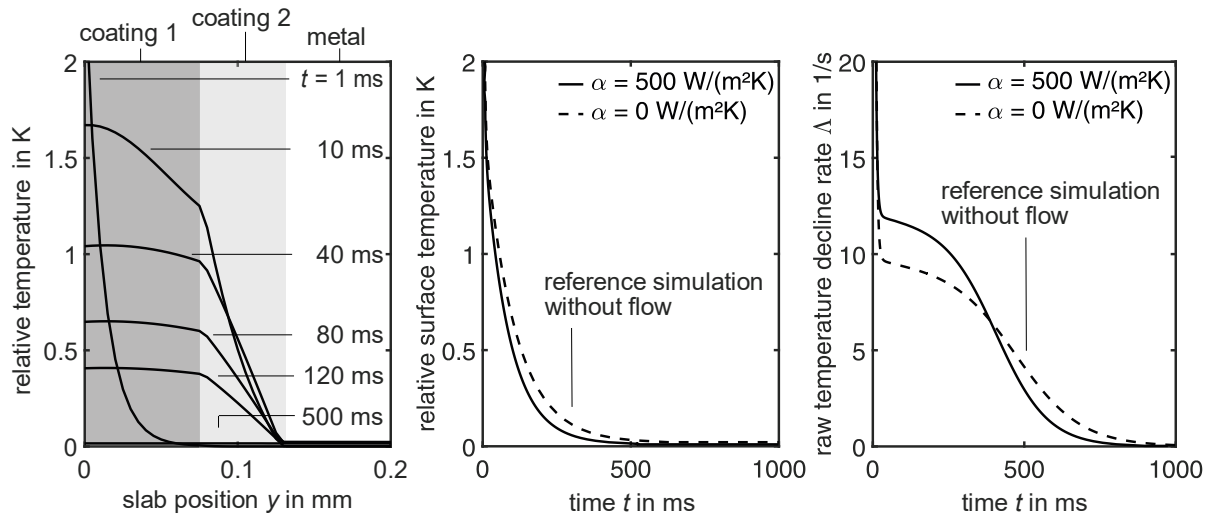


Figure 11 **Left** Simulation of the temperature distribution within coating system and metal substrate for different times t . The surface exposed to a convection boundary condition of $\alpha = 500 \text{ W}/(\text{m}^2\text{K})$ is at $y = 0$ mm. **Center** Temporal behavior of relative surface temperatures. The plot shows simulations with and without forced convection. **Right** Temperature decline rate Λ calculated from the temporal surface temperature behavior of the center diagram with and without forced convection.

The short time delay between the estimated start of the isothermal conditions of 11 ms and the simulated one of 40 ms is explained by the non-ideal insulation of coating 2 which was not considered by Astarita and Carlomagno and leads to a delayed development of isothermal conditions.

The center diagram of Fig. 11 shows the temporal temperature behavior at the surface $y = 0$ mm which strongly decreases during the first 500 ms. The plot on the right-hand side displays the temperature decline rate $\Lambda(t)$ which is calculated from the surface temperature data $\Delta T(t)$. In both diagrams a simulation without forced convection, $\Delta T_{\text{ref}}(t)$ and $\Lambda_{\text{ref}}(t)$, at $\alpha = 0$ W/(m²K) is plotted for comparison. During the first milliseconds $\Lambda(t)$ strongly decreases until a quasi-stationary state is reached where $\Lambda(t)$ is nearly constant. Due to forced convection on the surface, the heat stored in coating 1 is dissipated faster than without convection. This causes a stronger decrease of $\Lambda(t)$ compared to $\Lambda_{\text{ref}}(t)$ which intersect and converge to zero in the further course.

The quasi-stationary state of $\Lambda(t)$ is a key feature for the TDT analysis as it defines the time regime for the extraction of the temperature decline rate, which is then interpreted as the heat transfer coefficient. The proportional relation of the decline rate and heat transfer coefficient is essential and is observed after further analysis of the simulation results. First, $\Lambda_{\text{ref}}(t)$ is subtracted from $\Lambda(t)$. This is done to correct for conduction losses, which will be further discussed in Sec. 3.3. The resulting temperature decline curve $\Lambda(t) - \Lambda_{\text{ref}}(t)$ is shown on the left-hand side of Fig. 12 for different heat transfer coefficients between $\alpha \in [0, 3000]$ W/(m²K). $\Lambda - \Lambda_{\text{ref}}$ is extracted exemplarily from four different time steps t for every α and plotted as a function of α in the right-hand side of Fig. 12.

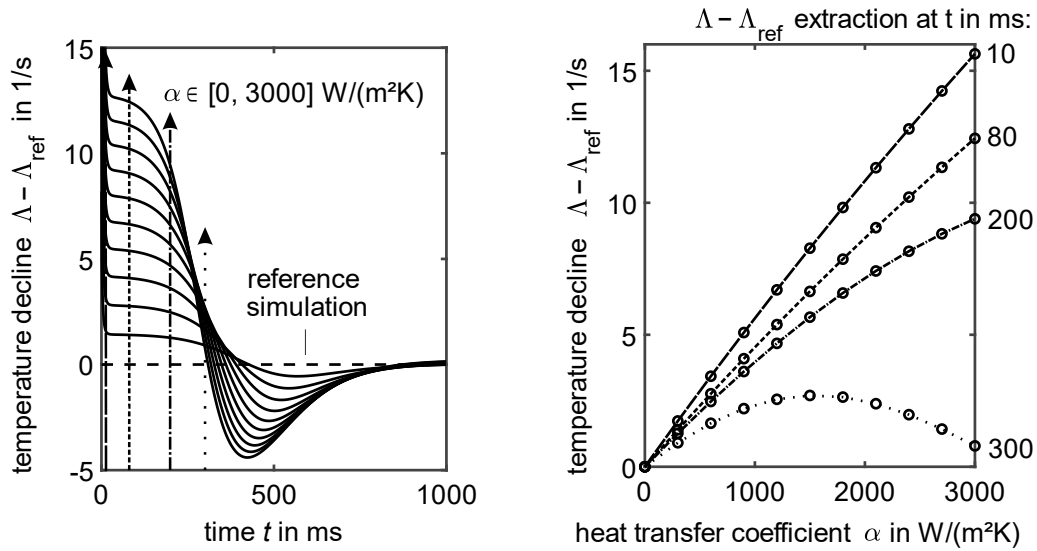


Figure 12 **Left** Simulation of the temperature decline $\Lambda - \Lambda_{\text{ref}}$ for different heat transfer coefficients. The reference temperature decline rate without forced convection ($\alpha = 0$ W/(m²K)) is defined as Λ_{ref} . **Right** Extraction of the temperature decline $\Lambda - \Lambda_{\text{ref}}$ from different time regimes from the left-hand plot. A quasi-linear relation between $\Lambda - \Lambda_{\text{ref}}$ and α is predicted for extraction times within the quasi-stationary regime.

A linear relation between $\Lambda - \Lambda_{\text{ref}}$ and α is observed for data extraction shortly before and within the quasi-stationary regime (at $t = 10$ ms and 80 ms). In contrast, if $\Lambda - \Lambda_{\text{ref}}$ is extracted after the quasi-stationary regime (at $t = 200$ ms and 300 ms), the non-linearity increases until the relationship loses its monotonous character and is no longer a bijective relation. Particularly, a calibration of $\Lambda - \Lambda_{\text{ref}}$ and α is then no longer possible.

From the left-hand side of Fig. 12 it is apparent, that within the quasi-stationary regime the difference between the decline rates for different convection conditions is pronounced and there is a high sensitivity of $\Lambda(t) - \Lambda_{\text{ref}}(t)$ to changes in α . An extraction of $\Lambda - \Lambda_{\text{ref}}$ from this time regime will therefore result in high contrasts in the TDT image, whereas an extraction of $\Lambda - \Lambda_{\text{ref}}$ after this time interval will result in a lower sensitivity and therefore less contrasts in the TDT image.

To conclude, the simulations allow a detailed analysis of the thermodynamic processes in a two-layer coating system after an energy pulse. Despite the non-ideal insulation of realistic systems, an isothermal condition develops like in the described idealized model of Sec. 2.1.3.2. Shortly after the energy pulse, when the isothermal condition is already established, a quasi-stationary regime of the temperature decline rate is observed. Data extracted from this regime provide a high sensitivity to the convective conditions at the surface and yield a proportional relation to heat transfer coefficients. A comparison of the simulation to experimental data is discussed in Sec. 3.5.2.

3.3 Theoretical derivation of the temperature decline rate

The aim of this section is to theoretically motivate the calculation of the temperature decline rate and to derive the linear relationship of $\Lambda - \Lambda_{\text{ref}}(\alpha)$ which was found in the simulation results. The description follows the simplified model introduced in Sec. 2.1.3.2 and additionally considers conduction losses through the insulating layer since they cannot be neglected for realistic systems. It is assumed that the evaluation of the decline rates is performed within the quasi-stationary regime of $\Lambda(t) - \Lambda_{\text{ref}}(t)$. Here, the temperature decline on the surface takes place due to a combination of heat fluxes including convection into the flow \dot{q}_{conv} and conduction into the substrate material \dot{q}_{cond} . Losses due to radiation are assumed to be negligible.

$$(41) \quad \dot{q} = \dot{q}_{\text{conv}} + \dot{q}_{\text{cond}}.$$

The surface temperature rise $\Delta T_0 = T - T_{\text{aw}}$, with T_{aw} as the adiabatic wall temperature is proportional to the pulse energy q_{pulse} according to the conservation of energy

$$(42) \quad \Delta T_0 = \frac{q_{\text{pulse}}}{C}.$$

Here, $C = sd$ is a proportionality constant containing the volumetric heat capacity s of the coating, while d corresponds to the coating thickness. Within the quasi-stationary regime, the spatial temperature within the coating is almost constant and the isothermal assumption is fulfilled. Newton's law of cooling (Eq. (11)) can be used which results in the differential equation

$$(43) \quad \Delta \dot{T} = \frac{1}{C} (\alpha \Delta T + \dot{q}_{\text{cond}}).$$

The rearrangement of this equation for the convective heat transfer coefficient yields

$$(44) \quad \alpha = C \frac{\Delta \dot{T}}{\Delta T} - \frac{\dot{q}_{\text{cond}}}{\Delta T} = C\Lambda - \frac{\dot{q}_{\text{cond}}}{\Delta T}.$$

The term $\Lambda = \Delta \dot{T} / \Delta T$ represents the temperature decline rate. Assuming constant α , Λ can be considered as constant only if \dot{q}_{cond} is linear in ΔT which is true for small temperature changes present across the coating system.

By setting the forced convection to zero, a reference measurement is performed which is subtracted from the measurement with forced convection. In this case, the temperature decline is governed by natural convection and conduction into the base material

$$(45) \quad C\Lambda_{\text{ref}} = \frac{\dot{q}_{\text{cond,ref}}}{\Delta T_{\text{ref}}} + \alpha_{\text{nat}}.$$

Quantities relating to the reference measurement are indexed with “ref”, α_{nat} is the heat transfer coefficient of natural convection. The reference measurement serves mainly as correction for spurious reflections, inhomogeneous heating and varying coating thicknesses as observed in von Hoesslin et al. [A3]. For sufficiently small heat transfer coefficients, it reduces systematical errors due to conduction losses

$$(46) \quad \alpha = C(\Lambda - \Lambda_{\text{ref}}) + \alpha_{\text{nat}} + f_{\text{cond}}(\alpha),$$

with $f_{\text{cond}}(\alpha) = (\dot{q}_{\text{cond,ref}} / \Delta T_{\text{ref}} - \dot{q}_{\text{cond}}(\alpha) / \Delta T(\alpha))$.

For small α , $\dot{q}_{\text{cond}}(\alpha) / \Delta T(\alpha)$ is approximately linear in α and thus $f_{\text{cond}}(\alpha) \propto \alpha$. This leads to a linear relation between decline rates and heat transfer coefficients

$$(47) \quad \alpha = C'(\Lambda - \Lambda_{\text{ref}}) + \alpha',$$

with C' and α' containing material parameters, conduction coefficients of the reference measurement and natural convection, respectively. A slight deviation from linearity of the calibration relation is observed on the right-hand side of Fig. 12 for an analysis at 80 ms. It is accounted to the deviation from the linear behavior of $\dot{q}_{\text{cond}}(\alpha) / \Delta T(\alpha)$ for large α values.

The linear relation of Eq. (47) is used in this study to qualitatively visualize heat transfer phenomena based on the measured decline rates and to quantitatively access heat transfer coefficients by means of a calibration measurement.

3.4 Experimental procedure and data analysis

In the following section, a general overview of the required measurement components and the experimental procedure is given to measure the temperature decline after an energy pulse. TDT applications are thereby divided into two areas: measurements on stationary and on rotating aerodynamic components. Rotating applications generally place higher demands on measurement setup and procedure since shorter measurement times lead to an increased noise level and a precise triggering is necessary. The general setup, and the experimental procedure of a TDT measurement are described for the application in stationary systems and in a rotating turbine environment. The data analysis is detailed and general rules for data quality enhancement and noise reduction are derived.

3.4.1 Measurement setup

The measurement components used for stationary and rotating applications are similar. In general, the TDT technique requires four measurement components:

1. an aerodynamic component with high surface emissivities and low heat conductance in an air flow,
2. a radiative energy source for pulsed heating of the aerodynamic component,
3. an infrared imager to record the temperature decline of the surface,
4. and a trigger control which individually triggers energy source and infrared imager.

In a stationary setup, the components are arranged as illustrated in Fig. 1. For a rotating application, differences occur due to the limited space for instrumentation, the achievable data quality, the timing of heating and image acquisition, and the measurement procedure.

Fig. 13 exemplarily shows a measurement setup in a turbine rig. Like in the stationary case, the rotating component is coated with a low conductivity and a high emissivity paint. Here, the coating system must resist additional centrifugal forces. In fast-rotating devices the space is often limited by a casing which requires optical probes for radiative heating and image acquisition. In the turbine rig shown in Fig. 13, optical access to the rotating blade is provided only via boreholes in the casing at certain circumferential positions. Compared to open geometries, the radiant power through these probes is reduced. A further loss of sensor signal results from a shorter integration time, which is limited by the movement of the rotating blade.

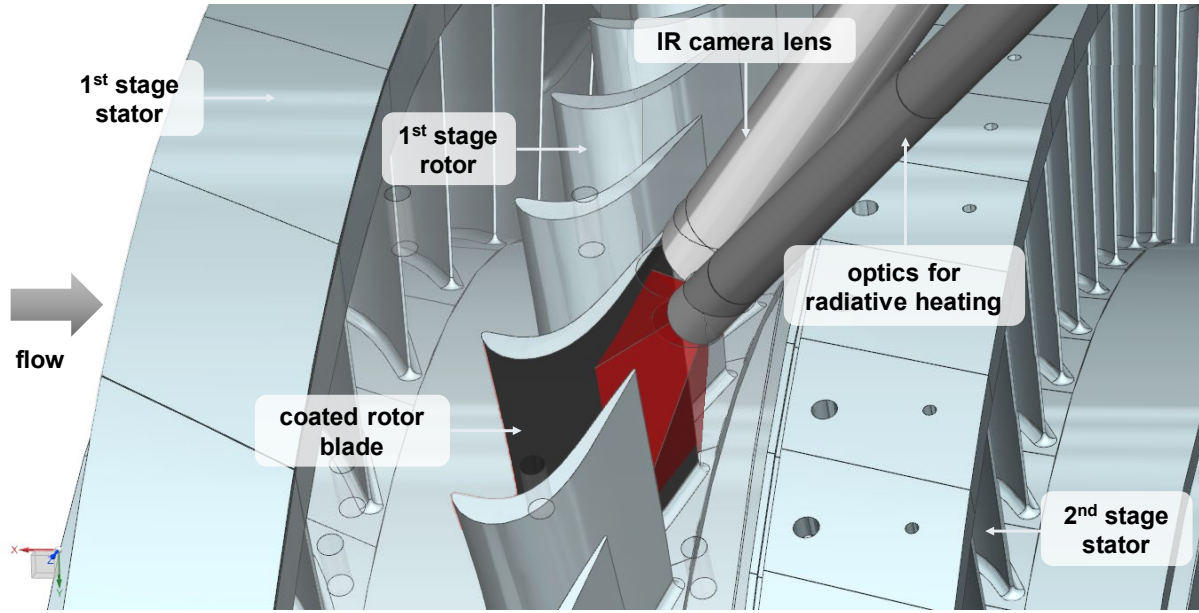


Figure 13 Schematic of the TDT measurement setup in a turbine rig. The casing of the rotor stage is shown transparent for better visualization. Optical access is only provided via two boreholes in the casing. The image was modified from [A1].

Here, a trade-off must be found between a long sensor integration time for better image quality and a small motion blur for a higher spatial resolution. In this study, the integration time for the measurement on a rotating blade is two orders of magnitude lower than in a stationary system.

To compensate for the reduced sensor signal, multiple measurements are recorded and averaged in the post-processing. To avoid position displacements of the blade and artifacts in the averaged image, the rotating blade must be at the exact same position for every energy pulse and camera image acquisition. Hence, a precise trigger control with low jitter is used which synchronizes the energy source and the camera with the rotating measurement blade.

3.4.2 Temperature decline measurement with flow

A TDT measurement consists of three measurement steps. First, the temperature decline measurement with flow is performed, followed by a reference measurement without flow. In the third step, an image of a position reference is recorded which is necessary for spatial position assignment and geometrical distortion correction in the post-processing. The TDT measurement with flow consists of a sequence of N images with intensity values $I(x, y)$. Since only small temperature changes are applied by the radiative heating, the intensity values of the infrared image can be considered proportional to temperature, hence $I(x, y) \propto T(x, y)$. One sequence contains N_0 offset images ($I_n(x, y)$ with $n \in [-(N_0 - 1), 0]$) before the heating and $N_T = N - N_0$ images ($I_n(x, y)$ with $n \in [1, N_T]$) after the heating. The images of a sequence are shown together with a typical temperature decline curve in Fig. 14.

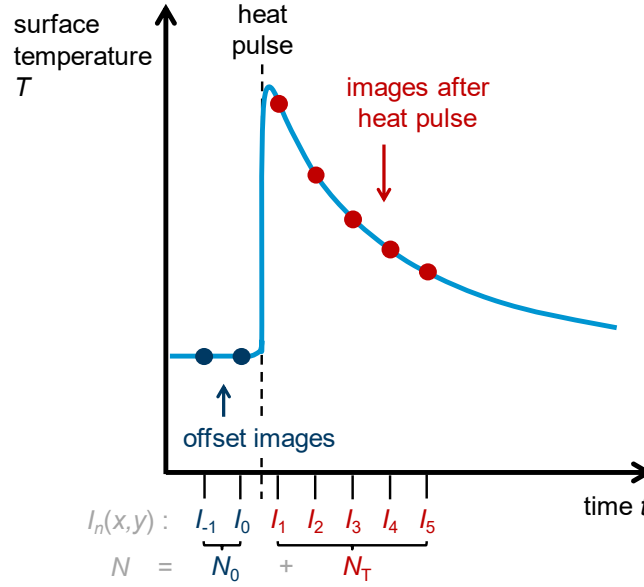


Figure 14 Schematic of a surface temperature decline after an energy pulse. For images recorded before the energy pulse, the term “offset images” is used together with negative indices including zero. Images after the energy pulse are indexed with positive numbers. In this example, $N_T = 5$ and $N_0 = 2$.

For the measurement, a minimum number of offset images $N_0 \geq 1$ and images on the temperature decline $N_T \geq 2$ are required. The offset images are used to determine the adiabatic wall temperature. From the images after the energy pulse, the temperature decline rates are calculated for every pixel. In a stationary measurement, the number of images is thereby only limited by the maximum image acquisition frequency of the camera. In the turbine application, camera and energy source are fixed at a certain circumferential position, so that only one image per revolution is recorded. The image acquisition frequency is therefore fixed at the turbine frequency and less images on the temperature transient are recorded. To reduce noise in the resulting TDT image, M measurements are recorded and the resulting image sequences $I^m(x, y)$, $m \in [1, M]$, are ensemble averaged in the post-processing.

3.4.3 Reference measurement without flow

A reference measurement without flow is recorded using the same settings as in the measurement with flow. In a rotating application, a reference measurement is performed on a stationary blade where forced convection is zero. To correctly subtract the reference measurement from the measurement with flow, the blade must be rotated manually into the measurement position. Compared to the measurement with flow, there is no motion blur in the reference measurement which leads to erroneous artifacts after subtracting both images. By adding an artificial motion blur to the reference image in the post-processing, the artifacts can be reduced which will be discussed in Sec. 3.4.5.

3.4.4 Position reference acquisition

Due to limited optical accessibility, curved surfaces and lens aberrations, the recorded image of the measurement object is often geometrically distorted and measurement positions are undefined. A position reference image is necessary for geometric distortion correction and spatial referencing in the post-processing. For this, an image of a reference object at the same position and with the same camera view as the actual measurement object is captured. A known length scale and reference points are applied on the reference object for correlating all camera pixel with the spatial coordinate system of the object. Hence, a correction for geometric distortion can be calculated. For stationary measurements, an equidistant grid is printed on paper and applied onto the object as position reference. In the turbine application, the accessibility is limited once the turbine is assembled. This implies that the measurement with flow and the position reference image must be recorded on separate blades. Figure 15 shows the reference blade which was used for turbine measurements. A specially prepared foil with elliptic holes and high emissivity coating is applied onto the surface of the blade to create strong contrasts in the infrared image. Here, contrast is generated by differences in emissivity of coating and underlying aluminum, as well as temperature differences between absorbing coating and reflecting metal. The position of the reference points is measured in x and y direction for 3D model mapping which is further described in the following section.

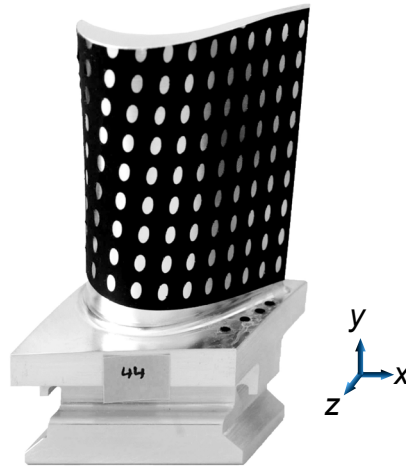


Figure 15 Photograph of the position reference blade of the turbine measurement. The black markers on the endwall provide additional reference points.

3.4.5 Image post-processing

Once the measurement is carried out, the recorded data is evaluated in four image post-processing steps. The first three steps are primarily used for data and noise reduction and to generate the TDT image. The last step corrects for the potentially distorted camera view and lens aberrations and maps the TDT image onto the geometry of the component. Figure 16 illustrates the effect of the first three post-processing steps on single pixel data.

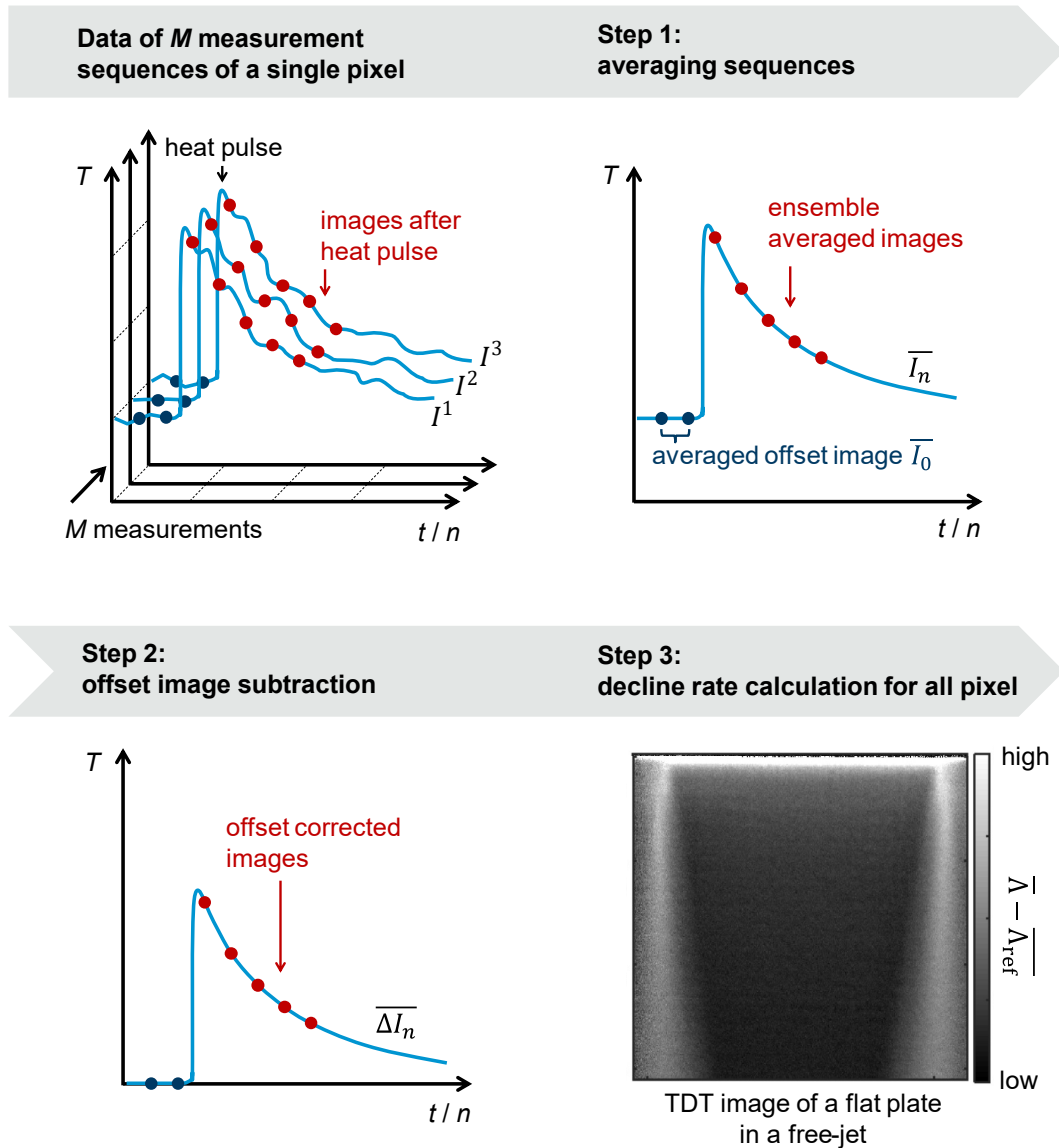


Figure 16 First three steps of TDT image post-processing. The plots in the top and bottom-left illustrate the post-processing steps on a typical temperature decline curve which was extracted from a single pixel. The dots represent the recorded measurement values I_n while the solid line illustrates the continuous temperature transient $I(t)$. The x -axis represents time or image number, respectively. The bottom-right plot shows the calculated temperature decline rates for every pixel. As an example, the TDT image of a flat plate in a free-jet facility is depicted, where bright areas correspond to areas with high temperature decline rates and heat transfer coefficients.

Step 1: average multiple measurements

In the first step, the temperature decline signals of M individual measurements are ensemble averaged which reduces the IR image sequences into a single sequence with reduced noise,

$$(48) \quad \overline{I_n(x, y)} = \frac{1}{M} \sum_{m=1}^M I_n^m(x, y),$$

for every image with index n in the sequence. Every pixel position (x, y) is analyzed individually. For better readability, the x, y dependence is abbreviated in the following using $I_n(x, y) = I_n$, which implies that the following equations are applied on every pixel in the IR image.

Step 2: subtract the offset image from the image sequence

In the next step, the offset images which are recorded before the laser heating, are averaged in time, and subtracted from every image of the sequence.

$$(49) \quad \overline{\Delta I_n} = \overline{I_n} - \overline{I_0},$$

for every n , with

$$(50) \quad \overline{I_0} = \frac{1}{N_0} \sum_{-(N_0-1)}^0 \overline{I_n}.$$

$\overline{I_0}$ thereby corresponds to the adiabatic wall temperature T_{aw} . Particularly for images with low signal and high noise level, the offset correction significantly reduces systematic sensor effects such as fixed pattern noise which is present in every image of the sequence. If sensor related artefacts, like periodically occurring lines, are still visible, Fourier filtering can be effectively applied.

Step 3: calculate temperature decline rates for every pixel

The third step is the actual TDT analysis where temperature decline rates are calculated from the sequence of every pixel. Within this step the averaged, offset corrected IR image sequence is reduced to a single TDT image where temperature decline rates are displayed as intensity values. For this, the differential equation of Eq. (43) is solved which yields a rule for calculating the decline rates from subsequent IR images. In a discrete formulation, this rule is given as

$$(51) \quad \Lambda_n = \frac{1}{\Delta t} \ln \left(\frac{\overline{\Delta I_{n+1}}}{\overline{\Delta I_n}} \right).$$

It is applied to the measurement with flow as well as the reference measurement, resulting in $\Lambda_{ref, n}$. As proposed in Sec. 3.3, the reference measurement is then subtracted from Λ_n . Figure 17 illustrates a double-logarithmic representation of the typical development of the decline rate $\Lambda(t) - \Lambda_{ref}(t)$.

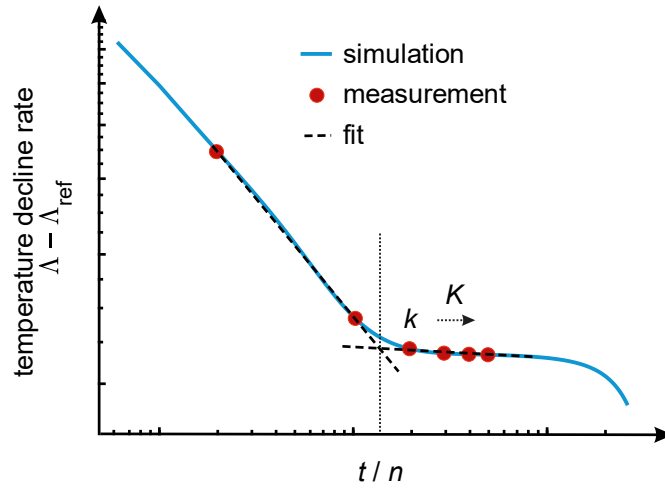


Figure 17 Double-logarithmic plot of the simulated temperature decline rate $\Lambda(t) - \Lambda_{\text{ref}}(t)$ versus time and image number. Measurement points are illustrated as circles. The first image of the analysis interval with index $n = k$ is defined by the first data point after the intersection of two best-fit lines before and within the quasi-stationary region.

As discussed in Sec. 3.2, a quasi-stationary regime of $\Lambda(t) - \Lambda_{\text{ref}}(t)$ is observed for a short period of time. For the extraction of the decline rates used in the TDT image, K decline rates from the quasi-stationary regime are extracted and averaged

$$(52) \quad \Lambda - \Lambda_{\text{ref}} = \frac{1}{K} \sum_{n=k}^{k+K} \Lambda_n - \Lambda_{\text{ref},n}.$$

To identify the start of the quasi-stationary regime at $n = k$ linear least-square fits before and within the quasi-stationary region are used. k is then defined as the next data point after the intersection point of both lines as shown in Fig. 17. The length of the extraction interval K , is more difficult to define since K strongly depends on the noise of the temperature decline. In practice, it is possible to find the optimal K manually, by searching for the minimal noise level in the TDT image. A theoretical estimation of K for optimal noise reduction is derived in Sec. 3.4.6.

Step 4: assign pixel locations to the model coordinate system

In the last post-processing step, the resulting TDT image is mapped onto the geometry of the aerodynamic component. Figure 18 shows an example of this step for the turbine blade measurement. The left-hand side displays a thermogram of the reference blade image in the inclined view of the camera.

The holes, arranged on an equidistant grid, are used to map the geometrically distorted camera image onto a 2D grid (Fig. 18, center) using the Matlab functions *cpselect* and *fitgeotrans* with polynomial transformation. The resulting rectified image is then mapped onto a 3D blade model (Fig. 18, right-hand side).

Step 4:
spatial assignment of pixel coordinates to model coordinates

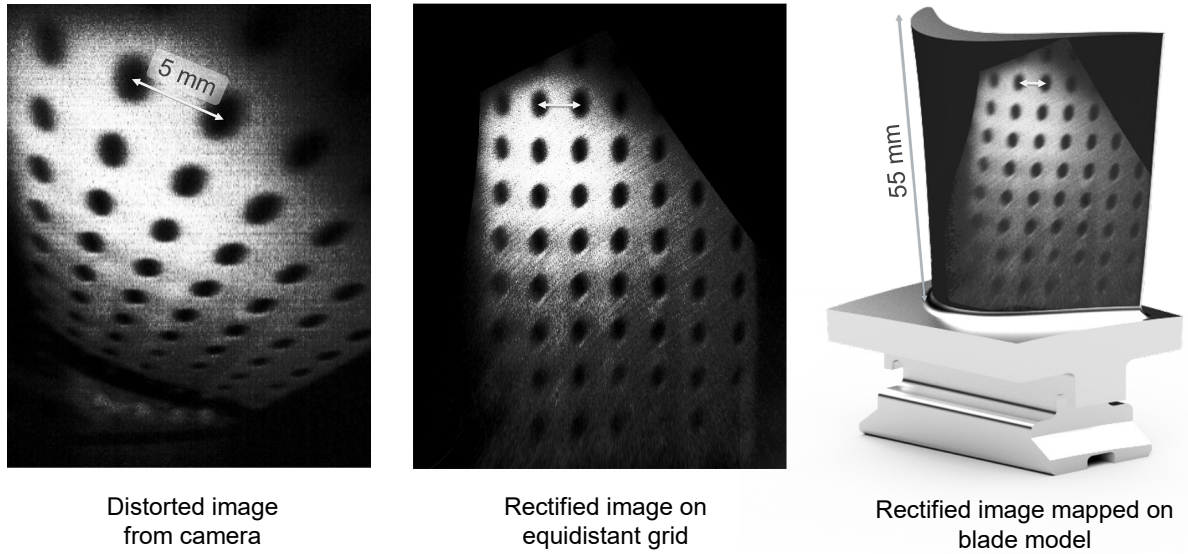


Figure 18 Registration of the reference rotor blade image with position pattern. The image was taken at a turbine frequency of 3500 rpm (around 95 m/s averaged tangential velocity) with a sensor exposure time of $10\ \mu\text{s}$ shortly after the laser heating. The same transformations used here can be applied to TDT images of the actual measurement blade without positioning holes. The image was modified from [A1].

This requires the positions of the previously measured holes on the blade. The transformations found during the registration of the reference blade can then be used to dewarp the actual TDT measurement.

During a reference measurement, the aerodynamic component is not moved. In a rotating TDT application, the motion blur of the reference measurement is therefore zero and differs from the measurement with rotation. A subtraction of both would result in systematic artefacts and may distort the visualization. This error can be reduced by artificially blurring the reference measurement by imitating the motion blur of the measurement with rotation. The blurred image is mathematically described by a convolution of the undisturbed image with a time-invariant impulse response called point-spread function. The point-spread function specifies how the intensity of a single pixel is distributed over multiple pixel during blurring. It is experimentally determined from the position reference measurement. Since the length in pixel of the reference holes is known from the stationary reference measurement, the length of the blurred holes in the rotating measurement is used to identify length and direction of the point-spread function as shown in Fig. 19. The reference measurement is then convoluted with the resulting point-spread function.

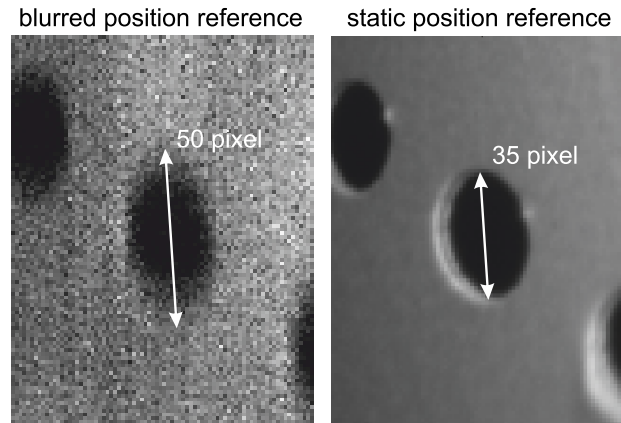


Figure 19 Comparison of moving and stationary position reference. The length of the point spread function is determined by the difference between the lengths of both ellipses. Both images are taken with different exposure times (**Left** 10 μ s, **right**: 1286 μ s) resulting in differences in data quality.

3.4.6 Measurement error sources and data quality enhancement

For a TDT measurement, several error sources can be identified. They determine the accuracy of quantitative heat transfer measurements and the localization of boundary layer phenomena in a TDT measurement. In the following, the error sources occurring in a TDT measurement are described and a quantitative error propagation is conducted for the post-processing steps of the TDT analysis. Practical measures for data quality enhancement are derived.

3.4.6.1 Measurement error sources

In general, error sources can be classified into random and systematic measurement errors. In infrared thermography, random error sources are mainly introduced by the electronic and thermal effects in the camera sensor and the natural photonic shot noise. The noise leads to statistical fluctuations of the intensity signal of a sensor pixel and the temperature signal.

Systematic error sources result from the temperature calibration which is determined for the radiative measurement path and for different integration times. Additional systematic errors are generated by instabilities in the cooling system of the sensor, inaccuracies in the determination of the emissivity of the target material and interfering ambient radiation arriving at the sensor [94]. Systematic errors cause a bias of the measured pixel signal.

A TDT measurement differs from a typical thermographic temperature measurement in that only relative changes of the pixel intensities are used for analysis. Consequently, some of the mentioned systematic error sources cancel out and can therefore be neglected. For example, all calibration related errors can be neglected since no calibration is necessary in a TDT measurement where raw intensity

signals are analyzed. Furthermore, due to the short duration of a measurement, low-frequency thermal instabilities of the sensor as well as quasi-stationary reflections or interfering radiation of the surrounding can be neglected. Particularly important is the fact that the emissivity of the target material has no influence on the mean TDT signal, since the relative analysis of Eq. (51) eliminates the influence of the emissivity. Therefore, a not exactly known or viewing angle dependent emissivity induces no additional systematic error to the measurement. However, as will be seen in the following section, a low emissivity increases the statistical noise in the TDT image.

In addition to pixel intensity errors, spatial errors must be considered in a TDT image. When TDT is used to localize boundary layer effects such as laminar-turbulent transitions, a main error source is the reprojection error, which is introduced during the correction of spatial distortions in the image (Step 4 of the image post-processing). This error describes the Euclidean distance of projected and measured pixel position and quantifies the deviation from the true image projection. Other error sources result from the accuracy of the reference grid application (as described in Sec. 3.4.4), and optical distortions such as spatial blurring due to the natural point spread function of the optics and a limited depth of field. Particularly for large viewing angles between camera and target, areas outside the focus distance appear blurred. In rotating applications, further spatial errors are induced by the jitter of the trigger control and the motion blur during the integration time of the sensor.

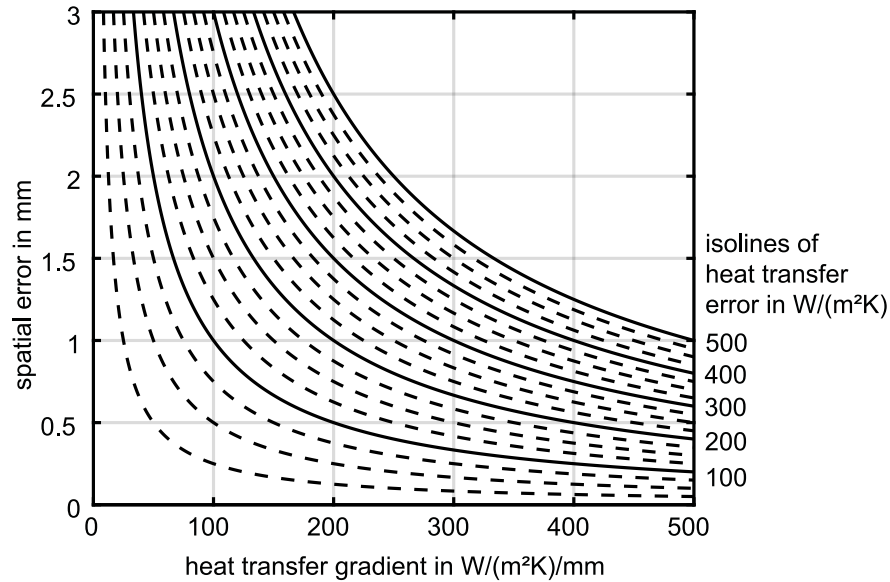


Figure 20 Isolines of the heat transfer error $\Delta\alpha$ caused by a spatial error Δx in the measurement. $\Delta\alpha$ increases for larger Δx and for steeper heat transfer gradients $\partial\alpha(x_0)/\partial x$ at the measurement position x_0 as described by Eq. (53).

These error sources lead to an uncertainty in the spatial determination of flow effects and smooth the measured heat transfer values in regions with strong heat transfer gradients as discussed in [95]. For quantitative heat transfer measurements, the total spatial error Δx in x -direction is correlated to a systematic error in the measured heat transfer coefficient $\Delta\alpha$ at a certain position x_0 . This systematic error is dependent on the gradient in heat transfer at this position and can be calculated by

$$(53) \quad \Delta\alpha(x_0) = \left| \Delta x \frac{\partial\alpha(x_0)}{\partial x} \right|.$$

Figure 20 shows the isolines of $\Delta\alpha$ calculated by Eq. (53) for graphical assessment.

3.4.6.2 Data quality enhancement

In contrast to most systematic error sources which have negligible influence on a TDT measurement, the random error sources strongly determine the image noise. Particularly in rotating measurements the *SNR* of the resulting TDT image is typically low. Compared to a stationary measurement in an easily accessible geometry, the radiant power received by the sensor is attenuated by specific optics, limited heating temperature and a short integration time. The infrared detector is operated under low light conditions where dark current noise mechanisms of detector and electronics like current and thermal noise are not negligible compared to the radiation-induced shot noise [10].

Since the intensity values of an IR image are used for the TDT analysis, the noise is described by the standard deviation of the temporal intensity variations σ_I of a single pixel. Each post-processing step of the TDT image analysis transforms the statistical noise which is described by the Gaussian error propagation. In the first step of the image post-processing, the ensemble average of the image sequences results in a single sequence with reduced noise:

$$(54) \quad \sigma_{\bar{I}} = \frac{1}{\sqrt{M}} \sigma_I.$$

The effect of step 2 on the statistical noise is negligible. However, systematic noise like fixed pattern noise due to non-uniformity of the pixel is strongly reduced by offset subtraction. Step 3 of image post-processing, the actual decline rate calculation, additionally reduces systematic noise since only relative temperature changes are analyzed. From the Gaussian error propagation of Eq. (51), the statistical noise in the resulting decline rates is given by

$$(55) \quad \sigma_{\Lambda} = \frac{\sigma_{\bar{I}}}{\Delta t} \sqrt{\left(\frac{1}{\overline{\Delta I_k}}\right)^2 + \left(\frac{1}{\overline{\Delta I_{k+K}}}\right)^2}.$$

Here, the standard deviation in the image $\overline{\Delta I_k}$ and $\overline{\Delta I_{k+K}}$ is assumed to be constant within the analysis time interval

$$(56) \quad \sigma_{\bar{I}}(k) = \sigma_{\bar{I}}(k + K) = \sigma_{\bar{I}}.$$

$\overline{\Delta I_k}$ and $\overline{\Delta I_{k+K}}$ are extracted within the quasi-stationary region where the temperature decreases exponentially. $\overline{\Delta I_{k+K}}$ can therefore be expressed as

$$(57) \quad \overline{\Delta I_{k+K}} = \overline{\Delta I_k} e^{-\Lambda \Delta t}.$$

Equation (55) implies that the error in the TDT image is reduced with increasing heating temperature which generally increases the intensity values $\overline{\Delta I_k}$ and $\overline{\Delta I_{k+K}}$. The length of the analysis time interval $\Delta t = K/f$ with f being the camera frequency, also affects the noise level directly through the denominator and implicitly since $\overline{\Delta I_{k+K}}$ decreases for longer Δt . An optimal length of the analysis interval can be found by minimizing σ_{Λ} in Eq. (55) with respect to Δt . With Eq. (57), minimization of Eq. (55) leads to

$$(58) \quad \frac{\partial}{\partial \Delta t} \left(\frac{\sigma_{\bar{I}}}{\Delta t} \sqrt{\left(\frac{1}{\overline{\Delta I_k} e^{-\Lambda \Delta t}} \right)^2 + \left(\frac{1}{\overline{\Delta I_k}} \right)^2} \right) = 0 \Rightarrow \Delta t_{\text{opt}} \approx \frac{1.1}{\Lambda}.$$

It is found that the noise in a TDT image is minimized if an interval with length Δt_{opt} is used for data extraction within the quasi-stationary regime. Δt_{opt} is described by a simple formula, which is only dependent on the temperature decline rate in the quasi-stationary regime. As an example, for the temperature decline simulated in Sec. 3.2, the optimal length of the analysis interval is about $\Delta t_{\text{opt}} \approx 1.1/(12 \text{ s}^{-1}) \approx 92 \text{ ms}$. With a camera frequency of $f = 100 \text{ Hz}$, this corresponds to about $K = 9$ images, which are used to calculate the average temperature declines with minimal noise. By inserting the expressions of Eq. (57) and Eq. (58) in Eq. (55), a simple formula is found which is used to estimate the resulting relative noise in a TDT image from the relative noise of the k^{th} IR image

$$(59) \quad \frac{\sigma_{\Lambda}}{\Lambda} \approx 2.9 \frac{\sigma_{\bar{I}}}{\overline{\Delta I_k}}.$$

This shows, that for an analysis region with optimal length, the relative noise level of the thermal image is amplified in the TDT image by a constant factor of 2.9. With the definition of the *NETD* in Eq. (34) and Eq. (35), the relative noise in a TDT image is correlated to the camera properties and the temperature ΔT_k at the k^{th} IR image

$$(60) \quad \frac{\sigma_{\Lambda}}{\Lambda} \approx 2.9 \frac{NETD_k}{\Delta T_k} \propto \frac{1}{\Delta T_k \sqrt{t_{\text{int}}}} \frac{(f\#)^2}{\int_{\lambda_1}^{\lambda_2} t_{\text{lens}} \varepsilon \frac{\partial M_{\lambda}}{\partial T_k} D_{\lambda}^* d\lambda}.$$

From this consideration, a list of rules for noise reduction in TDT measurements is extracted. Reduction of noise in TDT images is achieved by:

1. increasing the aperture of the camera lens (reducing the f-number of the camera lens $f\#$),
2. increasing the lens transmittance t_{lens} ,
3. increasing the sensor integration time t_{int} ,
4. increasing the specific detectivity D_λ^* , for example by using another sensor material,
5. increasing $\partial M_\lambda / \partial T_k$ by increasing the object temperature T_k ,
6. optimizing the wavelength range $[\lambda_1, \lambda_2]$ of the sensor according to the object temperature,
7. increasing the heating temperature ΔT_0 and therefore ΔT_k of the offset corrected image,
8. optimizing the length of the analysis interval Δt on the temperature decline as derived from Eq. (58),
9. using coating emissivities ε close to one,
10. averaging multiple measurements. The standard deviation of the mean value is reduced by $1/\sqrt{M}$ as found in Eq. (54).

The last rule is particularly relevant for rotating measurements, where a high number of measurements is used to compensate the noise which is induced by the short integration time and low light conditions. With Eq. (54), the needed number of measurements M to reduce the standard deviation of the mean value $\sigma_{\bar{I}}$ within a confidence interval of 68.3 % can be calculated. For arbitrary confidence intervals, the following equation is used:

$$(61) \quad M = \left(\frac{z_\gamma \sigma_I}{\sigma_{\bar{I}}} \right)^2,$$

where z_γ is the γ -quantile of the normal distribution. For a confidence interval of 68.3 %, $z_\gamma = z_{0.683} = 1$, for a confidence interval of 95 %, $z_{0.95} = 1.96$. If a specific standard deviation σ_Λ in the TDT image should be reached at a given standard deviation σ_I of the raw intensity image, the total number of measurements is found by inserting Eq. (59) in Eq. (61):

$$(62) \quad M = \left(2.9 \frac{z_\gamma \sigma_{I,\text{rel}}}{\sigma_{\Lambda,\text{rel}}} \right)^2,$$

where $\sigma_{I,\text{rel}} = \sigma_I / \sqrt{\Delta T_k}$ and $\sigma_{\Lambda,\text{rel}} = \sigma_\Lambda / \Lambda$. As an example, in a turbine measurement under low light conditions, the temporal intensity variation of a pixel corresponds to a standard deviation of $\sigma_{I,\text{rel}} = 10$. To reduce the noise in the TDT measurement below $\sigma_{\Lambda,\text{rel}} = 0.1$ within a confidence interval of 68.3 %, $M = 84,100$ measurements are necessary.

In a rotating measurement, M is mostly limited by the maximal available measurement time divided by the duration of a single measurement. Here, M can be increased by averaging multiple pixel, and by reducing the duration of a single measurement, which is mainly limited by the duration of the temperature decline and therefore material properties.

In conclusion, several systematic and random error sources in a TDT measurement were identified. Their relevance depends on the specific measurement task. If quantitative heat transfer coefficients are to be measured, systematic and random errors of single pixel values must be considered. If the position of boundary layer phenomena (e.g. transition or separation) is to be determined, spatial errors like reprojection error and motion blur are the most relevant. For both types of measurements, the random noise in the image must be efficiently reduced. Therefore, several measures were identified using Gaussian error propagation. In real applications, many of them are limited or fixed by physical or geometrical boundary conditions or would require an unrealizable amount of financial or temporal effort. However, particularly the object temperature, the integration time and the number of measurements can often be optimized to enhance image quality.

3.5 Description and test of the measurement components

In the above sections, theoretical and general practical aspects of the TDT method were introduced. In this section, the requirements on the measurement components will be summarized and the specific equipment used in the following experiments will be described. In addition, tests of relevant properties are performed to characterize the equipment.

3.5.1 Radiative heating

3.5.1.1 Energy source

TDT is primarily suitable for measurements in stationary systems and fast rotating devices. For both applications, the energy source must provide sufficient energy to be able to heat up the coating to temperatures between 5 – 40 K and must not disturb the boundary layer flow at the surface of the component by sudden changes in fluid density. Since the available time for the heating process is limited in rotating devices and short-duration measurements, pulsed heating is used in this work. In these applications, usually good data quality can only be achieved if multiple measurements are averaged, which requires a precise timing of the energy pulse.

A convenient choice to fulfill these requirements are radiative energy sources. They do not disturb the flow and offer a flexible measurement setup for a broad range of applications. Furthermore, high power devices like flash lamps and lasers can reach the necessary temperature difference within a short time. For stationary measurements in a free-jet facility, a xenon flash lamp (Broncolor Pulso G 3200) is used as an energy source. The flash lamp converts a maximum of 3200 J electrical energy into radiative energy. The pulse length at maximum energy is 7 ms and can be reduced to 2 ms with energies up to 1492 J. Flash lamps are convenient for stationary measurements as they are easy to set up and can heat up large areas. In a turbine application however, the pulse length must be below a few microseconds

to effectively heat up the moving component. Furthermore, the radiative energy of the energy source must be coupled into the turbine casing which requires a beam with low divergence.

For rotating applications and setups with limited optical access, a Nd:YAG laser (Ekspla NL317) is used. The laser has a specified wavelength of 1064 nm, 4 – 7 ns pulse length and 5 J pulse energy. Every pulse can be triggered individually with a repetition rate between 9 – 11 Hz. For turbine measurements, heating times up to several microseconds are still sufficiently short and even favorable since the peak intensity of too short laser pulses can harm the coating and lead to erroneous measurements. Unfortunately, modern high energy lasers with active q-switch control emit the entire energy in one short pulse with a length of a few nanoseconds. The high-power density sublimates parts of the coating at maximum energy.

3.5.1.2 Pulse Stretcher

In order to avoid irreversible effects on the coating system, the power density of the pulse must be reduced at constant pulse energy. Hence, the duration of the pulse must be increased. This is achieved by an optical system of beam splitters, laser line mirrors and light paths with different lengths as described by Khare and Shukla [96]. Figure 21 (left-hand side) shows an illustration of the pulse stretcher optics. The incident laser beam hits the first beam splitter and is divided into two partial beams. One half of the beam energy is transmitted and travels through loop 1 before it is again split in two halves by the same beam splitter. Now, one quarter of the original beam is transmitted through the beam splitter and follows the same path as the formerly reflected half of the incident beam – with a temporal delay. This process is repeated in a second loop with a different length.

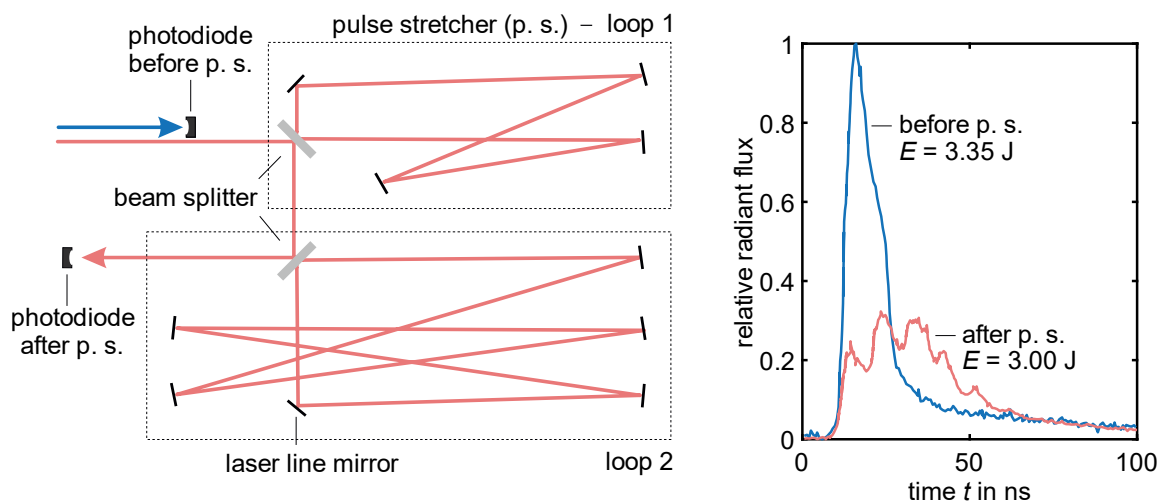


Figure 21 **Left** Illustration of the pulse stretcher (p. s.) optics. The incident laser beam is split into several partial beams by beam splitters. The partial beams are guided through loops with different lengths. **Right** Measurements of the temporal behavior of the radiant flux before and after the pulse stretcher using a photodiode sensor.

At the output of the pulse stretcher, the beam energy is distributed over a larger time interval and the peak intensity of the pulse is decreased by a factor of 3 so that destructive effects in the coating system are negligible. The temporal distribution of the beam energy before and after the pulse stretcher is shown on the right-hand side of Fig 21. The individual mirrors must be properly aligned so that all partial beams are superimposed at the output. Especially for beams which run through the loops several times, the correct alignment of the mirrors is very sensitive to small position changes, for example due to temperature drifts. Hence, absorption and scattering losses inside the pulse stretcher cannot be completely avoided, resulting in a reduction of the total energy of the beam by about 12 %.

3.5.1.3 Laser beam guidance

There are two common ways of delivering a laser beam to the required measuring position. The most convenient and easy one is to guide a laser beam by fiber optics. However, most of these fibers are made of solid materials such as silica or polymer and have a high-power limit. The laser power required for short-term heating in a TDT measurement exceeds the power limit of typical fiber optics by several orders of magnitude. In TDT measurements the beam is therefore directed to the desired position by high-energy laser line mirrors. However, adjusting these mirrors is often laborious, especially if the setup changes between measurements.

To avoid this effort, an articulated arm is used for some measuring tasks. An articulated arm is an optical system consisting of three hollow tubes which are connected by swivel joints. At the joints, the laser beam is redirected by high energy laser line mirrors. By rotation around the joints, the laser beam can be delivered to arbitrary positions without readjustment of the optics. The articulated arm used for this work, consists of two tubes with a length of around 2 m. The beam can thus be directed to positions within a radius of 4 m which offers a high degree of flexibility for a multitude of different measuring tasks. The laser beam inside the arm is encapsulated decreasing the laser safety class from 4 (highest) to 1 (lowest) if the light path before and after the arm is encapsulated as well.

3.5.1.4 Laser beam expansion probe

For two-dimensional heating, the collimated laser beam must be spatially expanded. Therefore, diffuser optics are used which are based on refraction or diffraction. The diffuser elements used in the experiments of this work consist of a glass substrate and a micro-structured surface made of polymer (RPC Photonics). The laser beam is refracted by the surface elements to form a rectangular or circular spatial pattern with high divergence angles. In general, arbitrary spatial forms can be achieved.

For the turbine application, the laser beam must be coupled into the rig casing via boreholes. Therefore, the beam diameter is initially reduced by a plano-convex lens from 17 mm to < 12 mm, to fit the borehole and is then strongly expanded by the diffuser optics at the end of the probe. The diffuser optics expands the beam into a rectangular shape with an opening angle of $44^\circ \times 36^\circ$. Due to reflection, such beam shaping elements can lead to beam energy losses. If the beam diameter is comparable to the

diameter of the diffuser element, the scattering of the edge rays of the beam can cause additional beam energy losses.

For an estimation of the total beam energy in a realistic application, the transmitted energy through the optical setup is thus measured after the diffuser optics. The energy of the rectangular core beam is shown on the right-hand side of Fig 21. As expected, the total pulse energy of 3.35 J differs from the manufacturer specification of about 5 J due to the described losses.

3.5.2 Coating system

For TDT measurements, a coating system is required on most components to optimize the thermal, aerodynamic, and emissive behavior of the surface. Particularly for metallic components with heat conductivities up to several hundred W/(m²K), the temperature rapidly recovers after an energy pulse so that time resolved measurements are almost impossible. Furthermore, high reflectances and hence low emissivities lead to poor signals on the IR sensor. On these components a surface coating offers a high emissivity in the wavelength range of the camera sensor, resistance against high laser power densities, high absorption at the laser specific wavelength and a low surface roughness. In addition, the layer system is used to design the temperature decline in such a way that quasi-stationary thermal conditions are present for a sufficiently long time for TDT analysis.

3.5.2.1 Coating materials

In this work, Nextel Velvet 811–21 coating and its optimized successor Nextel Suede 428–04 90FH coating (Mankiewicz) were used as high emissivity paints. The emissivity of the Nextel Velvet coating was measured by Lohrengel and Todtenhaupt with a normal emissivity $\varepsilon > 0.96$ in the wavelength range from 4 – 35 μm . Furthermore, they found a negligible temperature dependency of ε in the range of -60°C and 150°C and a negligible dependency on the emission angle up to 60° from the surface normal [11]. As an approximation, the coated surface can thus be regarded as a gray body $\varepsilon(\lambda, \delta, T) = \varepsilon$. This is especially true for TDT measurements since the dependency on the emissivity is eliminated during the relative analysis. However, low emissivities lead to higher noise in the resulting TDT image since the radiant flux and therefore the sensor signal is reduced.

Tests on the damage threshold of the Nextel coatings were conducted with the laser used in this work. It was observed that a laser energy of 3.0 J and a pulse length of 35 ns causes no material degradation for areas above 5 cm². This corresponds to a power density of the laser beam of about 17 MW/cm². For areas slightly smaller than 5 cm², inhomogeneities in the laser heating caused a gray coloring, whereas areas smaller than 2.5 cm² resulted in visible ablation of the Nextel coating.

According to the manufacturer, the further enhanced Nextel Suede coating features a reduced reflectivity in the SW wavelength range of about 0.3 % and an enhanced adhesive strength compared to the Nextel Velvet coating. It was thus used to increase the heating efficiency of the laser beam at a

wavelength of 1064 nm and to reduce the risk of delamination in the rotating application where high centrifugal and aerodynamic forces act on the coating. The surface roughness of both coatings was measured by an optical profilometer. The surface roughness parameter k_s was calculated according to [97] and yielded $k_s = 16.1 \mu\text{m}$ for Nextel Velvet and $k_s = 11.3 \mu\text{m}$ for Nextel Suede coating. An additional advantage of the Nextel Suede coating is therefore its reduced surface roughness.

To reduce conduction losses into the metallic base material, an insulation layer is placed under the high-emissivity coating. In this work, a polyamide foil was used as an insulation layer for geometries like flat plates or NACA profiles, and Parylene-C was used for more complex 3D-shaped components like turbine blades and vanes.

3.5.2.2 Thermal properties and impulse response

The thermal properties of both the high-emissivity paint and the insulation layer influence the thermal response on the energy pulse. The unsteady heat equation, Eq. (15), which describes the spatial and temporal temperature distribution inside the coating system contains the thermal conductivities λ_i , the layer thicknesses d_i and the volumetric heat capacities s_i of the used material layers. The index i denotes the individual coating layers: the high-emissivity paint $i = 1$ and the insulation layer $i = 2$. The aim of the following experiment was to study the effect of different coating thicknesses d_1 on the temperature decline behavior and analyze the properties of the coating system.

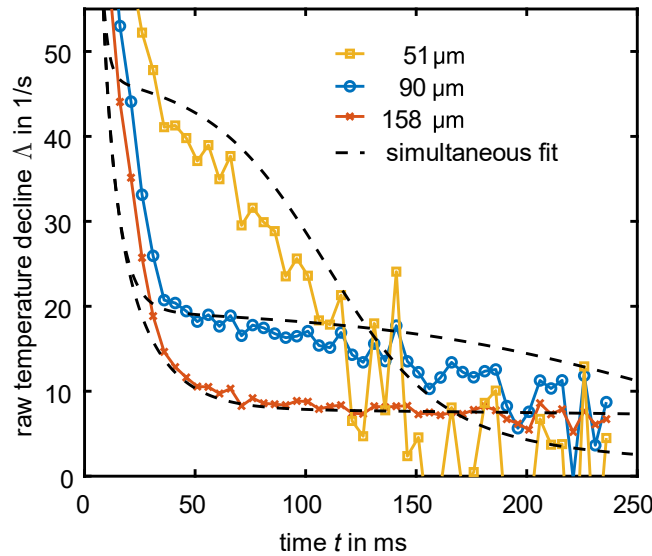


Figure 22 TDT measurement without flow for different coating layer thicknesses d_1 . The dashed lines show a simultaneous least-squares fit to demonstrate the usability of the 1D simulation for further analysis and to receive the volumetric heat capacity s_1 of the used coating.

Therefore, metal cylinders with a diameter of 30 mm and a height of 10 mm were coated with Parylene-C, $d_2 = 10 \pm 2 \mu\text{m}$ and a Nextel Velvet coating layer d_1 of 51 μm , 90 μm and 158 μm . The uncertainty of the d_1 measurement was $\Delta d_1 = 4 \mu\text{m}$.

Figure 22 shows the raw temperature decline rate Λ versus time for the different coating layer thicknesses. It is observed that the length of the quasi-stationary regime increases for increasing total thickness of the coating system, while Λ decreases. The simulation described in Sec. 3.2 was used to fit the measured data by least-squares minimization of all three curves simultaneously with fixed thickness distances. As fit parameters, the thickness d_1 , d_2 and the volumetric heat capacities s_1 were varied. For all other parameters literature values were found. All parameters are given in Tab. 1. From the fit in Fig. 22 two important conclusions are derived. First, the 1D simulation of the transient heat equation for several coating layers agrees with the measured data and can therefore be used for further analysis and estimations. Second, the unknown value for s_1 is determined and the fitted layer thicknesses agree well with the measured values.

Material parameter	Fitted value	Literature (L) or measured (M) value
thickness d_1 in μm (fixed distances according to measured values)	50.1, 89.1, 157.1	51, 90, 158 \pm 4 (M)
thickness d_2 in μm	10.2	10 \pm 2 (M)
volumetric heat capacities s_1 in $\text{MJ}/(\text{m}^3\text{K})$	1.9	—
volumetric heat capacities s_2 in $\text{MJ}/(\text{m}^3\text{K})$	—	0.92 (L, [98])
thermal conductivity λ_1 in $\text{W}/(\text{mK})$	—	0.20 (L, [11])
thermal conductivity λ_2 in $\text{W}/(\text{mK})$	—	0.082 (L, [98])

Table 1 Fitted, measured and literature values of thermal properties and thicknesses of Nextel Velvet coating (index 1) and Parylene-C (index 2)

3.5.2.3 Coating layer thickness

From the experimental data in Fig. 22 it was observed that the length of the quasi-stationary regime increases for increasing total thickness of the coating system, while Λ decreases. Further simulations of this effect are plotted on the left-hand side of Fig. 23 for different layer thicknesses. The dependency between the level and length of the quasi-stationary regime and the coating thickness is explained by heat loss through the insulating layer into the metal which is more pronounced for thin layers.

The relation between length of the quasi-stationary regime and Λ corresponds to the reciprocal relation between the optimal analysis length Δt and Λ found in Eq. (58). Hence, for smaller layer

thicknesses both the actual length of the quasi-stationary regime and the required length for an optimal TDT analysis are reduced to a similar extent. On the right-hand side of Fig. 23, both time intervals are simulated for varying Λ which were averaged within the optimal analysis interval. Independent of the coating thickness, the length of the quasi-stationary regime is always larger than the calculated optimal length of the analysis interval. This means that within a certain range, TDT measurements are independent of the total coating layer thickness. Limitations of this observation can be illustrated by considering the extreme cases.

For very thick coating layers, the duration of the temperature decline is long and the repetition rate for subsequent measurements is limited. As described in Sec. 3.4.6, particularly in turbine measurements where a high number of measurements is required and measurement time is limited, a long duration of the temperature decline has a negative effect on noise in the TDT image.

The other extreme case are very thin layers. Here the losses into the base material are substantial and the quasi-stationary regime is too short to be resolved by the IR imager, which has a limited image acquisition frequency. In a rotational application, the time between two subsequent images and therefore the minimal length of the quasi-stationary regime is determined by the rotation time of the rotating component. Figure 24 shows the minimal coating thickness at a given image acquisition frequency where exactly two images can be recorded during the quasi-stationary regime.

As an example, in the case of the turbine measurement conducted in this work, the rotation time of the measurement blade was about 17 ms and therefore the maximal possible image acquisition frequency was 59 Hz. Hence, a total coating thickness of 30 μm , leading to a quasi-stationary regime of about 9 ms length (see left-hand side of Fig. 23) is too thin to perform a TDT measurement.

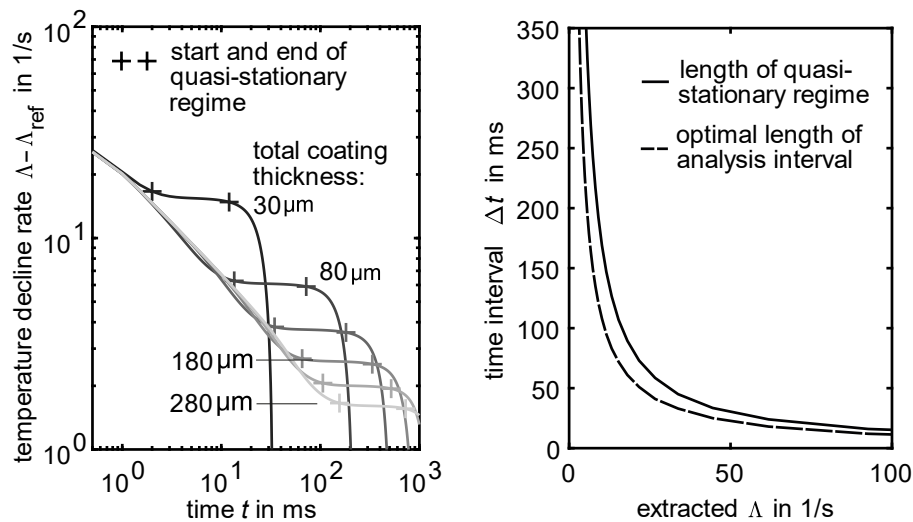


Figure 23 **Left** Double logarithmic plot of the temperature decline rate versus time for different coating layer thicknesses. The crosses show the estimated length of the quasi-stationary regime. **Right** Length of the quasi-stationary regime compared to the calculated length for data analysis Δt for optimal noise reduction as found in Eq. (58).

From Fig. 24, the minimal coating layer thickness is determined to about 40 μm . However, a more appropriate coating thickness is between 60 – 120 μm to resolve the temperature decline with more than two images and still maintain a fast temperature decline to enable a rate of > 3 measurements per second. In conclusion, TDT measurements require a coating system consisting of a high-emissivity paint with low surface roughness and an insulation layer. Experiments and simulations were conducted for Nextel Velvet coating on Parylene-C as insulation layer to show the suitability of this coating system for TDT measurements. Unknown material parameters were estimated, and an optimal range of coating layer thickness was found by using the 1D heat transfer simulation. For most applications, an appropriate coating layer thickness can be derived from the left-hand side of Fig. 23 and Fig. 24 if limiting time constants like image acquisition frequency or rotational speeds of the application are known.

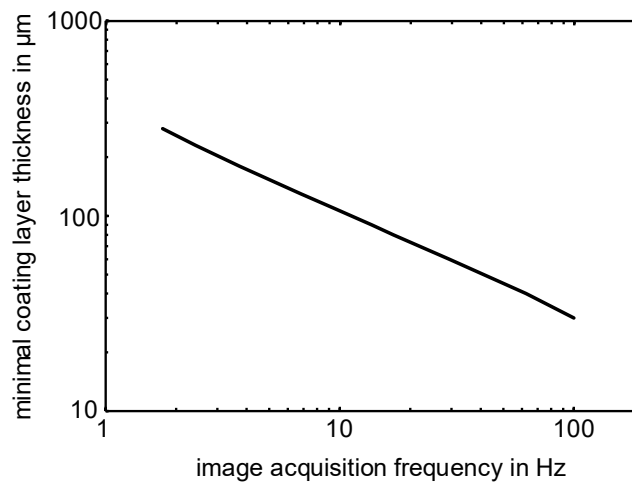


Figure 24 Minimal coating layer thickness for TDT analysis with a minimum of two images at a fixed image acquisition frequency

3.5.3 Infrared image acquisition

Measurements of the transient temperature decline are recorded by a high-speed IR camera. Two different camera systems were used in this work whose properties are listed in Tab. 2. The newer IR9300 has advanced sensor properties and a broader wavelength range and was used in most applications including the turbine measurement. TDT measurements were performed at temperatures up to 60 $^{\circ}\text{C}$. To provide a proof-of-concept for potential applications at higher temperatures, MW sensors were used which provide optimal temperature contrasts and temperature noise for temperatures between 40 – 400 $^{\circ}\text{C}$ as described in Sec. 2.4.2. The standard lens of both cameras has a focal length of 50 mm and a f-number of f/2.0. For turbine applications the standard lens is replaced by an IR borescope which was developed together with DIAS Infrared GmbH for this specific investigation. The borescope is in total 300 mm long to fit a wider range of turbine casing thickness, has a diameter of 19 mm, a focal length of 9 mm and a f-number of f/4.5.

Property	IR9300	CMT640
manufacturer	InfraTec GmbH	Thermosensorik
sensor	cooled InSb (indium antimonide)	cooled CMT (cadmium mercury telluride)
wavelength range in μm	2 – 5.7	3.4 – 5
resolution in pixel	1280×1024	640×512
pixel pitch in μm^2	15	15
max. image frequency for full-frame, half-frame, and quarter-frame in Hz	106,200,393	200,500, –

Table 2 Properties of the two high-speed IR-cameras used in this work

In order to quantify the noise characteristics of sensor and optics and to confirm Eq. (60), the relative image noise of the IR9300 camera system was analyzed in a set of experiments. For this, a temperature-stabilized blackbody source was set to a fixed temperature T_{BB} and the intensity signal I_1 was measured by the camera. 500 images were recorded with an image acquisition frequency of 200 Hz. The measurement was repeated at $T_{\text{BB}} + \Delta T$ to simulate a measurement after an energy pulse. From the second measurement I_2 , the standard-deviation of the temporal intensity noise σ_1 was calculated and averaged over several pixel. The relative image noise $\sigma_{\text{I,rel}}$ for the considered temperature range is then estimated by

$$(63) \quad \sigma_{\text{I,rel}} = \frac{\sigma_1}{\Delta I} = \frac{\sigma_1}{I_1 - I_2}.$$

The *NETD* of the camera system can then be calculated with Eq. (60) by multiplying $\sigma_{\text{I,rel}}$ with ΔT . Similarly, the expected relative noise in the TDT image can be estimated from Eq. (59).

Figure 25 shows the dependency of the relative image noise for different object temperatures, sensor integration times, number of averaged measurements, heating temperatures and lenses. According to the top left plot of Fig. 25, the relative noise is reduced for an increasing object temperature since the emitted radiant flux in the wavelength range of the MW sensor rises, which in turn increases $\partial M_{\text{BB}} / \partial T_{\text{BB}}$ (see Fig. 10 and Eq. (60)). A power law fit for the data of the standard lens yields

$$(64) \quad \sigma_{I,rel}(T_{BB}) = 4.36 T_{BB}^{-1.2},$$

with T_{BB} in $^{\circ}\text{C}$.

Furthermore, increasing the sensor integration time strongly reduces the noise. A fit of the data in the top right plot of Fig. 25 (standard lens) gives

$$(65) \quad \sigma_{I,rel}(t_{int}) = 0.22 t_{int}^{-0.75},$$

with t_{int} in μs . This approximately corresponds to the theoretical approach described in Eq. (59) which states a dependency of $\sigma_{I,rel}(t_{int}) \propto t_{int}^{-0.5}$.

Although the summed integration time of several measurements M yields the same radiation flux as an equivalent integration time of a single measurement, it is observed from the bottom left plot of Fig. 25 that the relative image noise is reduced more efficiently by a single measurement with comparable integration time.

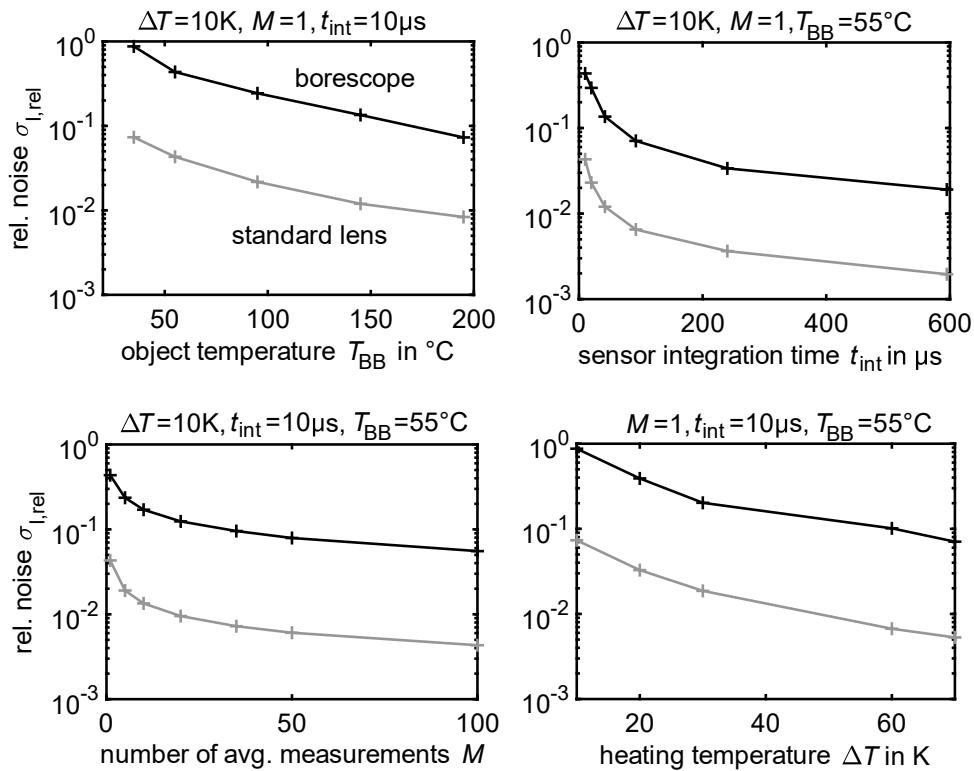


Figure 25 Logarithmic representation of the relative image noise of the IR camera system with standard lens (gray line) and borescope (black line) on changes in object temperature, sensor integration time, number of averaged measurements and heating temperature. The values of the fixed measurement properties are shown above every plot.

This is explained by the additional read-out and electronic noise of the sensor which accumulates for multiple measurements. However, the dependency of $\sigma_{I,rel}(M)$ shows that for a fixed integration time, like in a turbine application, the noise can be effectively reduced by averaging multiple measurements according to

$$(66) \quad \sigma_{I,rel}(M) = 0.04 M^{-0.50}.$$

The fit equation is matched by Eq. (54) which states a dependency of $\sigma_{I,rel}(M) \propto M^{-0.5}$.

The bottom right plot of Fig. 25 shows the dependency of the noise for different heating temperatures. As expected from the reciprocal relation in Eq. (59), the noise decreases for increasing heating temperatures with

$$(67) \quad \sigma_{I,rel}(\Delta T) = 1.8 \Delta T^{-1.37}.$$

All plots of Fig. 25 provide a comparison of the standard lens and the borescope. It is observed that the borescope performs about an order of magnitude worse. This is explained by the lower aperture of the borescope and therefore the reduced total radiant flux. According to Eq. (59), a decreasing aperture from $f/2.0$ to $f/4.5$ leads to an increase in noise by a factor of 5.1. In addition, the noise is amplified by the limited wavelength range of $3 - 5 \mu\text{m}$ of the borescope and its additional lenses which reduce the transmittance.

In conclusion, the experiments show that the noise level of a TDT measurement in a turbine environment increases by more than an order of magnitude due to the use of the IR borescope and about the same amount due to the small integration time of a few microseconds. This can be partially compensated by increasing the object and heating temperature and the number of averaged measurements.

3.5.4 Trigger control

Pulsed heating and IR image acquisition require precise triggering. In general, a measurement consists of N images and an energy pulse which is activated by a manual or automatic trigger event. In Fig. 26, the general trigger procedure is illustrated. The figure shows the triggering of the laser since it requires a more complex setup than the flash lamp.

After the trigger event, a temporal delay is added to the signal to control the number of images which are recorded before and after the energy pulse. The camera receives a trigger impulse for each image within the possible camera frequency range. The laser is triggered by two trigger signals. The first one enables the excitation of the lasing material by flash lamps. The second signal follows after 1 ms and starts the emission of the laser by activating the q-switch. Ideally, the emission trigger is

between two image triggers to avoid measurement errors in the IR image. The procedure is repeated M times.

The hardware used for triggering consists of a trigger control board and a delay generator (Ekspla SY4000) to generate a high-precision delay between the excitation and the emission trigger. Both devices provide a low jitter of < 500 ns and yield TTL trigger signals which are directly processed by camera and laser. In the case of a stationary measurement, the timing of the starting trigger is usually arbitrary. In contrast, for a turbine measurement, camera and laser are mounted at a fixed circumferential position of the turbine and must therefore be synchronized with the rotating measurement blade. Here, an accurate once per revolution signal (1/rev) from a turbine shaft encoder is used as starting trigger which is fed into the trigger control board. As illustrated in Fig. 27, the 1/rev signal is used as the temporal reference point for the calculation of camera and laser triggers. From there, the coated blade will be at the measurement position after a delay of d_{blade} . Shortly before the blade is at the measurement position, the camera is triggered to account for an internal delay d_{camera} between trigger input and the actual image acquisition (measured from trigger input to the middle of the integration time). An experiment with the camera IR9300 showed that $d_{\text{camera}} = 14 \mu\text{s} - t_{\text{int}}/2$.

While the camera is triggered every revolution, the laser heats up the blade only once per measurement (after N revolutions). The laser is excited exactly 1 ms before the blade arrives at the desired position and the laser emission is synchronized with the rotating blade. The triggering of camera and laser is subject to two boundary conditions.

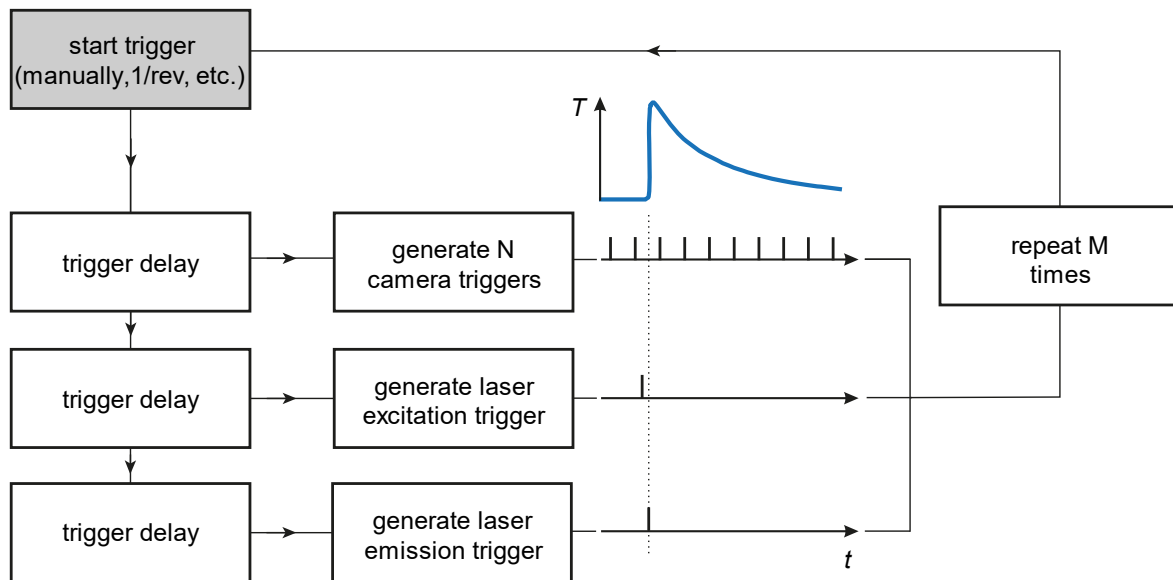


Figure 26 Procedure to generate trigger signals for camera and laser in TDT measurements

First, the repetition rate of the laser is fixed to 9 – 11 Hz. To avoid damage on the laser crystals by thermal effects, it must be excited within this frequency range, which is every 91 – 111 ms. However, laser emission is only required after several hundred milliseconds when the temperature of the blade has sufficiently decayed and a new measurement can be started. The laser beam of the excited laser must thus be blocked by omitting the emission trigger. The task of the trigger control board is to calculate the optimal excitation frequency within 9 – 11 Hz to enable a laser pulse for each measurement precisely when the blade is in the correct position. The second boundary condition concerns the trigger stability. If the signals are produced with a high jitter, the resulting images show random displacements in the blade position. Thus, averaging multiple measurements lead to a loss of spatial resolution and contrast. A correction of these displacements by image post-processing can be laborious or even impossible. In the turbine application of this work, the optimized jitter of the trigger control of < 500 ns lead to position displacements of $< 50 \mu\text{m}$ which is negligible compared to the spatial uncertainty in the rotor measurement.

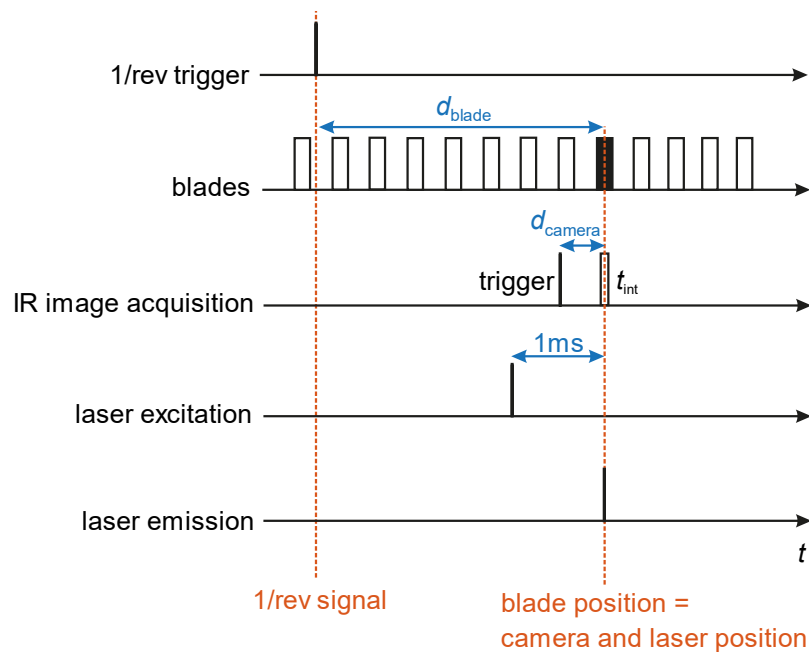


Figure 27 Trigger delays for a turbine measurement to synchronize camera and laser to the rotating measurement blade (filled black rectangle). The delays are calculated with respect to a once per revolution signal (1/rev).

Chapter 4

Quantitative heat transfer measurements

The following chapter is based on the work previously published in [A2] and [A4]. The author of this thesis would like to thank the co-authors for their valuable contributions. Especially relevant for this chapter are the contributions of Juergen Gruendmayer and Andreas Zeisberger for valuable discussions during the experimental design and the support during the setup and calibration of laser and pulse stretcher and of Christian J. Kähler to provide helpful discussions during the analysis and interpretation of the data and to enable the measurements at the free jet facility.

4.1 Aim of the measurement

In Sec. 3.3 a linear relation of temperature decline rates and heat transfer coefficients was derived theoretically. With this relation, quantitative heat transfer can be calculated from TDT data. In the following experiment, TDT data is converted into heat transfer coefficients by means of a calibration measurement. As a proof of concept, a TDT measurement is recorded in a laminar flat plate boundary layer and compared to the laminar Nusselt correlation. The resulting linear calibration relation is transferred to a different flow situation with a turbulent boundary layer. The results are compared to the turbulent Nusselt correlation to assess the validity of the calibration relation for different flow conditions.

In addition to the calibration measurement, a second experiment is presented. It addresses the non-uniform heating effect which is described in Sec. 2.2.3. This effect occurs in TDT applications where heat transfer is measured in hard-to-access geometries or over a large area. Since the laser energy is limited, to cover a larger measurement area, several smaller areas must be separately heated, analyzed, and stitched together in the post-processing. As the heated areas neither necessarily offer uniform temperature distribution nor start together with the developing velocity boundary layer, the unheated starting length results in inconsistent heat transfer coefficients and faulty stitching of different heating areas in the post-processing. The experiment investigates the application of a non-uniform heating correction for the TDT method on a flat plate in a free-stream. With this correction, the TDT method is

enhanced to consistently measure quantitative heat transfer distributions on extensive aerodynamic components and hard-to-access geometries with negligible pressure gradient.

4.2 Measurement setup

4.2.1 Setup for heat transfer calibration

The calibration measurements were performed on a 500 mm long flat plate at zero angle of attack in a free jet facility. The aluminum plate was laminated with a Kapton isolation foil with a low thermal conductivity of 0.12 W/(mK) [99] and coated with Nextel–Velvet–Coating 811–21. The leading edge of the plate has an asymmetrical profile which was derived from a numerical optimization which minimizes the pressure gradient around the leading edge [100]. The plate was positioned in the center of an exit nozzle of the free jet facility with 160 mm diameter at Mach numbers varying from $Ma = 0 - 0.15$. The Nd–YAG laser was used for this experiment. The laser beam was expanded by an engineered diffuser, resulting in a heated measurement area of about 50 mm \times 50 mm. The heating area provides a central part with homogeneous temperature distribution and an edge region with smoothly increasing temperature. In the central part of the heating area, a temperature rise of about 9 K was obtained. The IR9300 camera recorded the temperature decline with a frame rate of 200 Hz and 150 images per measurement.

The data reduction was performed following steps 1 – 3 described in Sec. 3.4.5. Since heat transfer coefficients do not change perpendicular to the flow direction, the resulting image was spatially averaged over 300 pixel to gain the mean profile section of $\Lambda - \Lambda_{\text{ref}}$ along the chord of the plate. This profile section was compared to heat transfer coefficients $\alpha(x)$ from the Nusselt correlation by calculating the corresponding x and Re_x for each pixel along the chord line and applying Eq. (28) and Eq. (29) to derive $\alpha(x)$.

This calibration relation was then applied to a turbulent boundary layer which was generated with an inclined flat plate of 4° angle of attack to generate a laminar separation bubble and a laminar–turbulent transition near the leading edge on the upper side of the plate. A TDT measurement was performed and the data were converted to heat transfer coefficients using the calibration relation found in the laminar measurement. For these experiments only weak temperature gradients in flow direction are present (< 0.1 K between neighboring pixel), such that two-dimensional conduction effects are negligible [101, 102].

4.2.2 Setup for non-uniform temperature correction

In order to investigate the effect of a non-uniformly heating area and unheated starting lengths, a similar setup was used with the above described flat plate. Another free-jet facility was used at

$Ma = 0.12$ and with a nozzle diameter of 55 mm in top-down configuration as shown in Fig. 28. By positioning the flat plate in an opening in the tabletop, undisturbed external flow conditions were achieved. The high-energy Nd-YAG laser was expanded by a diffuser optics resulting in a heated measurement area of about $80\text{ mm} \times 80\text{ mm}$ and a temperature rise of about 6 K. The laser beam was guided by high damage threshold mirrors mounted on a rail to easily move the heating area to different positions while the camera position was fixed. Seven different heating area positions were analyzed: position 1 with the uniform central part of the heating area starting at the leading edge of the flat plate at $x = 0$, and positions 2 – 7, where the non-uniform edge part of the heating area starts with a 10 mm offset in flow direction to the previous position. TDT measurements were performed with the IR9300 camera. Within the core jet of the flow, 180 pixel were averaged to reduce noise. The resulting temperature decline rates at position 1 were compared to the Nusselt correlation of a flat plate in laminar flow.

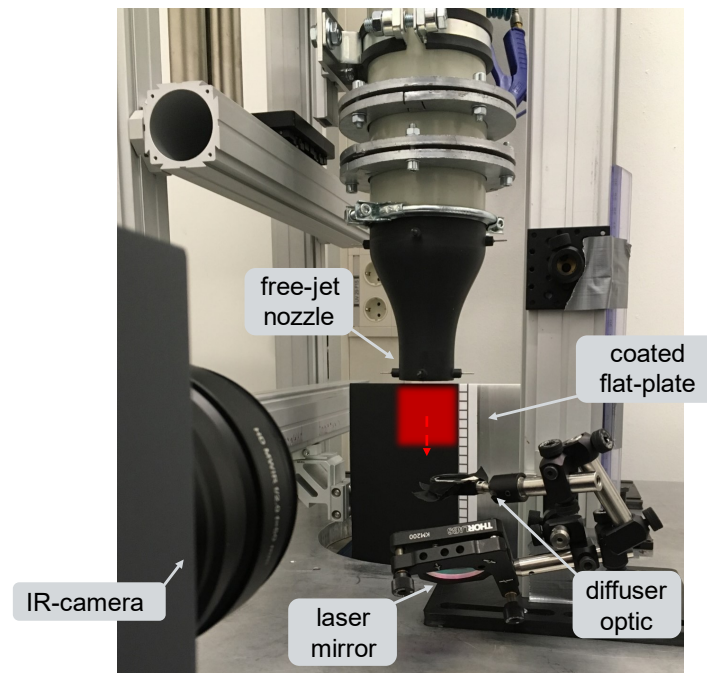


Figure 28 Measurement setup of a free-jet facility with coated flat plate, high damage threshold mirrors for laser beam guidance, diffuser optic for laser beam shaping, and IR-camera for temperature decline measurements. The (normally invisible) heating area was added to the photo for illustration. The image was modified from [A2].

4.3 Heat transfer calibration

4.3.1 Calibration in a laminar flow

For the calibration measurements, the free-jet was set to three different flow velocities, 17 m/s, 33 m/s and 51 m/s resulting in different Re_x ranges along the plate. A laminar boundary layer developed within the first centimeters of the flat plate. The measurement area started at the leading edge of the plate within the laminar region. For this measurement area and free-jet velocities, a local Reynold's number range of $Re_x \in [0.32 \times 10^3, 155 \times 10^3]$ was achieved for calibration. By using the local Nusselt correlation for laminar flow Eq. (28), heat transfer coefficients $\alpha(x)$ were calculated along the plate. By plotting $\alpha(x)$ against the measured TDT signal $\Lambda - \Lambda_{\text{ref}}$, a linear calibration relation can be observed as is shown in Fig. 29.

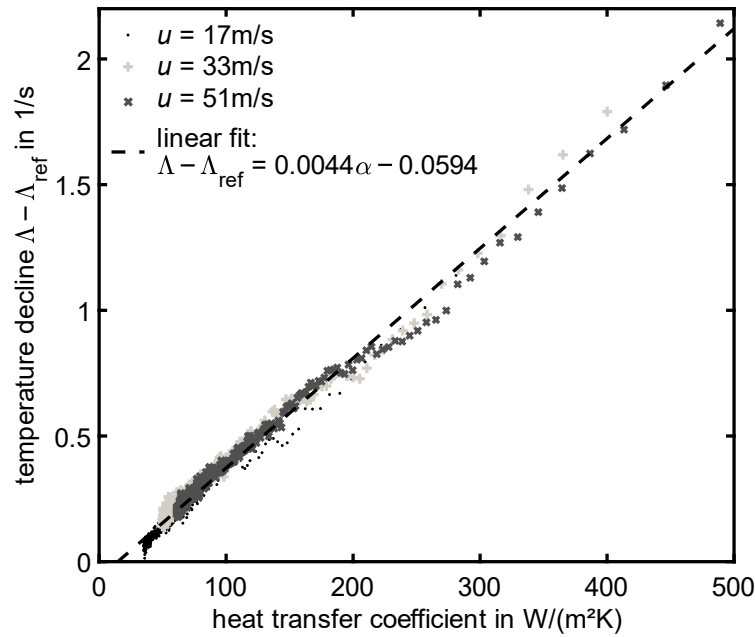


Figure 29 Linear calibration relation between data measured by Temperature Decline Thermography (TDT) and heat transfer coefficients calculated by the Nusselt correlation for different exit velocities u of the free-jet. A linear regression (dashed line) was fitted to the data of all free-jet velocities. The image was taken from [A4].

Datasets of three different free-jet velocities were fitted using a linear regression resulting in the calibration relation

$$(68) \quad \alpha = 227.3 \frac{\text{Ws}}{\text{m}^2\text{K}} (\Lambda - \Lambda_{\text{ref}}) + 13.5 \frac{\text{W}}{\text{m}^2\text{K}},$$

where the calibration constant is determined to $C' = 227.3 \pm 1.5 \text{ Ws}/(\text{m}^2\text{K})$.

The measurements indicate that the described theoretical model in Sec. 3.3 is applicable and that TDT data can be converted into heat transfer coefficients by applying the calibration relation within $\alpha = 50 - 500 \text{ W}/(\text{m}^2\text{K})$. This confirms the assumption, that within this range $f_{\text{cond}}(\alpha)$ in Eq. (46) can be approximated as linear in α . It thus affects only gradient and offset of the calibration relation. The offset of $13.5 \pm 0.8 \text{ Ws}/(\text{m}^2\text{K})$ at $\Lambda - \Lambda_{\text{ref}} = 0$ is composed of natural convection being present during the reference measurement without forced convection and conduction coefficients as described in Eq. (46). The errors given for the offset and calibration constant were derived from the fit. A detailed uncertainty estimation is given in Sec. 4.4.

4.3.2 Application of the calibration relation on turbulent flow conditions

Since the found calibration constants of Eq. (68) are independent of the flow condition, the calibration relation recorded in laminar flow also applies to other flow conditions. To show this, the calibration relation recorded under known laminar conditions is applied to other flow situations and geometries. Therefore, a turbulent boundary layer was generated on the plate.

In Fig. 30 a) and b), the local TDT data of the calibration measurement are shown as dark grey crosses along the chord line of the plate. This dataset corresponds to the data of Fig. 29 at $u = 33 \text{ m/s}$ and $u = 51 \text{ m/s}$ respectively which were converted to heat transfer coefficients using Eq. (68). For the sake of completeness, the laminar Nusselt correlation which was used for calibration is shown as well (black dotted line). The decreasing heat transfer with increasing boundary layer thickness and local Reynolds number is expected as the flow velocity gradient at the wall decreases with increasing boundary layer thickness.

The dataset of the inclined plate is shown in light grey circles. The data was converted to heat transfer coefficients using the same calibration relation Eq. (68). At $u = 51 \text{ m/s}$ (see Fig. 30b)), a characteristic change from low to high heat transfer coefficients is observed within the first six millimeters from the leading edge, corresponding to a laminar–turbulent transition. After the transition, a turbulent boundary layer develops which results in a gradual decrease of heat transfer coefficients. The laminar–turbulent transition takes place within the shear layer of a laminar separation bubble. Due to the lack of fluid movement within the laminar separation bubble [103], the heat transport is reduced resulting in lower heat transfer coefficients than in the laminar boundary layer.

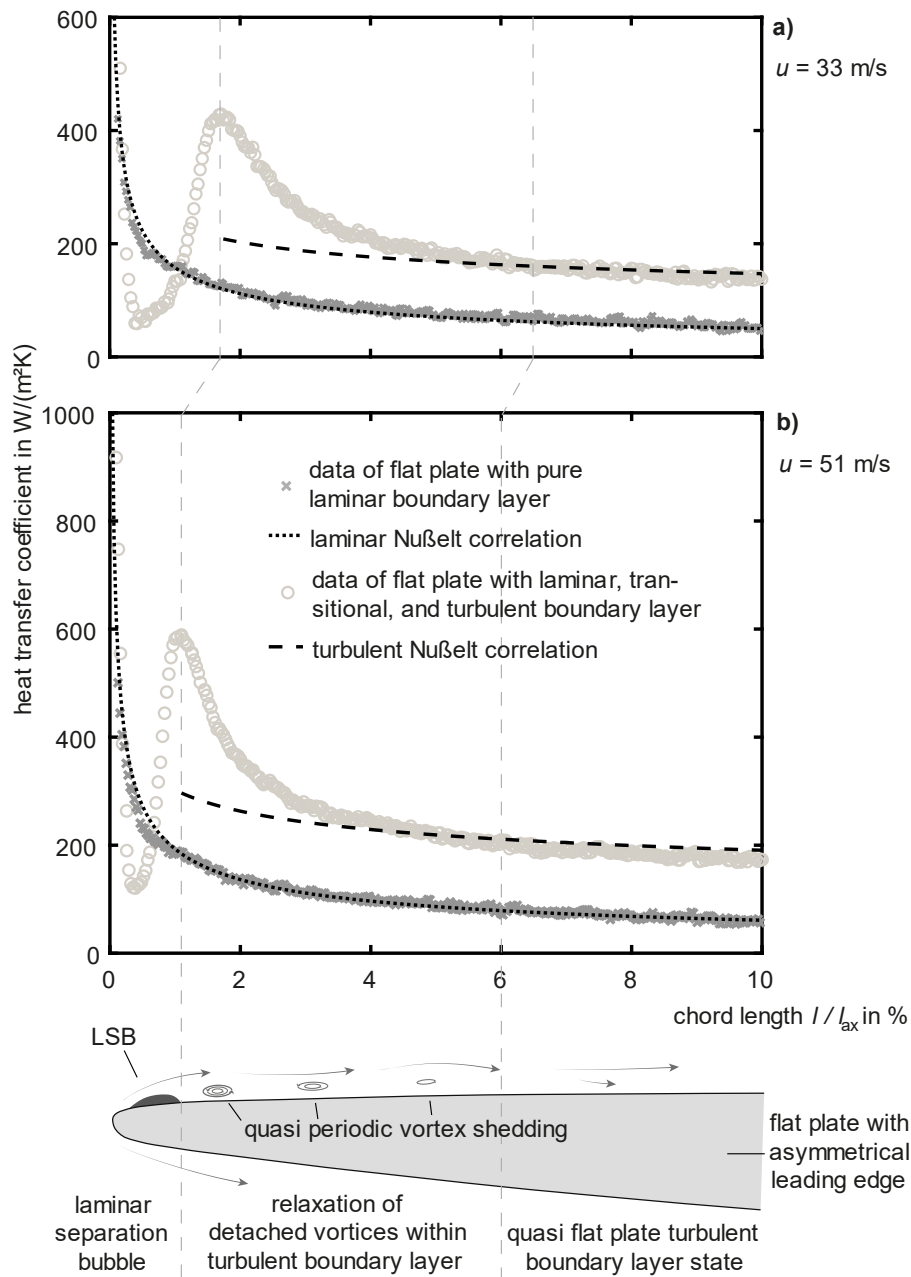


Figure 30 a) and b) show TDT data recorded in a laminar boundary layer as dark grey crosses which correspond to the data of $u = 33$ m/s and $u = 51$ m/s shown in Fig. 29. Additionally, data measured in a transitional and turbulent boundary layer on an inclined plate are shown as light grey circles. Both datasets were converted to heat transfer coefficients using the calibration relation Eq. (68). For comparison, the Nusselt correlation for laminar and turbulent flow are shown as dotted and dashed lines. The schematic below the plots shows the transitional and turbulent flow around the leading edge of the inclined plate. The laminar–turbulent transition, visible within the first millimeters of the plate, is triggered by a laminar separation bubble which is associated with quasi periodic vortex generation after reattachment of the flow. The vortices disperse gradually until a flat plate turbulent boundary layer state is observed. The image was taken from [A4].

The subsequent increase marks the end of the laminar separation bubble where the flow reattaches, and more heat is carried away due to the turbulent flow state after reattachment. The reattachment is a dynamic process. Small vortices develop at the end of the bubble which are detaching in an oscillating manner known as vortex shedding [104]. This process is sketched in the schematic of Fig. 30 c).

This results in higher mean heat transfer coefficients compared to the predictions of the turbulent Nusselt correlation for flat plates (black dashed line). The detached vortices gradually disperse in the turbulent flow and a flat plate similar boundary layer develops after about 30 mm. An asymptotic approach to the turbulent Nusselt correlation is observed within the last 30 mm of the measurement area. Within this range, it is shown that the calibration relation recorded in laminar flow can be validly applied to a measurement in turbulent flow with constant measurement parameters and different geometric setups.

4.4 Uncertainty estimation

The presented heat transfer calibration measurement is subject to systematical and random error sources of the TDT method as well as the error induced by the calibration method. In this study, the Nusselt correlation is used as calibration method. Since it is applied in non-ideal flow conditions, a deviation from the true heat transfer coefficient is expected which induces a systematic bias to the data. The use of the Nusselt correlation for calibration serves as a proof of concept, which demonstrates that in principle TDT data remains linear with changing heat transfer coefficients. By using a well-established measurement method for calibration instead, the error due to the calibration method can be reduced and specified.

The error sources of the TDT method were described in general in Sec. 3.4.6. Particularly relevant for this measurement is the induced random error, which is determined from the standard deviation of $M = 40$ individual measurements. According to Eq. (62), a random error of $\sigma_{\Lambda, \text{rel}} = 2.8\%$ is calculated for a confidence interval of 95 %. Systematic error sources like reprojection error and out-of-focus blur are negligible in this case since the camera angle was set to 0° and the target geometry was flat. The accuracy of the reference grid application is estimated to $\Delta x = 0.5 \text{ mm}$. As discussed in Sec. 3.4.6, the total spatial error is correlated to a systematic error in the measured heat transfer coefficient at a certain position x_0 , which is dependent on the local heat transfer gradient. According to Eq. (53), the spatial error in the transitional region of Fig. 30b) results in a maximum systematic heat transfer error of $\Delta \alpha = 0.5 \text{ mm} \cdot 258 \text{ W}/(\text{m}^2\text{K})/\text{mm} = 129 \text{ W}/(\text{m}^2\text{K})$. This shows that spatial error sources have a large effect on the uncertainty of the heat transfer measurement in regions with large heat transfer gradients. For the present calibration measurement on a flat plate with laminar boundary layer, the Nusselt correlation can be used to derive this error analytically. By calculating the derivative of the

Nusselt correlation of Eq. (28) and inserting it into Eq. (53), the error caused by a spatial uncertainty is given by

$$(69) \quad \frac{\Delta\alpha}{\alpha} = \frac{3}{2} \frac{\Delta x}{x},$$

which diverges for $x \rightarrow 0$. As an example, to not exceed a relative error in heat transfer coefficient of $\Delta\alpha/\alpha = 10\%$, calibration data must be extracted after $x = 1.5\%$ of the chord length. Here, the heat transfer gradient is sufficiently small, however, the calibration range is reduced. Hence, to cover a sufficiently large calibration range for a specific application, a large Ma number variation in the free-jet facility might be required.

It is emphasized, that the calibration relation in Eq. (68) can only be applied to other measurements if the same set of measurement and analysis parameters are used as for the calibration measurement. This contains the camera integration time, the used lens, the time interval on the temperature transient used for analysis, as well as type, and thickness of the coating. Changes in these parameters will lead to systematical errors when using the given calibration relation. Since only relative temperatures are measured, parameters like sample frequency and heating temperatures have a primarily negligible influence on calibration which is considered small compared to the random error of the method. However, for high heating temperatures the amount of heat emitted into the boundary layer is not negligible which may alter fluid density and viscosity of the flow. For the present measurements, a heating temperature of about 6.8 K was observed to have negligible influence on the calibration relation.

Different camera angles ($0^\circ - 70^\circ$ from the surface normal) and distances (0.5 – 1 m) with respect to the coated surface have been tested with negligible influence on the calibration relation. As expected, this allows the application of the calibration relation to data of different geometric arrangements.

4.5 Non-uniform temperature correction

In the following experiments, the heating area was gradually moved downstream to create an offset in temperature boundary layer development and to simulate experiments where stitching of multiple measurement areas is necessary or optical accessibility is limited.

The left-hand side of Fig. 31 exemplarily shows the thermogram of a shifted heating area of position 5 (50 mm offset to position 1 in flow direction) with temperature variations mapped in grayscales. High contrast areas with strong differences in emissivity and heat absorption are used as position marks in the infrared image. This enables determining the distance between leading edge and heating area and facilitates possible stitching of multiple measurement areas in the post-processing.

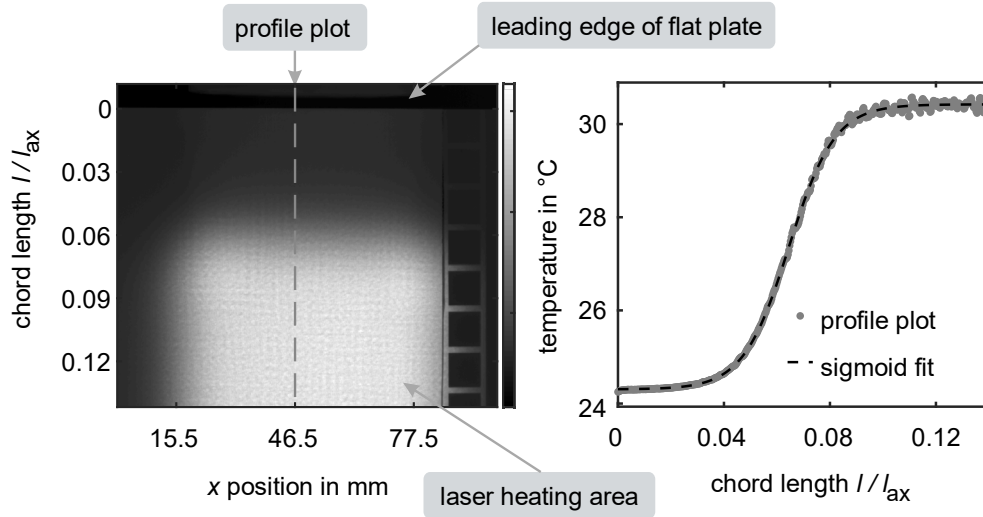


Figure 31 Left Thermogram of a flat plate in a free-jet facility for heating position 5. The laser heating area does not start at the leading edge, resulting in a non-uniform temperature distribution along the flat plate. A centimeter scale is shown on the right-hand side of the image. **Right** Averaged temperature profile plot along the dashed line of the left image. The data was parameterized by a least-squares fit of a sigmoid function. The image was modified from [A2].

On the right-hand side of Fig. 31, the related temperature profile plot along the flow direction is shown. For heating position 5, no heat was applied within the first 2% chord length. From 2 – 9% chord length, a steady increase of surface temperature is observed due to the refracting properties of the diffuser optics. The uniform central part of the heating area starts at 9% chord length and has a length of about 9% chord length (not shown in the plot). The temperature behavior can be fitted by least-squares minimization of a sigmoidal function

$$(70) \quad T(x) = T_{\infty} + \frac{b}{1 + e^{-a(x-c)}},$$

with the fit parameters $T_{\infty} = (24.30 \pm 0.01)^{\circ}\text{C}$, $a = 231.9 \pm 2.2$, $b = (6.12 \pm 0.01)^{\circ}\text{C}$, $c = 0.0323 \pm 0.01$. A sigmoid least-squares fit was performed for each position from 2 to 7. In position 1 a uniform heating was achieved by using only the central part of the heating area starting at the leading edge of the flat plate. The distance between the leading edge and the heating position is easy to determine in this case since it can be directly measured from the thermogram image.

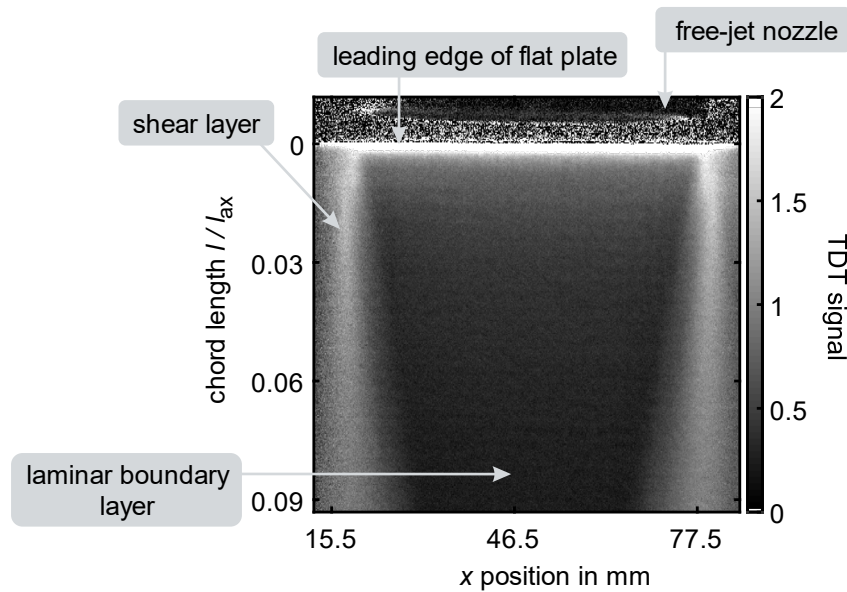


Figure 32 Temperature decline image of flat plate in a free-jet flow with $Ma = 0.12$. The uniform heating area starts at the leading edge of the flat plate. The image was modified from [A2].

However, due to limited optical accessibility or enlargement of the measurement area by stitching, this is not always possible. In such cases, the unheated starting length must be determined by measurements on the dissembled component, a computer aided model, and/or high contrast marks in the infrared image. A TDT measurement was performed for every heating position. Figure 32 shows the temperature decline rates of each pixel for heating position 1. Here, bright areas show high temperature decline rates which are proportional to high heat transfer coefficients. Dark areas stand for low heat transfer coefficients. The core jet of the free-jet facility with shear layers on both sides is clearly visible. A thin laminar boundary layer develops at the leading edge of the plate, resulting in high heat transfer coefficients which continuously decrease for downstream positions. Profile data of the measured temperature decline rates were extracted from the TDT images of position 1 to 7 in streamwise direction. The data are plotted in the top semi-logarithmic graph of Fig. 33. For better comparison to theory, the data of position 1 were multiplied by a constant factor to fit the Nusselt correlation of uniform heat flux in laminar flow. The same factor was then applied to the data of all other heating positions. A non-linear offset between the data of the shifted heating positions and position 1 is observed along the chord. This offset arises from differently developing thermal boundary layers of differently heated measurement areas. Temperature gradients are highest at the beginning of the heating areas, where cooler flow meets the heated wall and gets lower as the flow temperature within the thermal boundary layer rises.

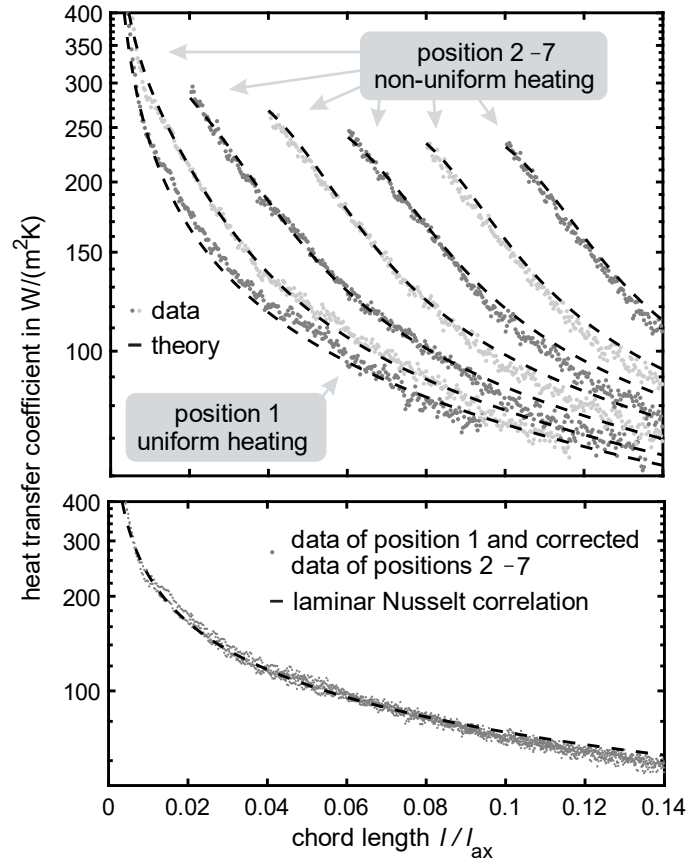


Figure 33 Top Semi-logarithmic representation of the temperature decline data of shifted heating areas along the flat plate (position 1 – 7). The data was multiplied by a factor to fit the Nusselt correlation for uniform heating and laminar flow. For positions 2 – 7, an integral boundary layer solution was found based on a sigmoidal temperature distribution. The theoretical solutions are shown as dashed lines. **Bottom** Corrections applied to heating positions 2 – 7 and plotted together with data of position 1. The laminar Nusselt correlation is plotted as dashed line. The image was modified from [A2].

The measured heat transfer coefficients were modelled by the integral boundary layer solution Eq.(31) using the fitted sigmoidal functions as local temperature distribution. Thereby, $\Delta T = T(x) - T_\infty$ is known and the local derivative $\partial T(\xi)/\partial \xi$ can be easily calculated. The summation consists of a single discontinuity term ($k = 1$) at the leading edge of the flat plate at $\xi_1 = 0$, where the sigmoid function has a non-zero value

$$(71) \quad \Delta T_1 = T(0) - T_\infty = \frac{b}{1 + e^{ac}}.$$

The integral is solved numerically. The parameter c in the sigmoid function characterizes the position of the heating.

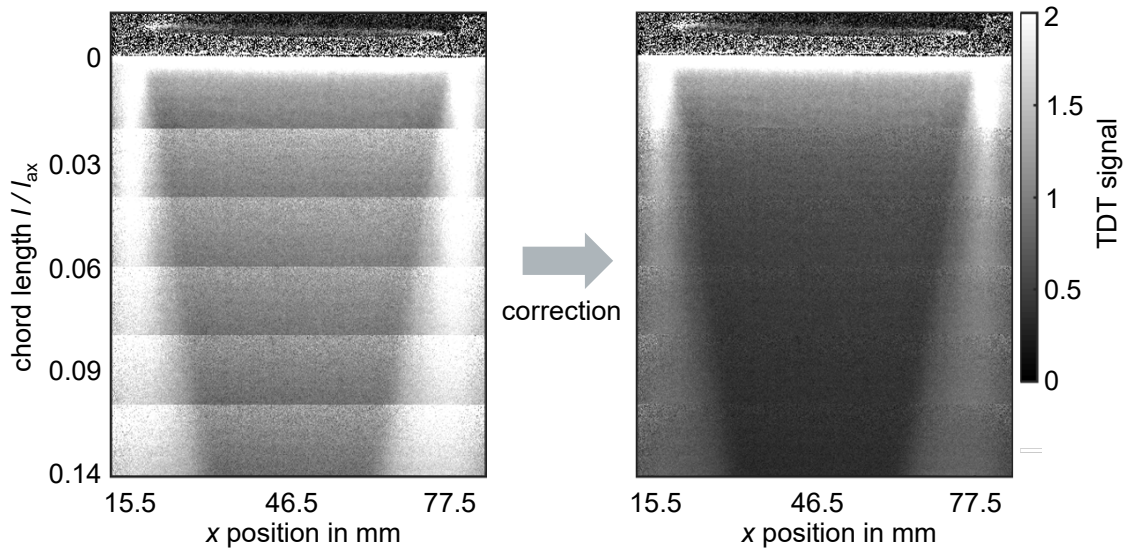


Figure 34 Stitched TDT images of the laminar flat plate boundary layer. **Left** Before applying the non-uniform heating correction. **Right** After the correction.

In Fig. 33 (top), the resulting modelled heat transfer coefficients are displayed as dashed lines. In general, theory and experiment are in very good agreement. For better comparison, the found corrections were applied to the data of position 2 – 7 and plotted together with the data of position 1 in the bottom graph of Fig. 33. For downstream positions starting from 9 % chord length, an increasing offset between data and theory is observed which is amplified by the semi-logarithmic representation. Since it is consistently found for all heating areas within the same chord length range, this effect can be considered as actual flow effect due to a non-ideal laminar flow, rather than a systematic error in the correction theory. Figure 34 shows the effect of the correction on the stitched TDT images. The correction works very well within the laminar core jet, but also significantly reduces the error in the shear layer of the flow.

4.6 Conclusion on quantitative heat transfer measurements with TDT

The quantitative analysis conducted in the calibration and the non-uniform heating experiment has the following important implications:

1. It was shown that data recorded by the TDT method can be correlated to heat transfer coefficients by a linear calibration relation. This confirms the developed theory of the temporal temperature decline and the numerical simulations based on the heat equation in Sec. 3.2 and 3.3.

2. The calibration relation recorded in laminar flow was used to convert data measured in turbulent flow into quantitative heat transfer coefficients. Good agreement to the corresponding Nusselt correlation was observed. Constraints to the application of the calibration to measurements in other flow conditions and geometries were given.
3. With a quantitative representation of TDT data, laminar and turbulent boundary layer conditions can be characterized. Furthermore, different flow states like laminar separation bubbles can as well be classified and analyzed.
4. The analysis of non-uniform heating areas showed that the effect of arbitrary heating distributions is an error source in quantitative TDT measurements and large area flow visualization. This effect is very well described by the integral boundary layer solution for unheated starting lengths of Sec. 2.2.3. A correction based on this solution was successfully applied to quantitative TDT data in non-pressure gradient flows.

The experiments in this chapter showed that quantitative heat transfer coefficients can be derived from a transient temperature measurement. Advantages of the TDT method are the fast, contactless, and two-dimensional measurement without complex electrical or mechanical heating (or cooling) of the component itself. No additional measurement techniques like thermocouples embedded in the component surface are needed. With a calibration, accurate knowledge of the thermo-physical constants of the surface materials is no longer required and the relative analysis of TDT reduces errors due to reflections and inhomogeneous coating emissivities. With the described correction, errors due to non-uniform heating are reduced and stitching of multiple measurement areas is enabled. This allows in particular the use of a laser as radiative heating source, where the heating is spatially confined and non-uniform, but highly reproducible and can be applied in geometries that are difficult to access.

To increase the accuracy of this technique, it would be reasonable to replace the Nusselt correlation as the calibration standard by a second measurement technique. The error of the calibration relation can then be defined more precisely. Furthermore, differences of coating thicknesses in calibration measurement and the desired application could be corrected by using simulations.

Chapter 5

Laminar–turbulent transition detection and validation

The following chapter is based on the work previously published in [A3]. The author of this thesis would like to thank the co-authors for their valuable contributions. Especially relevant for this chapter are the contributions of Juergen Gruendmayer, Andreas Zeisberger and Martin Stadlbauer to support the experimental design and setup; of Bastian Patzer to support the surface hot film measurements and of Christian J. Kähler to provide helpful discussions during the analysis and interpretation of the data.

5.1 Aim of the measurement

Before TDT is applied to complex geometries in a rotating turbine environment, its ability to detect laminar–turbulent transition and to measure qualitative heat transfer distributions is verified on a stationary NACA 0018 airfoil. TDT is compared to surface hot films, a well–established measurement technique for this task [105] and an alternative post–processing method for transition detection based on Gartenberg and Wright in which two thermograms before and during a heating process are subtracted [84].

In addition to the measurements of steady boundary layer transition, the usability of TDT for unsteady transition detection is assessed. Movement or oscillations in transition positions occur in many industrial applications and measurements are experimentally challenging [105]. TDT is compared to DIT, another method for unsteady transition analysis, which was introduced in Sec. 3.1.3. The aim of this section is to estimate the maximum temporal resolution of unsteady transition detection and to discuss implications for stationary and rotating systems.

5.2 Measurement setup

For the following experiments, surface hot films and the TDT method are simultaneously applied to a NACA 0018 airfoil exposed to the flow of a calibration free jet. A standard NACA 0018 profile with a cord length of 51 mm was used. It was manufactured from aluminum and equipped with 43 surface hot films which are mounted in 1.25 mm intervals along the suction side of the profile. Next to the surface hot films, two stripes of Nextel Velvet Coating 811–21 were applied as shown in the top photograph of Fig. 35. As surface hot films come with their own insulating Kapton layer, no additional thermal barrier was added underneath the paint. The airfoil was mounted in a free jet facility with 100 mm exit nozzle diameter as illustrated in the bottom schematic of Fig. 35.

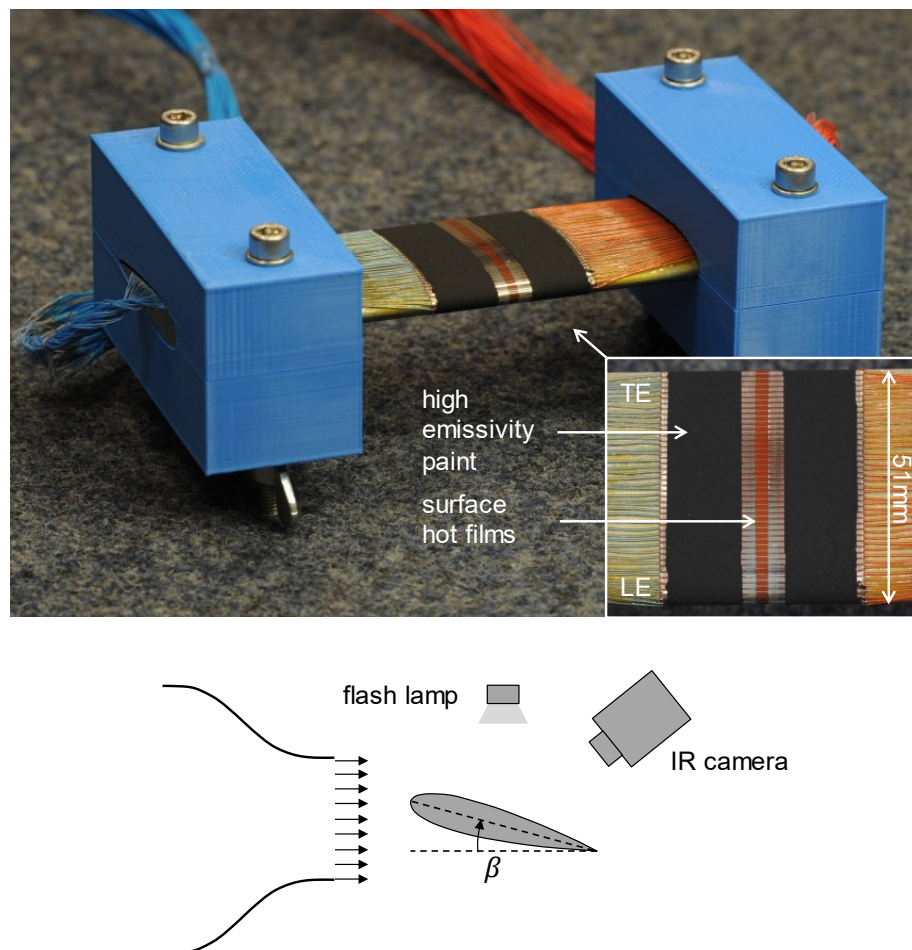


Figure 35 Top NACA–0018 profile equipped with surface hot films. The electric connections are coated with high emissivity paint for temperature decline measurements. Leading and trailing edge are marked by LE and TE. **Bottom** Schematic view of the NACA 0018 airfoil mounted in the free jet facility. β denotes the angle of attack.

To generate the energy pulse, a flash lamp (Broncolor, Pulso G) was used. Depending on the distance between lamp and sample, a temperature rise up to 40 K was achieved. The Thermosensorik CMT 640 M HS camera with standard lens was used to detect the temperature decline after the energy pulse. It was operated in half-frame mode for image acquisition with a sampling rate of 500 Hz and a sensor integration time of 592 μ s. The camera recorded 200 frames beginning immediately after the energy pulse.

Several different flow conditions were investigated with this setup by varying the Reynolds number (150×10^3 , 230×10^3), Mach number (0.15, 0.22) and angle of attack (0° , 8° , 15°). For each measurement, 20 sequences of 10 images were averaged. Furthermore, for each angle of attack, reference sequences were recorded with the same setup and geometry. TDT images were processed as described in Sec. 3.4.5 and profile plots were extracted from the perspective corrected images (after step 4 of the image-processing). Surface hot film and TDT measurements were carried out successively to avoid mutual interference. In addition, the individual hot film measurements were performed one after the other to prevent interference with the downstream sensors. In this way, equivalent flow conditions for TDT and surface hot films were ensured.

5.3 Transition detection on a NACA 0018 airfoil

A systematic study of laminar–turbulent transition with TDT on a NACA 0018 airfoil is described in von Hoesslin et al. [A3]. In these measurements, it was shown that transition positions are consistently detected with a high spatial resolution using the TDT method. By increasing the angle of attack of the airfoil, the transition position on the suction side shifted towards the leading edge as is expected for an increasing adverse pressure gradient. The same trend was observed by increasing the free flow velocity. This is explained by the fact that the critical local Reynolds number for boundary layer transition is reached earlier. To verify the ability of TDT to detect transition positions and measure qualitative heat transfer behaviors, TDT was compared to surface hot films.

Figure 36 shows the measured profile plots of both methods (top and center row) for different angles of attack along the chord line of the airfoil. The surface hot film signal was calculated from the raw data using Eq. (37). Since surface hot films record data with a temporal resolution of several kHz, the distribution of the temporal signal can be used to calculate standard deviation and skewness as described in Sec. 3.1.2. These parameters offer additional measures for the degree of turbulence within the boundary layer and can be used to determine the transition position with higher accuracy than the mean signal [62]. To determine the transition position with TDT, the center location between minimum and maximum of the transition region was used as indicated by the dashed and solid lines in Fig. 36. Like in the study mentioned before, the transition position (indicated by the solid line) is shifted towards the leading edge for higher angles of attack.

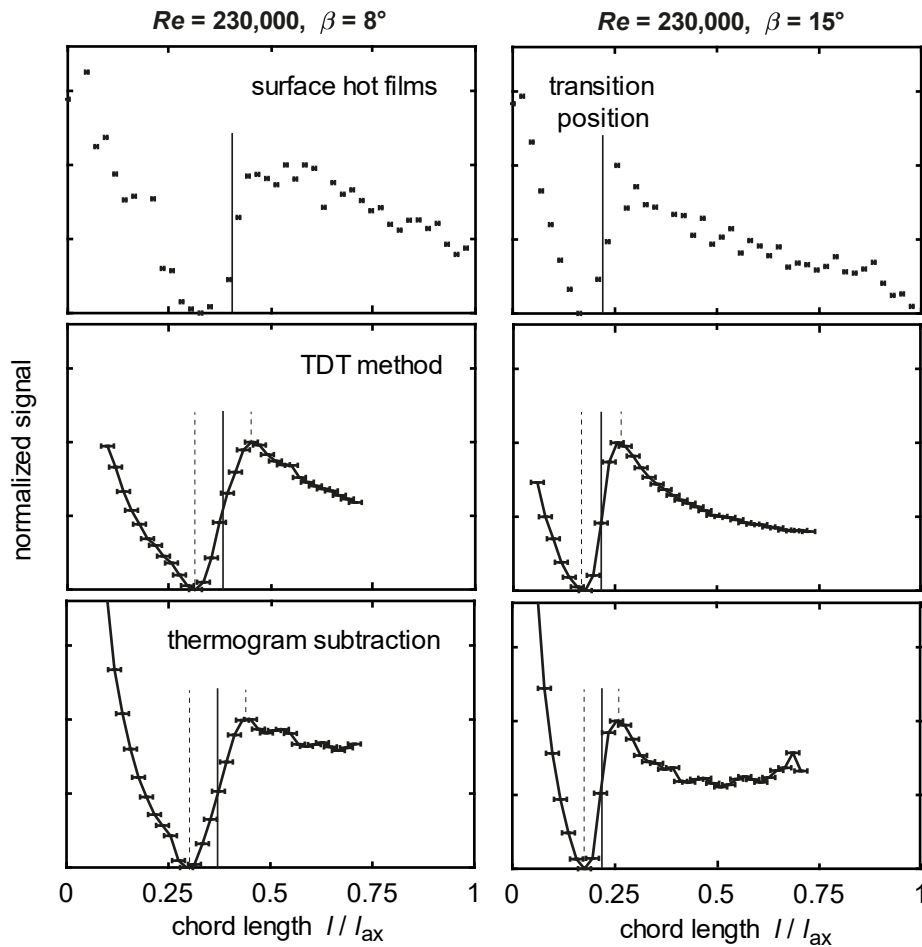


Figure 36 Comparison of surface hot films (top row), novel TDT method (center row) and the thermogram subtraction method of Gartenberg and Wright [84] (bottom row) at $Re = 230 \times 10^3$ for different angles of attack (8° and 15°) along the chord line of a NACA 0018 airfoil. All data were normalized and offset corrected to simplify comparison. The vertical solid lines mark the identified transition positions for each method. In the case of the surface hot films, the transition positions were determined with the skewness of the temporal signal distribution. For TDT and thermogram subtraction method the transition positions were determined by the midpoint between minimum and maximum in the transition region (marked by dashed lines).

TDT and surface hot films show consistent results regarding the transition position as well as the development of the heat transfer along the chord line. Good agreement between the two methods was also achieved for the other angles of attack and Reynolds numbers tested. The found transition positions of TDT and surface hot film measurements are summarized in Fig. 37 where the transition positions of both measurement methods are plotted against each other. The deviation from the ideal agreement (dashed line) of both measurement methods is within the measurement uncertainty of 2.7% of the chord

length for the TDT measurement and 1.4 % of the chord length for the surface hot film measurement. A detailed estimation of the spatial uncertainty is described in the subsequent Sec. 5.4.

In addition to surface hot films, Gartenberg and Wright's thermogram subtraction method was applied to the transient temperature data and compared to TDT. For this, two thermograms were recorded and subtracted. For the first thermogram I_1 a steady-state image before the energy pulse was used, while the second thermogram I_2 was recorded at the maximum temperature difference between the turbulent and laminar areas. The difference of the thermograms is calculated and the results are inverted and normalized for better comparison with the other methods. The bottom row of Fig. 36 shows the resulting profile plots. The analysis region of TDT and thermogram subtraction method was constrained by the curvature of the leading edge and the limited laminar region of the free-stream along the NACA profile. In Fig. 38, the two-dimensional spatial data of the TDT method and thermogram subtraction are shown. From the left-hand side of Fig. 38 turbulent wedges are observed at both sides of the coated area which narrow the laminar region in streamwise direction. This area, as well as the area near the leading edge was omitted for the determination of the averaged profile diagrams of Fig. 36. Hence, only data between 10 % and 74 % chord length are shown, which were averaged using 20 pixel rows left and right from the surface hot film area.

From Fig. 36 and Fig. 38 it is observed that both methods map the transition onto the same area. Since the high emissivity paint was applied on the metallic contacts of the hot films, the heat is partially dissipated by those rather than emitted into the flow. Consequently, different heat transfer conditions appear on the metallic contacts leading to a striped pattern perpendicular to the flow direction in the thermogram subtraction image (Fig. 38, right-hand side).

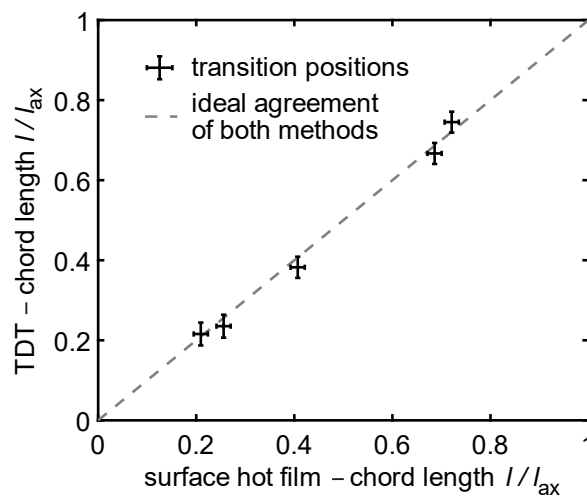


Figure 37 Comparison of the measured transition positions of TDT and surface hot films for all performed measurements. The data from left to right correspond to $(Re, \beta) = [(230 \times 10^3, 15^\circ), (150 \times 10^3, 15^\circ), (230 \times 10^3, 8^\circ), (230 \times 10^3, 0^\circ), (150 \times 10^3, 0^\circ)]$.

This bias effect is strongly reduced if the TDT method is used which takes advantage of the described post-processing and a reference measurement without flow (Fig. 38, left-hand side). In Fig. 36 a deviation of the thermogram subtraction method to surface hot film and TDT measurement can be identified near the leading edge of the profile and between 40 % and 74 % chord length. This deviation results from an inhomogeneous heating of the coated surface. The anisotropic illumination of the used flash lamp and the curved surface of the NACA-0018 profile lead to varying energy densities along the model surface. In this experiment, trailing and leading edge were thus less heated than the central part of the profile causing higher ΔI . In the case of the temperature decline method, this effect is considerably reduced by subtracting a reference measurement and applying the proposed analysis method.

It is noted that no temperature calibration of the infrared camera is needed since raw intensities correlate approximately linear with temperature values within the relevant temperature region. For the present experiments, no significant difference for using raw intensities or temperature values was observed. Furthermore, in the current experiments, the energy pulse caused a temperature rise of about $\Delta T = 40$ K. Generally, keeping ΔT as low as possible is desirable to not significantly alter the boundary layer by changes in fluid density and viscosity. However, due to the good agreement with surface hot film data, the effects on the transitional behavior at $\Delta T = 40$ K are assumed to be negligible.

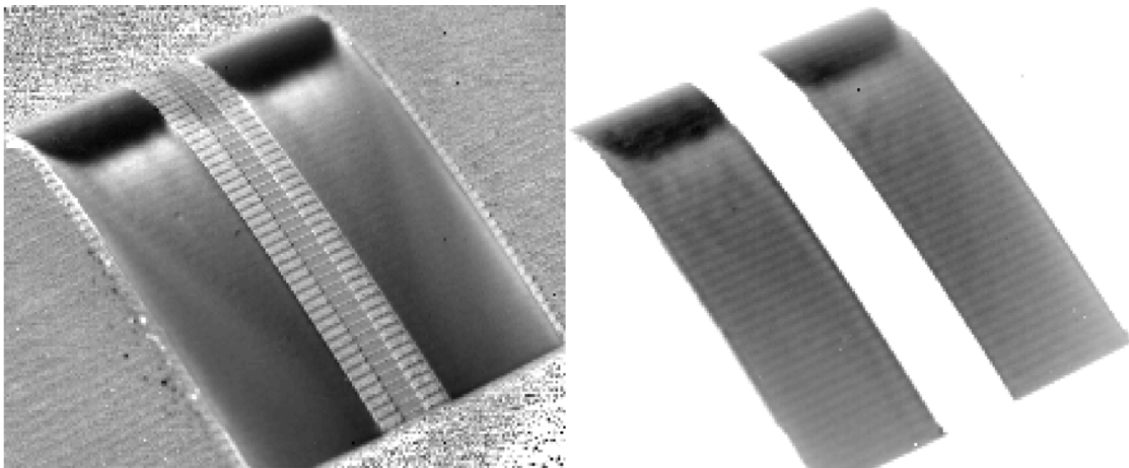


Figure 38 Post-processed images of a NACA0018 profile of the novel TDT method before perspective correction (**Left**), and after applying Gartenberg and Wright's method (**Right**). Exemplarily, the data of the measurement with a Reynolds number of $Re = 230 \times 10^3$ and an angle of attack of 15° were chosen. The image was taken from [A3].

5.4 Uncertainty estimation

Boundary layer transition detection with the TDT method is subject to several error sources. A general description of possible measurement errors can be found in Sec. 3.4.6. Particularly relevant for determining the position of a boundary layer transition with TDT is the induced spatial error. In the presented experiments, the transition position was determined by the midpoint between minimum and maximum heat transfer with an estimated error of 0.5 mm. Additional spatial errors are caused by the accuracy of the reference grid application which was estimated to 0.5 mm, the maximum circle of confusion in defocused areas on the NACA profile (< 0.1 mm), and the maximum reprojection error of dewarping the image in the post-processing (< 0.2 mm). The resulting total error of 2.7 % of the chord length is plotted in Fig. 37 together with the error of the surface hot films. The latter was estimated from the spatial resolution and application accuracy of the surface hot films to 0.7 mm which resulted in an error of about 1.4 % of the chord length.

From Fig. 36 it is observed that, compared to the TDT, the surface hot film data show large fluctuations between the individual sensors. The origin of these fluctuations remains unclear. Due to the long measurement time of 60 s, the random error has a negligible contribution to the measurement uncertainty. Hence random temporal effects cannot lead to the observed fluctuations. Moreover, the resistance of hot films and electrical connections were temperature calibrated before the measurement to correct systematical biases caused by temperature variations and different sensor resistances. However, it is assumed that the fluctuations originate from a systematic bias of the individual sensors. This may come from electrical interferences in the test facility which disturbed the measurement electronics of the hot films and caused a sensor specific bias.

5.5 Estimation for unsteady transition detection

In the experiments of the previous sections, components exposed to steady flow conditions have been investigated. In many aerodynamic systems unsteady flow and moving transition positions are observed. In gas turbines, for example, unsteady transition positions occur due to the repeated interaction of wakes of the vane row with the boundary layer of the rotating blade. The aim of the following section is to estimate the performance of TDT for unsteady transition detection in stationary as well as rotating environments.

In contrast to the previous NACA 0018 experiment in which 20 measurements were averaged to reduce noise, only a single measurement was evaluated for the unsteady analysis. Furthermore, temperature decline rates were calculated from only two subsequent images from the quasi-stationary

regime. With an image acquisition frequency of 500 Hz, the total measurement time was thus reduced from $t_{\text{tot}} = 265 \text{ ms}$ to $t_{\text{tot}} = 2 \text{ ms}$. Steady flow conditions are assumed during t_{tot} .

Figure 39 shows the result of this analysis. As is observed from the comparison between Fig. 38 and Fig. 39 (left–hand side images), the noise in the TDT image strongly increases. However, the signal change within the transitional region is still clearly visible. On the right–hand side of Fig. 39, a single row profile plot along the dashed line of the left–hand image is shown. To quantify the noise level, a *SNR* is calculated where the signal is defined as the difference between the minimum at the start of transition and the maximum at the end of transition.

The noise is calculated from the averaged standard deviation of the pixel–wise fluctuations perpendicular to the flow direction assuming that fixed pattern noise is eliminated in the TDT image and the pixel–wise fluctuation is only due to temporal noise. The *SNR* for the unsteady analysis with $t_{\text{tot}} = 2 \text{ ms}$ is determined to about 12. From an estimation using the data of Fig. 25 and Eq. (55), it is found that the total measurement time can be reduced to about $t_{\text{tot}} = 400 \mu\text{s}$ with a camera integration time of $t_{\text{int}} = 200 \mu\text{s}$ to still maintain a *SNR* of unity in the TDT image.

The maximum achievable temporal resolution of an unsteady TDT measurement is given by the minimum time between two subsequent measurements. If these were recorded during the same temperature decline, a superposition of thermal traces of the different transition positions impeded the detection of onset or end of transition like in the case of DIT [82]. This effect can be avoided if the second measurement is recorded after a second energy pulse and when the temperature of the first energy pulse has already recovered. In this case, the temporal resolution of an unsteady measurement is determined by the duration of the temperature decline. Simulations with the coating system used in this work show, that a minimum practically achievable layer thickness of $20 \mu\text{m}$ would lead to a duration of the temperature decline of about $t_d = 12 \text{ ms}$ at a heat transfer coefficient of $500 \text{ W}/(\text{m}^2\text{K})$.

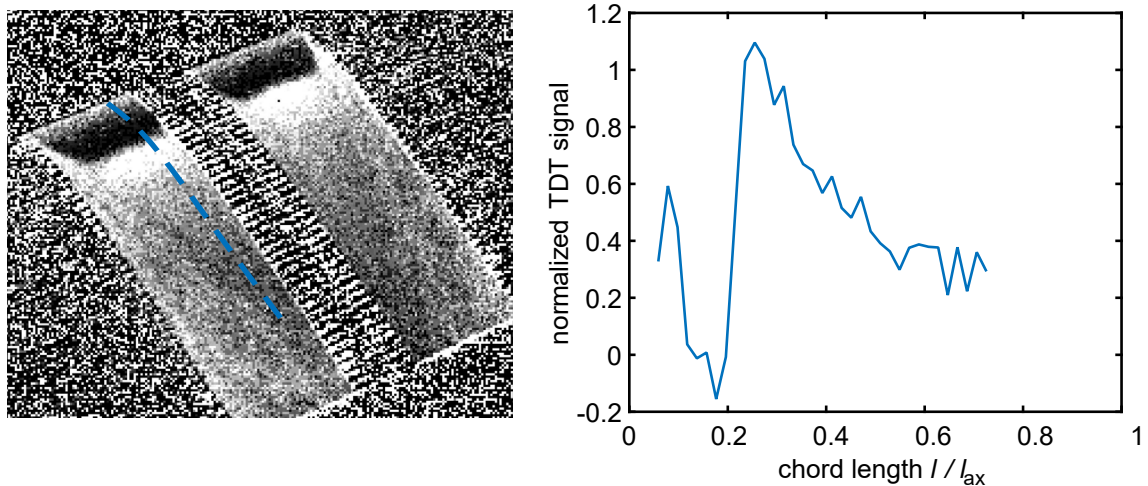


Figure 39 Left TDT image from a single short duration measurement at $Re = 230 \times 10^3$ and an angle of attack of 15° . Only two subsequent thermograms with a total measurement time of $t_{\text{tot}} = 2 \text{ ms}$ were used. Right Profile plot along the dashed line in the left–hand image.

The estimated achievable temporal resolution of an unsteady transition detection with TDT is therefore in the order of $f_{\max} = 1/t_d \approx 80$ Hz. It is noted that this is an order of magnitude estimation of the maximum frequency which is dependent on the thermal properties of the coating and the flow conditions. For the current TDT setup, f_{\max} is technically limited by the repetition rate of the energy source. As a comparison, DIT was tested for oscillating transition frequencies of 8 Hz and 14 Hz [82, 83]. Other authors performed unsteady IR thermography measurements at frequencies up to 10 Hz [106].

The estimation of the maximum temporal resolution shows that the detection of unsteady transition with TDT is possible in stationary systems. In fast rotating environments, additional constraints must be considered. In a turbine setup as described in Sec. 3.4.1, the minimum total measurement time is limited by the rotation frequency of the application since only one image can be recorded per revolution. Thus, $t_{\text{tot}} = 1/f_{\text{turb}}$. During one revolution, a blade passes several vane wakes such that the flow cannot be regarded as steady during t_{tot} and the transition oscillations cannot be resolved. Moreover, at high f_{turb} , smaller integration times than $t_{\text{int}} = 200 \mu\text{s}$ are necessary to avoid blurring in the images. If additionally the standard lens must be replaced by a special optics like the IR borescope due to the limited optical accessibility, the *SNR* in the TDT image drops far below unity according to Fig. 25. An unsteady transition in a turbine environment is thus not detectable with the current TDT method. However, for more open geometries and lower rotational velocities like in the helicopter rotor application of Raffel et al. [83], unsteady transition detection with TDT is expected to be feasible. The advantage of TDT is that no thermal history effects must be corrected as is the case for DIT. TDT uses pulsed heating and the evaluation of two or more thermograms on a fast temperature transient. The time between the two thermograms is significantly shorter and onset and end of transition can be detected from a single measurement. This simplifies the data analysis and allows for a faster and a more robust evaluation of unsteady transitions.

5.6 Conclusion on transition detection with TDT

From the experiments in this chapter, the following conclusions are derived for the detection of laminar–turbulent boundary layer transitions with TDT:

1. It was shown that a transient temperature analysis can be used to detect and visualize laminar, transitional, and turbulent flow regions on a NACA 0018 airfoil with a high spatial resolution. Reynolds and Mach numbers up to $Re = 230 \times 10^3$ and $Ma = 0.22$ were tested.
2. Compared to surface hot films, transition positions and the development of the heat transfer along the profile showed excellent agreement for several different angles of attacks and

Reynolds numbers. The TDT method provides two–dimensional information and vastly reduces the amount of instrumentation since no wiring and sensor calibration is necessary.

3. Compared to other post–processing techniques for IR–based approaches, it combines short heating and measuring times with strongly reduced interfering effects making it suitable for transition detection in complex and fast rotating systems.
4. Although transient transition effects do not seem to be resolvable in fast rotating environments, an estimation showed that in systems that allow the use of long sensor integration times $> 200\text{ }\mu\text{s}$ and camera lenses with large aperture ($> f/2.0$), the detection of an unsteady transition is possible with TDT. The estimated maximum temporal resolution is in the order of 80 Hz with the coating used in this study.

TDT provides fast and accurate detection of steady boundary layer transition. For the detection of flow effects in fast rotating turbine applications, TDT is well suited if information of the averaged flow effect is required. Currently, such measurements are of great importance for the design of modern aircraft engines and will be addressed in the following chapter.

Chapter 6

Flow visualization in a turbine rig

The following chapter is based on the work previously published in [A1]. The author of this thesis would like to thank the co-authors for their valuable contributions. Especially relevant for this chapter are the contributions of Juergen Gruendmayer, Andreas Zeisberger and Martin S. Sommer to provide valuable discussions concerning the design of the experiments, to support measurement and calibration of laser, pulse stretcher and trigger control; of Christian J. Kähler to provide helpful discussions on the experimental design, the analysis and interpretation of the data; of Jonathan Klimesch to support the implementation of the Matlab tools used for image analysis; of Stephan Behre to conduct the CFD simulations; of Henri Brandies to ensure the safe operation of the axial turbine rig.

6.1 Aim of the measurement

In this chapter, the TDT method is applied to a 1.5 stage axial turbine rig at the Institute of Jet Propulsion and Turbomachinery of the RWTH Aachen. The aim of this measurement is to provide a proof of concept for the use of the TDT method to visualize surface boundary layer flows in a realistic turbine environment.

First, the setup is described for the measurement on a stationary vane and a rotating blade. The blade measurement demonstrates the applicability of the IR borescope and beam delivery optics under real rig conditions. Near-wall flow phenomena like transition, flow separation and vortex systems are observed and the influence of surface roughness on the boundary layer is discussed. After this, experiments on the rotating blade are presented which are compared to CFD simulations. This measurement confirms the usability of TDT in a high-speed application under low-light conditions and with a limited optical accessibility. For the first time, a two-dimensional visualization of boundary layer transition on a rotating turbine blade was achieved in this experiment.

6.2 Measurement setup

TDT measurements were conducted in a 1.5 staged configuration which consists of a rotor surrounded by two vane rows. The design Reynolds number of the first vane is $Re = 8.1 \times 10^5$ which is defined by the outflow conditions of the vane and the cord length. The turbulence intensity at the turbine inlet is in the range of 0.4 – 0.7% and the turbulent length scale between 7.9 – 11 mm according to [107, 108]. The development of turbulence intensity and length scale after the first vane row is described in [109]. Further description of the test rig has been presented in previous papers [107, 110].

A photograph of the measurement setup at the turbine rig with high-power laser, beam guidance, infrared camera and borescope is shown in Fig. 40. The laser generates a laser pulse whose power is reduced by the pulse stretcher system mounted on top of the laser head. It is guided through the articulated arm and the beam expansion probe into the turbine rig. Right after the laser pulse, the blade is heated up by about 5 K. The following temperature decline is measured by the infrared camera with IR-borescope. Like the beam expansion probe, the borescope is inserted through the rig casing via a borehole and the camera is mounted on the casing to minimize mechanical stress on the optical components due to oscillations of the running turbine. The configuration of the probes inside the rig is illustrated in Fig. 13.

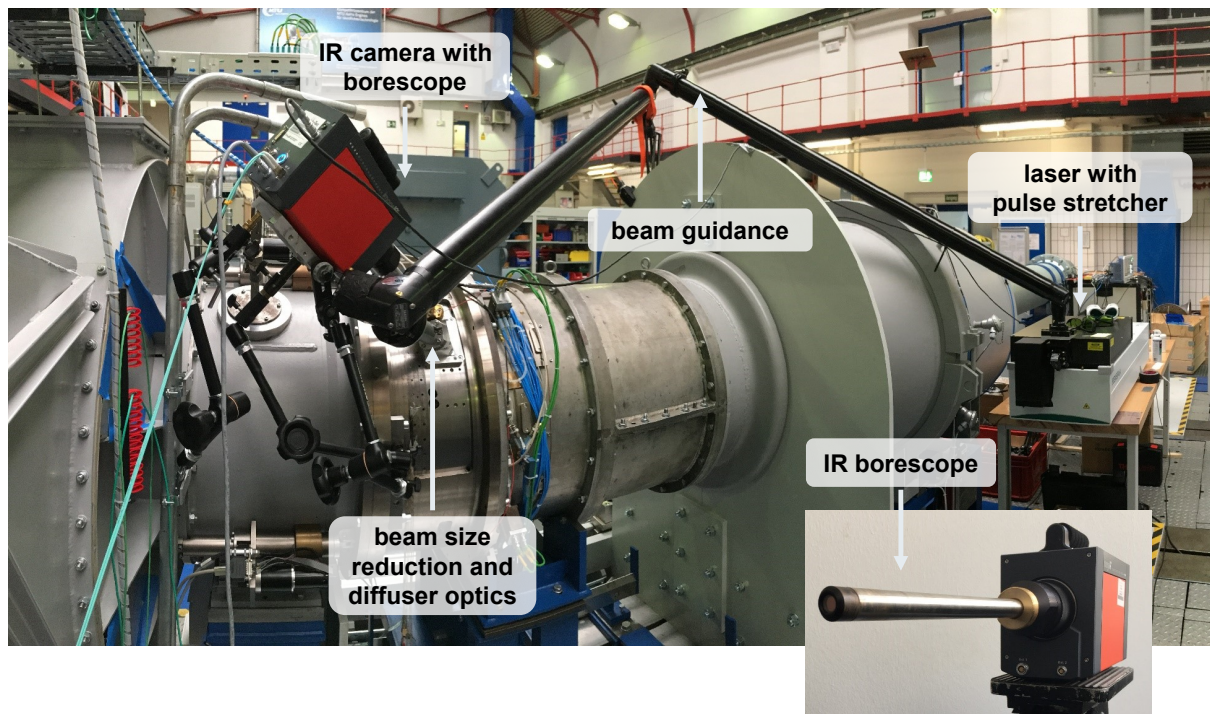


Figure 40 Experimental setup of the TDT components at the axial flow turbine rig of the Institute of Jet Propulsion and Turbomachinery, RWTH Aachen. The photograph in the bottom right corner shows the used infrared borescope in more detail. The image was taken from [A1].

The surface coating consists of Nextel Suede 428–04 90FH and Parylene–C with a total layer thickness of 100 μm . It was applied to several blades and vanes for redundancy. In addition, two blades and one vane were covered with the position reference coating as shown in Fig. 15. In the vane measurement, images were recorded with a fixed frequency of 150 Hz. The exposure time of the imaging sensor was set to 1286 μs . One measurement consisted of ten offset images before, and 70 images after the energy pulse. In total, 100 measurements were ensemble averaged to reduce statistical noise. A backward facing step was milled into the vane to force a laminar–turbulent transition. It is typically used to generate known boundary layer conditions for the CFD simulations of the downstream rotor row. In this experiment, the resulting flow separation and transition to turbulence were used as a reference to confirm the applicability of TDT. Furthermore, a cylindrical wire piece with about 1 mm in diameter and height was glued to the vane surface to cause a turbulent wake in the boundary layer and provided an additional consistency control for feature interpretation.

In the rotor measurement, images were recorded once per revolution with a frequency of 58 Hz. Two offset images were recorded before the laser heating followed by five images during the temperature transient. The sensor exposure time was reduced to 10 μs to reduce local blurring due to the fast–moving blade. This is accompanied by a significant reduction in the *SNR* of the recorded images, which was partly offset by averaging 3000 measurements. This is a trade–off between a high *SNR* and a convenient measurement time which was about 40 minutes.

The results of the rotor measurement are compared to computational fluid dynamics (CFD) simulations. A detailed description of the numerical model and the parameter used for this analysis can be found in [A1]. Since the temperature decline is analyzed over several revolutions, the resulting data are interpreted as the integral effect of the unsteady flow within one revolution. This includes the 33 vane wakes which lead to an oscillating transition position and instationary vortex flows. Hence, the unsteady CFD simulations were time averaged to model the experimental situation.

6.3 Flow visualization on stationary vanes

6.3.1 Vane measurement with a backward facing step

The left–hand side of Fig. 41 shows the TDT measurement area of the suction side mapped on the 3–D vane model where the backward facing step and the glued wire piece are marked by arrows. The right–hand side graph shows the intensity profile (radially averaged over 20 pixel rows) along the dashed line of the left–hand side. Upstream the backward facing step, a laminar boundary layer develops. Due to the increasing thickness of the thermal boundary layer along the flow direction, the heat transfer coefficient decreases until a steep drop marks the edge of the backward facing step.

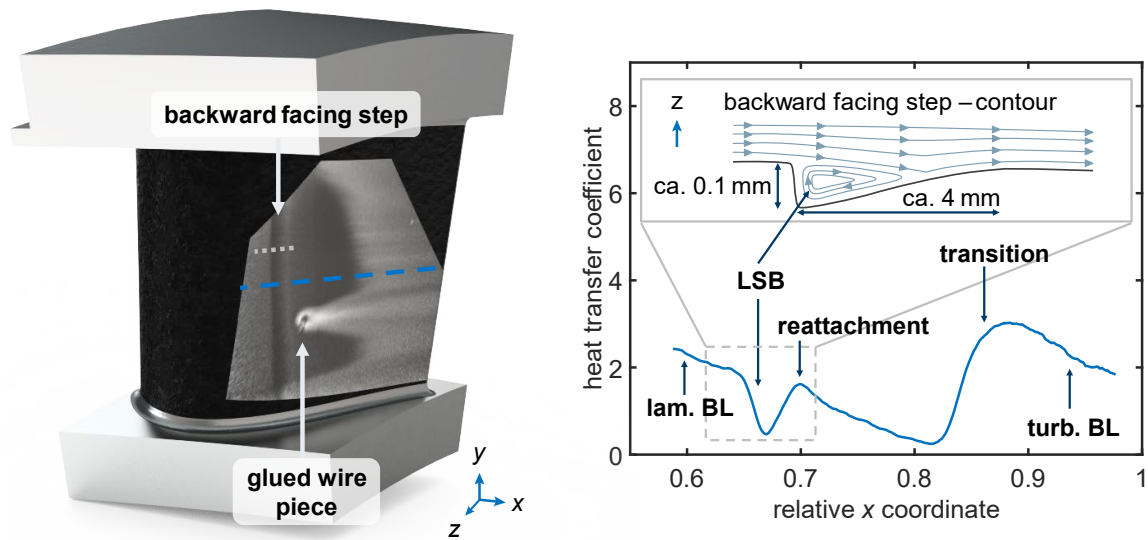


Figure 41 TDT measurement on the suction side of a guide vane at a Reynolds number of $Re = 2.8 \times 10^5$. **Left** 2-D flow visualization mapped on a model of the vane. **Right** profile plot of the measured heat transfer coefficient along the dashed line on the left-hand side. Leading and trailing edge of the vane correspond to x -axis values of 0 and 1. The inset shows a schematic of the flow around the enlarged backward facing step contour along the dotted line on the left-hand side. The image was modified from [A1].

The schematic in the inset of the right-hand side of Fig. 41 shows a schematic of the contour of the backward facing step after which a laminar separation bubble (LSB) occurs [111, 112]. Within the LSB, the heat from the wall cannot be dissipated effectively and the heat transfer coefficient is significantly reduced which was also observed in the previous flat-plate experiments and by other authors [46]. Following the dashed line further downstream, the laminar boundary layer reattaches after about 2 mm which leads to an increase in the heat transfer coefficient. A maximum in heat transfer is reached that slightly exceeds the heat transfer coefficient of the undisturbed laminar boundary layer. According to Vogel and Eaton [113], this maximum occurs near the reattachment region. They describe a rapid recovery of the heat transfer to undisturbed boundary conditions downstream the maximum. Although they investigated turbulent flows, this effect is as well observed in the laminar flow of the current measurement. At the relative x position of about 82 %, the heat transfer is minimal followed by a transition to a turbulent boundary layer. As expected, the heat transfer coefficient strongly increases within the transition region and decreases after the transition due to an increasing turbulent boundary layer thickness.

Apart from the strong turbulent wake of the glued wire piece and the transition, the near-wall footprints of the endwall flow vortices are clearly visible confining the 2-D flow region in the center of the vane. The measurement shows that a high SNR and a spatial resolution of up to 13 sample points

per millimeter can be achieved. The analysis of temperature changes instead of absolute temperatures, the subtraction of an offset image from the temperature transient and the subtraction of a reference measurement without air flow effectively correct for spurious effects like inhomogeneous coating emissivities and surface heating, reflections from surrounding components and non-uniform heat loss due to a varying blade thickness.

6.3.2 Influence of surface roughness on transition

With higher Reynolds numbers, the thickness of the boundary layer decreases, and isolated surface roughness elements begin to cause disturbances and distort the flow. Figure 42 shows the result of the vane measurement at different Reynolds numbers ranging from $Re = 2.8 \times 10^5$ to 7.6×10^5 . The flow visualization of Fig. 41 is shown again in the upper left image for better comparison. For Reynolds numbers greater than $Re = 4.6 \times 10^5$, turbulent wedges are observed within the laminar flow region which impose high heat transfer on the wall. The wedges appear randomly in a certain distance range from the leading edge and move upstream as the Reynolds number increases.

The backward facing step has a clear influence on the onset of these wedges. At $Re = 5.9 \times 10^5$, the transition is induced directly at the backward facing step while upstream individual turbulent wedges occur. At $Re = 7.6 \times 10^5$ the boundary layer upstream the backward facing step is almost completely turbulent. The surface roughness of the Nextel Suede 428–04 90FH coating was estimated to $k_s = 11.3 \mu\text{m}$ in Sec. 3.5.2.1. The critical surface roughness $k_{s,\text{crit}}$, above which an influence on the boundary layer is expected can be estimated from Eq. (32) and is shown for every Reynolds number in Fig. 42. It is observed that for $Re = 2.8 \times 10^5$, no influence of the surface roughness is expected ($k_s < k_{s,\text{crit}}$) while for all other cases, disturbance of the boundary layer is possible ($k_s > k_{s,\text{crit}}$). The occurrence of turbulent wedges for $Re > 4.6 \times 10^5$ confirms this estimation.

It is therefore concluded that in turbine flows with a comparably low free-stream turbulence of about 0.7% and a vane Reynolds numbers greater than about $Re > 4 \times 10^5$, the influence of the present surface coating on the boundary layer is not negligible. For these cases it is confirmed that Eq. (32) provides a valid measure to determine the optimal coating prior to a specific application. As described in Sec. 2.1.1.2, a high coating roughness usually increases the emissivity of the coating. Hence, a trade-off must be found between a smooth surface with low flow disturbance and a high data quality due to high emissivities.

After the measurements it was found that the Nextel Suede 428–04 90FH coating had changed to a brownish color within the measuring range. This could be due to microscopic oil particles in the fluid that were deposited on the coating and burned by the high-energy laser beam. It is expected that the emissivity of the coating was gradually reduced during the measurements. As described in Sec. 3.4.6, this increases the image noise, but has a negligible effect on the mean value of one pixel.

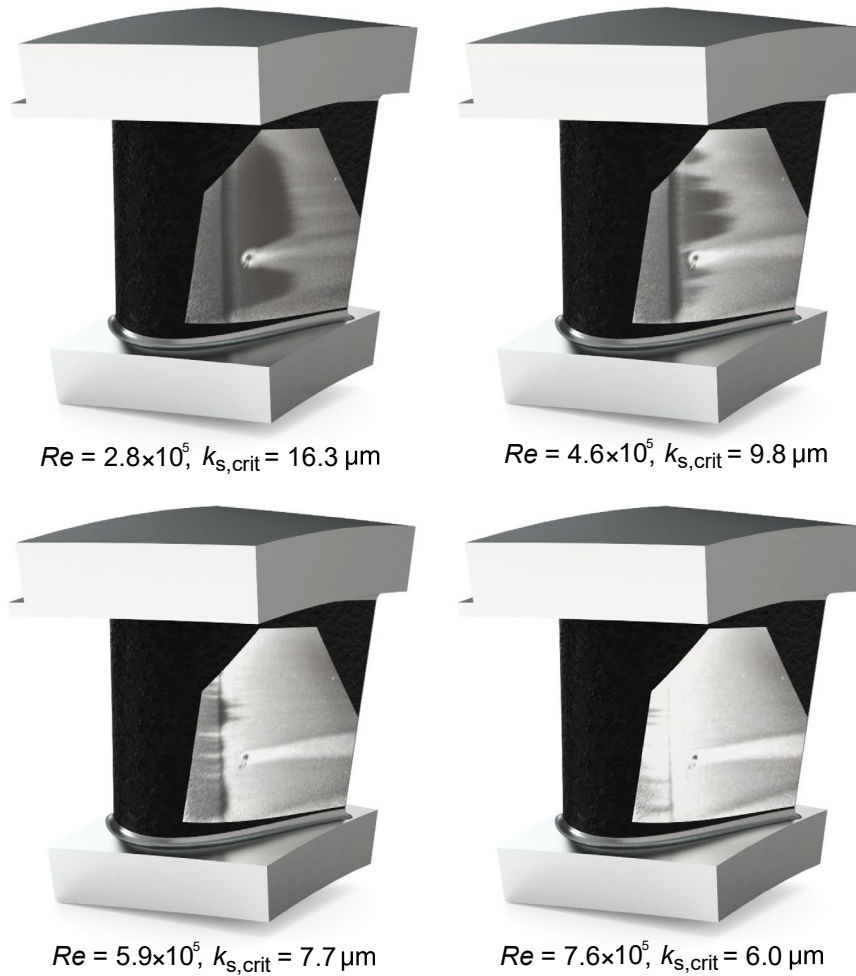


Figure 42 TDT measurements at four different Reynolds numbers. Turbulent structures due to surface roughness elements are visible for Reynolds numbers greater than $Re = 4.6 \times 10^5$.

6.4 Flow visualization on rotating blades

In the following, a proof of concept for the visualization of a laminar–turbulent transition on a rotating blade in a gas turbine rig is presented. Since this is the first experiment ever of a flow visualization on the suction side of a rotating gas turbine blade, the present study is limited by the lack of available ground truth data to verify the measured boundary layer phenomena. Hence, CFD simulations are used to provide estimates for the accuracy of transition detection as described in Sec. 6.2. Figure 43 shows the TDT measurement and the CFD simulations of intermittency and wall shear stress.

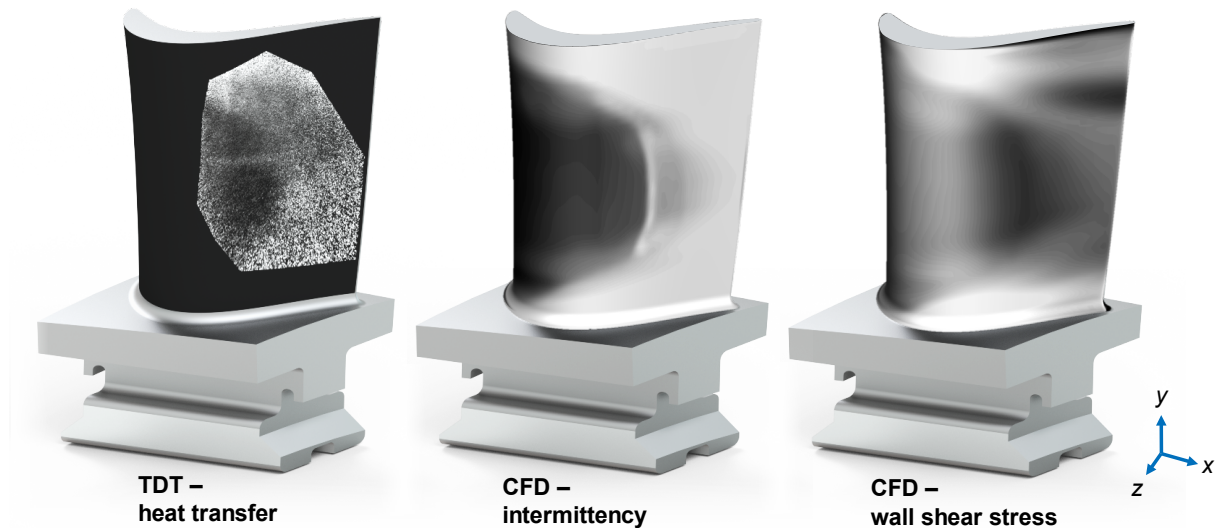


Figure 43 Qualitative comparison of near-wall boundary layer conditions in TDT measurement and CFD simulation at $Re > 7.6 \times 10^5$. The image was modified from [A1]. The author would like to thank Stephan Behre for conducting the CFD simulation and providing the resulting data.

Due to the short exposure time of the sensor of $10 \mu s$, the noise level of the TDT measurement is significantly higher than in the vane measurement. However, after averaging 3000 measurements, the transition area is clearly visible by the abrupt change from low to high heat transfer. As in the vane measurement, the laminar 2-D flow area is confined by the secondary vortex flows from the top and bottom. Near the center of the channel height, a turbulent wake of a surface roughness element is visible as a bright narrow wedge as observed in the vane measurements.

Figure 44 shows the corresponding intensity profiles of the data of Fig. 43. The profile plots were radially averaged in the 2-D flow regime (within 30 – 45 % of the blade height, 80 pixel rows) to further reduce noise. The measurement starts at an x position of around 60 % and ends near the trailing edge of the blade. The intermittency simulation predicts a mostly laminar boundary layer up to about $x = 80 \%$ and a subsequent transition to a turbulent boundary layer, which is well reproduced by the experiment. Wall shear stress and heat transfer show declining behavior up to $x = 80 \%$ corresponding to an increasing laminar boundary layer thickness in flow direction. An instationary analysis of the simulation indicates the existence of a periodically occurring laminar separation bubble at about $x = 80 \%$ disturbed by the incoming vane wakes. Further downstream, a steep increase in measurement and simulation profiles marks the averaged transition region and a turbulent boundary layer develops.

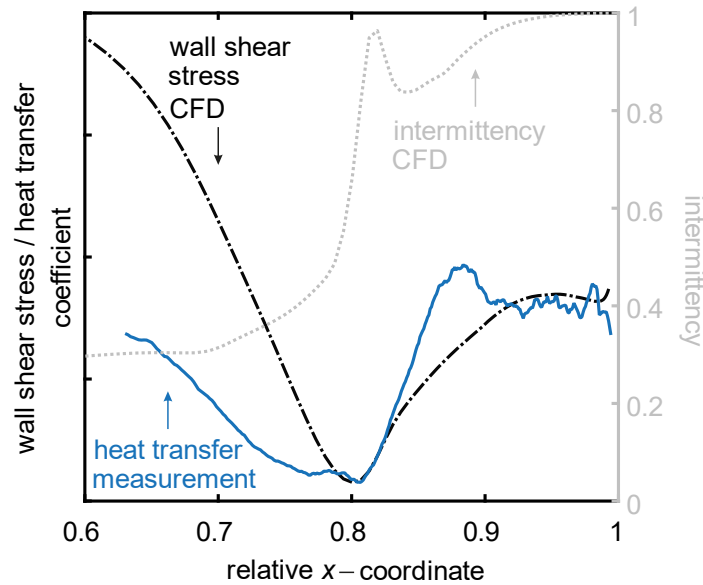


Figure 44 Radially averaged profile plots within 30 – 45 % of the blade height (see Fig. 43). The y-axis corresponds to wall shear stress and intermittency of the CFD simulation and heat transfer of the TDT measurement, respectively. For better comparison of the transition position the TDT data were scaled in y-direction to match the CFD wall shear stress. The image was modified from [A1].

It is emphasized that the comparison of heat transfer coefficient and wall shear stress serves only to verify the measured position of transition and the other flow effects. A quantitative comparison of the development of both parameters across the blade is affected by uncertainties of the CFD model and other non-linear effects. One non-linear effect results from a variable Reynolds analogy factor due to the high degree of turbulence intensity, the surface roughness and the adverse pressure gradient, which was already discussed in Sec. 2.3.3. Another effect emerges from the unheated starting length between leading edge of the blade and the start of the heating area as described in Sec. 2.2.3 and 4.5.

A simple correction as proposed in Sec. 4.5 cannot be applied in this case due to the non-zero pressure gradient for which the used theory is not necessarily valid. A coupled fluid and heat transfer simulation might lead to the required non-uniform heating correction. This approach must, however, be evaluated in future experiments.

In summary, the good agreement between the present measurement and simulated wall shear stress regarding the position of boundary layer phenomena indicates that the total of the described effects has little influence on the streamwise position of the laminar-turbulent transition. The comparison to the simulated intermittency confirms this result and shows that the TDT method can be successfully applied in rotating aerodynamic systems to visualize near wall boundary layer effects. It therefore offers high potential for the conceptual improvement of CFD models to correctly estimate friction losses in turbines.

6.5 Uncertainty estimation

The localization of flow effects with TDT is accompanied by measurement uncertainties as described in detail in Sec. 3.4.6. In the vane and blade experiments of this chapter, the accuracy of the reference grid positioning and the reprojection error lead to a spatial systematic error in the analysis region of about 1 mm on the blade surface. In the rotating blade measurement, the jitter of the trigger control of 500 ns and the motion blur of the blade at about 100 m/s rotational speed and 10 μ s exposure time of the sensor cause an additional spatial error of 1 mm in the analysis region. Due to the small aperture of the borescope optics, the depth of field was sufficiently large to provide negligible blurring of the image within the analysis region of 30 – 45 % of the blade height as can be seen from the left-hand side of Fig. 18. Due to the large viewing angle, the spatial error increases towards the tip of the blade due to the limited depth of field and the faster movement of the blade. The viewing angle increases towards the endwall which results in an increasing reprojection error (see right-hand side of Fig. 18).

In the vane measurement, the projection of the total spatial error onto the relative x – coordinate yields a relative error of about 1 % of the axial chord length, while in the blade measurement a total relative error of 2 % of the axial chord length was estimated within the analysis region. The motion blur represents the main part of the error which can in principle be partly corrected in the image post-processing by deconvolution with the known point spread function [10, 114]. However, this has not been examined in the present work and is the subject of future efforts.

The blurring effects caused by trigger jitter, blade movement and optical depth of field can be described by a convolution of the signal with the point spread function as convolution kernel. This reduces the contrast in the image and induces a systematic error on the pixel intensity (see Eq. (53)). The effect is particularly pronounced in regions with strong heat transfer gradients which leads to a reduced signal of the detected flow effect. A systematic bias or a smoothed signal has a minor influence on the detected position of a boundary layer transition. However, the smoothed signal must be greater than the statistical noise in the image which is caused by sensor noise and photonic shot noise. For a single measurement, the SNR is smaller than one so that a transition detection is not possible. Hence, the noise was reduced by averaging 3000 measurements and 80 pixel rows for each measurement resulting in an effective number of averaged measurements of $M = 240,000$. With Eq. (62) the relative random error of the TDT signal within the analysis region is calculated to $\sigma_{\Lambda,rel} = 11.5$ % within a confidence interval of 95 %. This corresponds to a $SNR \approx 7$ at which flow effects can be detected.

6.6 Conclusion on the application of TDT in turbine environments

In the experiments of this chapter, TDT was used for flow visualization and laminar–turbulent transition detection in a rotating turbine rig for the first time. Several conclusions can be drawn from these experiments:

1. It was shown that the TDT setup consisting of a high–speed infrared camera with borescope, a pulsed high–energy laser with beam guiding optics and a surface coating system can be used to detect laminar–turbulent transition, flow separation and secondary vortex flows on stationary vanes and rotating blades in realistic turbine environments.
2. Compared to other measurement techniques like surface hot films, the design of the components offers flexible and fast integration in multiple rig environments with reduced optical accessibility. No complex instrumentation of the blade and additional telemetry systems are necessary. TDT provides a temporally averaged, two–dimensional heat transfer map of the blade surface with a high spatial resolution.
3. The surface roughness of the coating can have an influence on the measured boundary layer. To find a surface coating with optimal trade–off between roughness and emissivity, Eq. (32) can be applied to estimate the critical roughness at which an influence on transition is expected.
4. In the rotating blade measurement, laminar–turbulent transition, and the influence of vortex systems on the near wall flow were visualized for the first time. A comparison to CFD simulations confirmed the observed results. Despite the higher noise level, detailed analysis of heat transfer effects is enabled for future experiments in rotating systems.

TDT provides valuable, previously unattained data to prove the performance of guide vanes and rotor blades and can be used to develop deeper understanding, for example, regarding transition processes, shock–wave boundary layer interaction and heat transfer processes on rig components. Additionally, CFD models can be supported and validated for a variety of design tasks like transition positioning, end–wall contouring and blade film–cooling. It thus promotes the development of highly efficient gas turbines to reduce CO₂ emissions and fuel consumption for modern aircraft engines.

Chapter 7

Conclusion and outlook

TDT was introduced as a measurement method to visualize near-wall heat transfer phenomena in applications ranging from simple flat plates and airfoils to experimentally challenging fast rotating turbine blades. It was successfully applied to stationary components exposed to a steady air flow and enabled the spatial visualization of laminar-turbulent transition on fast rotating turbine blades for the first time ever.

TDT uses a combination of pulsed radiative heating and infrared imaging to analyze the transient response of the surface temperature shortly after an energy pulse. Dependent on the convective flow condition, the rate of the transient temperature decline varies over the surface area and convective flow effects can be visualized by plotting the decline rate for every pixel. Numerical simulations and the analysis of an analytical model of the heat transfer processes showed that the rate of the local temperature decline is proportional to the heat transfer coefficient. Thus, spatial information of the near-wall heat transfer is provided across the aerodynamic component.

In this thesis, the measurement setup and procedure, the post-processing methods and the measurement instruments were described in detail. Laser and flash lamp, coating systems, infrared cameras, newly developed optics, and a trigger control were characterized by experiments. In a first experiment, the TDT setup was applied to a stationary flat plate in a free-jet facility. Here, the theoretically motivated linear relation of temperature decline rate and heat transfer coefficient was confirmed and a calibration for quantitative heat transfer measurements was conducted for heat transfer coefficients between 50 and 500 W/(m²K). An example was given, that the found calibration relation holds valid when applied to other flow conditions. For the calibration, the flat plate Nusselt correlation was used which lead to a high systematic uncertainty. This calibration error can be improved by using a second measurement method with low uncertainty in future experiments. Additional systematic errors were observed in experiments with spatially variable illumination or on large components where several measurement areas must be stitched together. Here, differences in velocity and thermal boundary layer lead to inconsistent heat transfer measurements. To correct for these errors, a non-uniform heating correction was successfully established for flows with negligible pressure gradients. The experiments

showed that the TDT method enables quantitative heat transfer measurements with high spatial resolution and a non-invasive measurement setup.

As a next step, TDT was applied to a NACA 0018 airfoil for validation with the well-established surface hot film method. Excellent agreement between both methods was observed with respect to the qualitative heat transfer behavior across the airfoil and the quantitative position of boundary layer transition. It was shown that the described post-processing method effectively reduces interfering effects like reflections, inhomogeneous illumination, and conduction losses, and enhances the data quality in the resulting TDT image. In addition to steady transition detection, an order of magnitude estimation showed that unsteady transition detection at a measurement rate of about 80 Hz can be conducted in systems that allow for the use of camera integration times $> 200 \mu\text{s}$ and camera lenses with large apertures $> f/2.0$. This estimation was based on the convective conditions found on the NACA 0018 airfoil and is principally limited by the duration of the temperature transient, the repetition rate of the energy source and the noise level of the TDT image. Future experiments are necessary to verify and further specify the estimated limits.

In the last set of experiments, TDT was applied to stationary vanes and rotating blades of a gas turbine rig. Due to the limited optical access, new optics for camera observation and laser pulse forming were developed. The precise synchronization of camera, laser and rotating blade was enabled by a custom-made trigger control. The experiments provided a proof of concept which showed that despite the low aperture of the borescope and the short camera integration time of $10 \mu\text{s}$, the heat transfer traces of several flow phenomena like boundary layer transition and turbulent vortices can be successfully visualized. The presented TDT technique can be potentially expanded in the future for accurate quantitative determination of the surface heat transfer; however, some efforts are still necessary in this direction. This includes a quantitative correction for unheated starting lengths in pressure gradient flows and improvements of the calibration measurement to reduce uncertainties.

In summary, the TDT method is capable of qualitative heat transfer visualization and quantitative laminar-turbulent transition detection for a broad range of applications and geometries. Combined with the possibility to measure quantitative heat transfer after calibration, the method is advantageous for a range of high-speed applications like in gas turbines and blow-down wind tunnels, where a two-dimensional overview of the flow situation, but also detailed quantitative and time-resolved information are required. The non-uniform heating correction further expands the range of applications and enables the use of TDT on large aerodynamic components like wind turbine blades or aerodynamic vehicles. The hope is that TDT will enable future experiments to support the development of highly efficient aerodynamic systems and to combine technical innovation with a sustainable future.

References

- [1] ICAO, "2016 Environmental Report," 2016. [Online]. Available: <https://www.icao.int/environmental-protection/Documents>. [Accessed 6 December 2019].
- [2] E. Terrenoire, D. Hauglustaine, T. Gasser and O. Penanhoat, "The contribution of carbon dioxide emissions from the aviation sector to future climate change," *Environmental Research Letters*, vol. 14, no. 8, p. 084019, 2019.
- [3] O. Reynolds, "XXIX. An experimental investigation of the circumstances which determine whether the motion of water shall be direct or sinuous, and of the law of resistance in parallel channels.," *Philosophical Transactions of the Royal society of London*, vol. 174, pp. 935-982, 1883.
- [4] L. Prandtl, "Entstehung von Wirbeln bei Wasserströmungen–1. Entstehung von Wirbeln und künstliche Beeinflussung der Wirbelbildung," Institut für Wissenschaftlichen Film, Göttingen, 1936.
- [5] H. L. Dryden, "Recent advances in the mechanics of boundary layer flow," *In Advances in Applied Mechanics*, vol. 1, pp. 1-40, 1948.
- [6] C. J. Kähler, S. Scharnowski and C. Cierpka, "On the resolution limit of digital particle image velocimetry," *Experiments in Fluids*, vol. 52, no. 6, p. 1629–1639, 2012.
- [7] J. Woisetschläger, R. Pecnik, E. Göttlich, O. Schennach, A. Marn, W. Sanz and F. Heitmeir, "Experimental and numerical flow visualization in a transonic turbine," *Journal of visualization*, vol. 11, no. 1, pp. 95-102, 2008.
- [8] M. Stadlbauer, J. Gründmayer and F. von Plehwe, "Method for determining a transition point and/or for determining wall shear stresses on surfaces around which surfaces a flow circulates, and measuring device". Patent WO2014198251 A1, 2014.
- [9] W. Demtröder, *Experimentalphysik 2: Elektrizität und Optik*, Berlin: Springer-Verlag, 2018.
- [10] M. Vollmer and K. P. Möllmann, *Infrared thermal imaging: fundamentals, research and applications*, Weinheim: John Wiley & Sons, 2017.
- [11] J. Lohrengel and R. Todtenhaupt, "Wärmeleitfähigkeit, Gesamtemissionsgrade und spektrale Emissionsgrade der Beschichtung Nextel-Velvet-Coating 811-21 (RAL 900 15 tiefschwarz matt)," *PTB-Mitteilungen*, vol. 106, pp. 259-265, 1996.

- [12] X. He, Y. Li, L. Wang, Y. Sun and S. Zhang, "High emissivity coatings for high temperature application: progress and prospect," *Thin Solid Films*, vol. 517, no. 17, pp. 5120-5129, 2009.
- [13] F. Incropera and D. De Witt, *Fundamentals of Heat and Mass Transfer*, New York: Wiley, 1985.
- [14] H. Schlichting, *Boundary Layer Theory*, New York: Mc-Graw-Hill, 1968.
- [15] T. Astarita and G. M. Carlomagno, *Infrared Thermography for Thermo-Fluid-Dynamics*, Berlin, Heidelberg: Springer, 2013.
- [16] W. S. Saric, "Physical description of boundary-layer transition: Experimental evidence," *AGARD, Special Course on Progress in Transition Modelling*, vol. 793, p. 51, 1994.
- [17] R. Mayle, "The 1991 IGTI Scholar Lecture: The Role of Laminar-Turbulent Transition in Gas Turbine Engines," *Journal of Turbomachinery*, vol. 113, no. 4, pp. 509-536, 1991.
- [18] H. Schlichting and K. Gersten, *Grenzschicht-Theorie*, Berlin, Heidelberg: Springer-Verlag, 2006.
- [19] S. Hunklinger, *Festkörperphysik*, München: Oldenbourg Verlag, 2009.
- [20] O. Reynolds, "On the Extent and Action of the Heating Surface for Steam Boilers," *Manchester Literature Philosophical Society*, vol. 14, p. 7–12, 1874.
- [21] J. Bons, "A Critical Assessment of Reynolds Analogy for Turbine Flows," *Journal of Heat Transfer*, no. 127, pp. 472-485, 2005.
- [22] T. H. Chilton and A. P. Colburn, "Mass transfer (absorption) coefficients prediction from data on heat transfer and fluid friction," *Industrial and Engineering Chemistry*, vol. 26, no. 11, pp. 1183-1187, 1934.
- [23] A. Colburn, "A method of correlating forced convection heat-transfer data and a comparison with fluid friction," *International Journal of Heat and Mass Transfer*, vol. 7, no. 12, pp. 1359-1384, 1933.
- [24] H. Blasius, "Grenzschichten in Flüssigkeiten mit Kleiner Reibung," *Zeitschrift für Angewandte Mathematik und Physik*, vol. 56, pp. 1 - 37, 1908.
- [25] E. Pohlhausen, "Der Wärmeaustausch zwischen festen Körpern und Flüssigkeiten mit kleiner Reibung und kleiner Wärmeleitung," *Journal of Applied Mathematics and Mechanics*, vol. 1, no. 2, pp. 115-121, 1921.

- [26] W. C. Reynolds, W. M. Kays and S. J. Kline, "Heat Transfer in the Turbulent Incompressible Boundary Layer: II - Step Wall Temperature Distribution," NASA Memo 12-2-58W, Washington, 1958.
- [27] M. Tribus and J. Klein, "Forced convection from non-isothermal surfaces," in *Proceedings of the Heat Transfer Symposium*, Ann Arbor, 1952.
- [28] J. R. Sellars, M. Tribus and S. J. Klein, "Heat Transfer to Laminar Flow in a Round Tube or Flat Conduit - the Graetz Problem Extended," *Transactions of the ASME*, vol. 78, no. 2, pp. 441-448, 1956.
- [29] M. W. Rubesin, "The Effect of an Arbitrary Surface Temperature Variation on the Convective Heat Transfer in an Incompressible Turbulent Boundary Layer," NACA TN 2345, Washington DC, 1951.
- [30] W. M. Kays and M. E. Crawford, *Convective heat and mass transfer*, New York: McGraw-Hill, 1993.
- [31] J. M. Hacker and J. K. Eaton, "Measurements of heat transfer in a separated and reattaching flow with spatially varying thermal boundary conditions," *International Journal of Heat and Fluid Flow*, vol. 18, no. 1, pp. 131-141, 1997.
- [32] G. J. Walker, "The role of laminar-turbulent transition in gas turbine engines: A discussion," *Journal of Turbomachinery*, vol. 115, no. 2, pp. 207-216, 1993.
- [33] E. Dick and S. Kubacki, "Transition models for turbomachinery boundary layer flows: a review," *International Journal of Turbomachinery, Propulsion and Power*, vol. 2, no. 2, p. 4, 2017.
- [34] M. F. Blair, "Boundary-layer transition in accelerating flows with intense freestream turbulence: Part 1-Disturbances upstream of transition onset," *Journal of Fluids Engineering*, vol. 114, no. 3, pp. 313-321, 1992.
- [35] M. F. Blair, "Boundary-layer transition in accelerating flows with intense freestream turbulence: Part 2 - The zone of intermittent turbulence," *Journal of Fluids Engineering*, vol. 114, no. 3, pp. 322-332, 1992.
- [36] J. P. Gostelow, A. R. Blunden and G. J. Walker, "Effects of free-stream turbulence and adverse pressure gradients on boundary layer transition," *Journal of Turbomachinery*, vol. 116, no. 3, pp. 392-404, 1994.

- [37] B. J. Abu-Ghannam and R. Shaw, "Natural transition of boundary layers - the effects of turbulence, pressure gradient, and flow history," *Journal of Mechanical Engineering Science*, vol. 22, no. 5, pp. 213-228, 1980.
- [38] P. Dassler, D. Kožulović and A. Fiala, "Modelling of roughness-induced transition using local variables," in *V European Conference on CFD*, Lisbon, 2010.
- [39] E. G. Feindt, Untersuchungen über die Abhängigkeit des Umschlages laminar-turbulent von der Oberflächenrauigkeit und der Druckverteilung, Dissertation: Technische Hochschule Carolo-Wilhelmina zu Braunschweig, 1957.
- [40] R. G. Jacobs and P. A. Durbin, "Simulations of bypass transition," *Journal of Fluid Mechanics*, vol. 428, pp. 185-212, 2001.
- [41] L. Brandt and H. C. De Lange, "Streak interactions and breakdown in boundary layer flows," *Physics of Fluids*, vol. 20, no. 2, p. 024107, 2008.
- [42] Z. Xu, Q. Zhao, Q. Lin and J. Xu, "Large eddy simulation on the effect of free-stream turbulence on bypass transition," *International Journal of Heat and Fluid Flow*, vol. 54, pp. 131-142, 2015.
- [43] R. J. Volino and L. S. Hultgren, "Measurements in separated and transitional boundary layers under low-pressure turbine airfoil conditions," *Journal of Turbomachinery*, vol. 123, no. 2, pp. 189-197, 2001.
- [44] B. R. McAuliffe and M. I. Yaras, "Transition mechanisms in separation bubbles under low-and elevated-freestream turbulence," *Journal of Turbomachinery*, vol. 132, no. 1, p. 011004, 2010.
- [45] A. P. Wheeler, R. D. Sandberg, N. D. Sandham, R. Pichler, V. Michelassi and G. Laskowski, "Direct numerical simulations of a high-pressure turbine vane," *Journal of Turbomachinery*, vol. 138, no. 7, p. 071003, 2016.
- [46] R. Mittal, U. Madanan and R. Goldstein, "The heat/mass transfer analogy for a backward facing step," *International Journal of Heat and Mass Transfer*, vol. 113, pp. 411-422, 2017.
- [47] D. E. Halstead, D. C. Wisler, T. H. Okiishi, G. J. Walker, H. P. Hodson and H. W. Shin, "Boundary layer development in axial compressors and turbines: Part 1: Composite picture," *Journal of Turbomachinery*, vol. 119, no. 1, p. 114-127, 1997.
- [48] O. P. Sharma and T. L. Butler, "Predictions of endwall losses and secondary flows in axial flow turbine cascades," *Journal of Turbomachinery*, vol. 109, no. 2, pp. 229-236, 1987.
- [49] C. H. Sieverding, "Recent progress in the understanding of basic aspects of secondary flows in turbine blade passages," *Journal of Turbomachinery*, vol. 107, no. 2, pp. 248-257, 1985.

- [50] L. S. Langston, "Secondary flows in axial turbines - a review," *Annals of the New York Academy of Sciences*, vol. 934, no. 1, pp. 11-26, 2001.
- [51] H. P. Wang, S. J. Olson, R. J. Goldstein and E. R. Eckert, "Flow visualization in a linear turbine cascade of high performance turbine blades," *Journal of Turbomachinery*, vol. 119, no. 1, pp. 1-8, 1997.
- [52] R. J. Goldstein, H. P. Wang and M. Y. Jabbari, "The influence of secondary flows near the endwall and boundary layer disturbance on convective transport from a turbine blade," *Journal of Turbomachinery*, vol. 117, no. 4, pp. 657-665, 1995.
- [53] P. J. Newton, G. D. Lock, S. K. Krishnababu, H. P. Hodson, W. N. Dawes, J. Hannis and C. Whitney, "Heat transfer and aerodynamics of turbine blade tips in a linear cascade," *Journal of Turbomachinery*, vol. 128, no. 2, pp. 300-309, 2006.
- [54] N. Abuaf, R. S. Bunker and C. P. Lee, "Effects of surface roughness on heat transfer and aerodynamic performance of turbine airfoils," *Journal of Turbomachinery*, vol. 120, no. 3, pp. 522-529, 1998.
- [55] B. J. Belnap, J. A. Van Rij and P. M. Ligrani, "A Reynolds analogy for real component surface roughness," *International Journal of Heat and Mass Transfer*, vol. 45, no. 15, pp. 3089-3099, 2002.
- [56] S. Han and R. Goldstein, "The heat/mass transfer analogy for a simulated turbine blade," *International Journal of Heat and Mass Transfer*, vol. 51, no. 21-22, pp. 5209-5225, 2008.
- [57] F. Hamdi, J. Seo and S. Han, "Numerical study of heat and mass transfer analogy for a simulated turbine endwall," *Journal of Mechanical Science and Technology*, vol. 31, no. 9, pp. 4275-4283, 2017.
- [58] G. Zissis and W. Wolfe, *The Infrared Handbook*, Michigan: ERIM Press, 1993.
- [59] A. Milton, F. Barone and M. Kruer, "Influence of nonuniformity on infrared focal plane array performance," *Optical Engineering*, vol. 24, no. 5, pp. 885-862, 1985.
- [60] A. Redjimi, D. Knežević, K. Savić, N. Jovanović, M. Simović and D. Vasiljević, "Noise Equivalent Temperature Difference Model for Thermal Imagers, Calculation and Analysis," *Scientific Technical Review*, vol. 64, no. 2, pp. 42-49, 2014.
- [61] D. P. DeWitt and G. D. Nutter, *Theory and practice of radiation thermometry*, New York: John Wiley & Sons, 1988.
- [62] W. Nitsche and A. Brunn, *Strömungsmesstechnik*, Berlin Heidelberg: Springer-Verlag, 2006.

- [63] R. L. Maltby, Flow visualization in wind tunnels using indicators, Paris: Advisory Group for Aeronautical Research and Development, 1962.
- [64] E. Schülein, "Development and Application of the Thin Oil Film Technique for Skin Friction Measurements in the Short-Duration Hypersonic Wind Tunnel," in *New Results in Numerical and Experimental Fluid Mechanics IV*, München, Springer Science & Business Media, 2004, pp. 407-414.
- [65] R. Radespiel, D. G. Francois, D. Hoppmann, S. Klein, P. Scholz, K. Wawrzinek, T. Lutz and T. Knopp, "Simulation of wing stall," in *43rd AIAA Fluid Dynamics Conference*, San Diego, 2013.
- [66] F. Haselbach and W. Nitsche, "Calibration of single-surface hot films and in-line hot-film arrays in laminar or turbulent flows," *Measurement Science and Technology*, vol. 7, no. 10, pp. 1428-1438, 1996.
- [67] A. R. P. van Heiningen, A. S. Mujumdar and W. J. M. Douglas, "On the use of hot and cold-film sensors for skin friction and heat transfer measurements in impingement flows," *Letters in Heat and Mass Transfer*, vol. 3, no. 6, pp. 523-528, 1976.
- [68] H. P. Hodson, I. Huntsman and A. B. Steele, "An investigation of boundary layer development in a multistage LP turbine," *Journal of Turbomachinery*, vol. 116, no. 3, pp. 375-383, 1994.
- [69] O. Burkhardt, Erprobung und Anwendung von Oberflächensensoren und Sensorarrays zur Erfassung instationärer Wandschubspannungen an Schaufelprofilen, Dissertation: Technische Universität Berlin, 2004.
- [70] H. Lang, T. Mørck and J. Woisetschläger, "Stereoscopic particle image velocimetry in a transonic turbine stage," *Experiments in Fluids*, vol. 32, no. 6, p. 700–709, 2002.
- [71] M. Wernet, D. Van Zante, T. Strazisar, W. John and P. Prahst, "3-D Digital PIV Measurements of the Tip Clearance Flow in an Axial Compressor," in *ASME Turbo Expo 2002: Power for Land, Sea, and Air*, Amsterdam, 2002.
- [72] K. Day, P. Lawless and S. Fleeter, "Particle image velocimetry measurements in a low speed two stage research turbine," in *32nd Joint Propulsion Conference and Exhibit*, Lake Buena Vista, 1996.
- [73] M. Bross, T. Fuchs and C. J. Kähler, "Interaction of coherent flow structures in adverse pressure gradient turbulent boundary layers," *Journal of Fluid Mechanics*, vol. 873, pp. 287-321, 2019.
- [74] C. Camci and B. Glezer, "Liquid crystal thermography on the fluid solid interface of rotating systems," *Journal of Heat Transfer*, vol. 119, no. 1, pp. 20-29, 1997.

- [75] B. K. Crawford, G. T. Duncan Jr, D. E. West and W. S. Saric, "Laminar-Turbulent Boundary Layer Transition Imaging Using IR Thermography," *Optics and Photonics Journal*, vol. 3, no. 3, p. 233, 2013.
- [76] R. Ricci and S. Montelpare, "A quantitative IR thermographic method to study the laminar separation bubble phenomenon," *International Journal of Thermal Science*, vol. 8, no. 44, pp. 709-719, 2005.
- [77] D. Yorita, K. Asai, C. Klein, U. Henne and S. Schaber, "Transition detection on rotating propeller blades by means of temperature sensitive paint," in *In 50th AIAA Aerospace Sciences Meeting including the New Horizons Forum and Aerospace Exposition*, Nashville, 2012.
- [78] M. Mori, L. Novak and M. Sekavčnik, "Application of IR thermography as a measuring method to study heat transfer on rotating surface," *Forsch Ingenieurwes*, vol. 72, no. 1, pp. 1-10, 2008.
- [79] T. Reichstein, A. Schaffarczyk, C. Dollinger, N. Balaesque, E. Schülein, C. Jauch and A. Fischer, "Investigation of Laminar–Turbulent Transition on a Rotating Wind-Turbine Blade of Multimegawatt Class with Thermography and Microphone Array," *Energies*, vol. 12, no. 11, p. 2102, 2019.
- [80] K. Richter and E. Schülein, "Boundary Layer Transition Measurements on Hovering Helicopter Rotors by Infrared Thermography," *Experiments in Fluids*, vol. 55, no. 7, pp. 1-13, 2014.
- [81] R. Thiessen and E. Schülein, "Infrared Thermography and DIT of Quadcopter Rotor Blades Using Laser Heating," in *15th International Workshop on Advanced Infrared Technology and Applications*, Florence, 2019.
- [82] M. Raffel and C. B. Merz, "Differential infrared thermography for unsteady boundary-layer transition measurements," *AIAA Journal*, vol. 52, no. 9, pp. 2090-2093, 2014.
- [83] M. Raffel, C. B. Merz, T. Schwermer and K. Richter, "Differential infrared thermography for boundary layer transition detection on pitching rotor blade model," *Experiments in Fluids*, vol. 56, no. 2, p. 30, 2015.
- [84] E. Gartenberg and R. E. Wright, "Boundary-layer transition detection with infrared imaging emphasizing cryogenic applications," *AIAA journal*, vol. 32, no. 9, pp. 1875-1882, 1994.
- [85] W. Cook and E. Felderman, "Reduction of data from thin-film heat-transfer gages - A concise numerical technique," *AIAA Journal*, vol. 4, no. 3, pp. 561-562, 1966.
- [86] D. N. Kendall and W. Dixon, "Heat Transfer Measurements in a Hot Shot Wind Tunnel," *Transactions on Aerospace and Electronic Systems*, vol. 3, no. 4, pp. 596-603, 1996.

- [87] D. G. Walker and E. P. Scott, "Evaluation of estimation methods for high unsteady heat fluxes from surface measurements.," *Journal of Thermophysics and Heat Transfer*, vol. 12, no. 4, pp. 543-551, 1998.
- [88] E. Schülein, "Skin-Friction and Heat Flux Measurements in Shock/Boundary-Layer Interaction Flows," *AIAA Journal*, vol. 44, no. 8, pp. 1732-1741, 2006.
- [89] M. K. Yadav, S. K. Singh, A. Parwez and S. Khandekar, "Inverse models for transient wall heat flux estimation based on single and multi-point temperature measurements," *International Journal of Thermal Sciences*, vol. 124, pp. 307-317, 2018.
- [90] D. Modenini and F. F. J. Schrijer, "Heat transfer measurements in a supersonic wind tunnel through inverse temperature data reduction: application to a backward facing step," *Quantitative Infrared Thermography*, vol. 9, no. 2, pp. 209-230, 2012.
- [91] F. Avallone, "A low-computational-cost inverse heat transfer technique for convective heat transfer measurements in hypersonic flows," *Experiments in Fluids*, vol. 56, no. 4, pp. 56-86, 2015.
- [92] F. C. von Plehwe, Numerische und experimentelle Untersuchung von Wärmetransportphänomenen nach Impulsanregung als Verfahren zur Strömungssichtbarmachung, Diplomarbeit: RWTH Aachen, 2013.
- [93] G. Lück, "Binder-Schmidt-Verfahren für nichtstationäre Wärmequellenprobleme," *Chemie Ingenieur Technik*, vol. 33, no. 8, pp. 547-550, 1961.
- [94] W. Minkina and S. Dudzik, *Infrared Thermography Errors and Uncertainties*, Chichester: John Wiley & Sons, 2009.
- [95] G. Erlacher, Feasibility Study of Temperature Measurements in Turbine Center Frames by Infrared Thermography, Master Thesis: Graz, 2019.
- [96] R. Khare and P. K. Shukla, "Temporal stretching of laser pulses," in *Coherence and Ultrashort Pulse Laser Emission*, London, IntechOpen, 2010, p. 205.
- [97] A. Fiala and E. Kügeler, "Roughness modeling for turbomachinery," in *Turbo Expo: Power for Land, Sea, and Air*, Vancouver, 2011.
- [98] Speciality Coating Systems, "www.scscoatings.com," [Online]. Available: <https://scscoatings.com/wp-content/uploads/2017/09/02-SCS-Parylene-Properties-1016.pdf>. [Accessed 13 March 2020].

- [99] Dupont, "www.dupont.com," [Online]. Available: <http://www.dupont.com/content/dam/dupont/products-and-services/membranes-and-films/polyimide-films/documents/DEC-Kapton-summary-of-properties.pdf>. [Accessed 23 May 2018].
- [100] R. E. Hanson, H. P. Buckley and P. Lavoie, "Aerodynamic optimization of the flat-plate leading edge for experimental studies of laminar and transitional boundary layers," *Experiments in Fluids*, vol. 53, no. 4, pp. 863-871, 2012.
- [101] M. Estorf, "Image based heating rate calculation from thermographic data considering lateral heat conduction," *International Journal of Heat and Mass Transfer*, vol. 49, no. 15-16, p. 2545–2556, 2006.
- [102] F. F. J. Schrijer, "Unsteady data reduction techniques for QIRT: consideration of temporal and spatial resolution," in *11th QIRT Conference*, Naples, 2012.
- [103] M. Ol, B. McCauliffe, E. Hanff, U. Scholz and C. J. Kähler, "Comparison of laminar separation bubble measurements on a low Reynolds number airfoil in three facilities," in *35th AIAA Fluid Dynamics Conference and Exhibit*, Toronto, 2005.
- [104] R. Hain, C. J. Kähler and R. Radespiel, "Dynamics of laminar separation bubbles at low-Reynolds-number aerofoils," *Journal of Fluid Mechanics*, vol. 630, pp. 129-153, 2009.
- [105] P. F. Lorber and F. O. Carta, "Unsteady transition measurements on a pitching three-dimensional wing," in *The Fifth Symposium on Numerical and Physical Aspects of Aerodynamic Flows*, East Hartford, 1992.
- [106] B. Simon, A. Filius, C. Tropea and S. Grundmann, "IR thermography for dynamic detection of laminar-turbulent transition," *Experiments in Fluids*, vol. 57, no. 5, p. 93, 2016.
- [107] M. Restemeier, J. Niewoehner, P. Jeschke, Y. Guendogdu and K. Engel, "Experimental and Numerical Investigation of Blade Row Spacing Effects in a 1.5 Stage Turbine Rig under Off-Design Operating Conditions," in *ISABE*, Gothenburg, 2011.
- [108] J. Niewöhner, Wirkungsgradpotential von nicht-rotationssymmetrischen Seitenwandkonturen und Schaufelneigung in einer subsonischen Axialturbine, Dissertation: Aachen, 2017.
- [109] S. Behre, R. Kluxen, P. Jeschke and Y. Guendogdu, "Development of Turbulence Intensity and Integral Length-Scale in a 1.5 Stage Axial Flow Turbine," in *International Gas Technology Conference*, Tokyo, 2015.

- [110] J. Niewoehner, T. Poehler, P. Jeschke and Y. Guendogdu, "Investigation of Nonaxisymmetric Endwall Contouring and Three-Dimensional Airfoil Design in a 1.5 Stage Axial Turbine—Part II: Experimental Validation," *Journal of Turbomachinery*, vol. 137, no. 8, p. 081010, 2015.
- [111] P. M. Nadge and R. N. Govardhan, "High Reynolds number flow over a backward-facing step: structure of the mean separation bubble," *Experiments in Fluids*, vol. 55, no. 1, p. 1657, 2014.
- [112] K. O'Malley, A. D. Fitt, T. V. Jones, J. R. Ockendon and P. Wilmott, "Models for high-Reynolds-number flow down a step," *Journal of Fluid Mechanics*, vol. 222, pp. 139-155, 1991.
- [113] J. Vogel and J. Eaton, "Combined Heat Transfer and Fluid Dynamic Measurements Downstream of a Backward-Facing Step," *Journal of Heat Transfer*, vol. 107, no. 4, pp. 922-929, 1985.
- [114] R. C. Gonzalez and R. E. Woods, Digital image processing, Upper Saddle River, N.J.: Prentice Hall, 2008.

List of publications by the author

- [A1] S. von Hoesslin, J. Gruendmayer, A. Zeisberger, M. S. Sommer, J. Klimesch, S. Behre, H. Brandies and C. Kähler, "Visualization of laminar–turbulent transition on rotating turbine blades," *Experiments in Fluids*, 2020.
- [A2] S. von Hoesslin, J. Gruendmayer, A. Zeisberger and C. Kähler, "Non–uniform heating correction for Temperature Decline Thermography," in *HEFAT*, Wicklow, 2019.
- [A3] S. von Hoesslin, M. Stadlbauer, J. Gruendmayer and C. J. Kähler, "Temperature decline thermography for laminar–turbulent transition detection in aerodynamics," *Experiments in Fluids*, vol. 58, no. 9, p. 129, 2017.
- [A4] S. von Hoesslin, J. Gruendmayer, A. Zeisberger and C. J. Kähler, "Accessing quantitative heat transfer with Temperature Decline Thermography," *Experimental Thermal and Fluid Science*, vol. 108, pp. 55–60, 2019.

Acknowledgement

Finally, I would like to express my gratitude to all the people that supported me writing this thesis. In particular I would like to thank:

Prof. Dr. Christian J. Kähler for supervising this thesis, the support in technical questions and for several valuable discussions beyond fluid mechanics.

Hans-Rüdiger Deubert, Dr. Frank Grauer, Dr. Carsten Subel and Tim Haas for giving me the opportunity to write my thesis in the Testing and Measurement Technology team at MTU Aero Engines.

The whole Testing and Measurement Technology team for their technical and administrative advices and relaxing lunch breaks.

A special thanks goes to my supervisors Jürgen Gründmayer, Martin Stadlbauer and Andreas Zeisberger for encouraging and forward-looking discussions and for problem solving in difficult situations. They invested a lot of time helping me with experiments, discussing questions and proofreading my thesis.

A special thanks goes also to my family for their support and dedication, for the joyful weekends and valuable discussions. To Jonathan Klimesch for the additional proofreading, for the enjoyable moments and especially for allowing me to see things in life from a different perspective.

Finally, I am proud sharing my life with my wonderful wife Madlaina von Hößlin. Her positive and intelligent way encourages me every day and gives me a happy life beyond work. Together with her (and our bikes) everything seems possible.